TU Delft

Delft University of Technology

Numerical Investigation of Turbidity Flows Generated by Polymetallic Nodules Mining

Elerian, M.F.A.I.

DOI
10.4233/uuid:9903501f-5614-4380-893e-f51a1eef3dca

Publication date
2023

Document Version
Final published version

Citation (APA)
Elerian, M. F. A. I. (2023). *Numerical Investigation of Turbidity Flows Generated by Polymetallic Nodules Mining*. [Dissertation (TU Delft), Delft University of Technology]. https://doi.org/10.4233/uuid:9903501f-5614-4380-893e-f51a1eef3dca

Important note
To cite this publication, please use the final published version (if applicable).
Please check the document version above.

Copyright
Other than for strictly personal use, it is not permitted to download, forward or distribute the text or part of it, without the consent of the author(s) and/or copyright holder(s), unless the work is under an open content license such as Creative Commons.

Takedown policy
Please contact us and provide details if you believe this document breaches copyrights.
We will remove access to the work immediately and investigate your claim.

This work is downloaded from Delft University of Technology.
For technical reasons the number of authors shown on this cover page is limited to a maximum of 10.

Numerical Investigation of Turbidity Flows Generated by Polymetallic Nodules Mining

Numerical Investigation of Turbidity Flows Generated by Polymetallic Nodules Mining

Proefschrift

ter verkrijging van de graad van doctor
aan de Technische Universtiteit Delft,
op gezag van de Rector Magnificus Prof.dr.ir. T.H.J.J van der Hagen,
voorzitter van het College voor Promoties,
in het openbaar te verdedigen
op Tuesday 5 September 2023 om 10:00 uur
door

Mohamed ELERIAN

Werktuigkundig ingenieur
geboren te Hail, Saudi Arabia.

Dit proefschrift is goedgekeurd door de promotor:

Prof.dr.ir. C. van Rhee

Copromotor:

Dr.ir. R.L.J Helmons

Samenstelling promotiecommissie:

Rector Magnificus,	voorzitter
Prof.dr.ir. C. van Rhee,	Technische Universiteit Delft
Dr.ir. R.L.J Helmons,	Technische Universiteit Delft

Onafhankelijke leden:

Dr. J. Spearman	HR Wallingford, UK
Prof.dr. L. Thomsen	University of Gothenburg, Sweden
Prof.dr. G.J. Reichart	NIOZ, the Netherlands
Prof.dr.ir. W.S.J. Uijttewaal	Technische Universiteit Delft
Prof.dr.ir. B.J. Boersma	Technische Universiteit Delft

©2023, M.F.A.I. Elerian

All rights reserved. No part of this book may be reproduced, stored in a retrieval system, or transmitted, in any form or by any means, without prior permission from the publisher.

ISBN 978-94-6366-720-3

Keywords: Deep Sea Mining, polymetallic nodules, near-field region, turbidity Current, flocculation modelling, multi-phase drift flux model, population balance model

Published and distributed by Ridderprint
PRINTED IN THE NETHERLANDS

Financial support
This study was conducted as a part of the Blue Harvesting project, supported by the European Union's EIT, EIT RawMaterials and has received funding under Framework Partnership Agreement No [FPA 2016/EIT/EIT Raw Materials], Specific Grant Agreement No [EIT/RAW MATERIALS/SGA2019/1], Project Agreement 18138.

To Ayat and Malek

Contents

Summary **xi**

Samenvatting **xv**

List of Tables **xix**

List of Figures **xxi**

1 Introduction **1**
1.1 Background 1
1.2 Scope 7
1.3 Objectives and Research Questions 8
1.4 Dissertation Outline 9

2 The State-of-The-Art-Knowledge **13**
2.1 Introduction 14
2.2 Discharge Process 17
2.3 Flow Specification 22
2.4 Flow Physics 31
2.5 Synthesis and Outlook 37

3 Dynamics of the Near-Field Generated Flows **39**
3.1 Lagrangian Plume Model 40
3.2 Four-Equation Model for Turbidity Currents 41
3.3 Model Application 44
3.4 Comparison of Results 46
3.5 Flocculation 47
3.6 Synthesis and Outlook 50

4 DSM-Generated Turbidity Currents **53**
4.1 Introduction 54
4.2 Experimental Apparatus and Laboratory Experiments 58
4.3 Experimental Results 63
4.4 Numerical Model Description 69
4.5 Comparison of Numerical Simulations with Experiments . . . 77
4.6 Conclusions 82

5 Flocculation Effect in DSM-Generated Turbid flows **85**
5.1 Introduction 86
5.2 Mathematical Model 89
5.3 Numerical Model 98
5.4 Case Studies 105
5.5 Conclusions 117

6 The Influence of System Design on the Dispersion and Flocculation of Turbidity Currents **121**
6.1 Numerical Model 124
6.2 Steady State in the PNMT Reference Frame 126
6.3 Comparison of the Results 127
6.4 Discussion 149
6.5 Conclusions and recommendations 152

7 Conclusions **155**
7.1 Conclusions 156

Bibliography **163**

List of Publications **177**
Journal Publications 177
Conference Publications 177

Curriculum Vitae **179**

Acknowledgements **181**

Summary

The depletion of terrestrial mineral deposits and the increasing demand for minerals are causing disruptions in the global supply chain. The shift towards renewable technologies requires significant quantities of metals used, for example, in the production of electric vehicles and wind turbines, putting additional strain on the supply chain. The deep seabed holds significant reserves of minerals that were discovered almost a century ago but remained untapped due to lack of technology and demand. However, with the current technological advances and demand, commercial extraction can be initiated in the coming years. Deep-sea mining poses several challenges due to the sensitive nature of the deep sea. The impact of mining operation on the surrounding region that can be affected from the generated turbidity flow can cause significant harm to the delicate marine ecosystem.

In this context, this study aims to provide a comprehensive understanding of the turbid flows resulting from the extraction of polymetallic nodules, a type of deep-sea deposit. To mine these nodules, special equipment such as a collector, a vertical transport system and a supporting vessel are needed. To date, the most mature technology used in this process is the hydraulic collector, which moves across the seabed and collects the nodules.After the nodules are collected by the hydraulic collector, a vertical transport system is used to transfer them to a supporting vessel. On the vessel, the nodules are carefully handled while the remaining effluents are discharged back into the water column. During the collection process, a mixture of water and sediment is inevitably collected along with the nodules. This mixture is discharged from the back of the collector into the environment. This process increases the turbidity level of the surrounding area and probably also beyond the mining region, so that there is a risk of losing the flora and fauna in the deep sea.

This study begins by investigating the state-of-the-art knowledge of the physical behavior of the encountered flows similar to plumes, jets, and turbidity

currents encountered near the collector, resulting in a classification of flow types, length and time scales in the near-field region, covering the fundamentals of the corresponding turbidity flows. Additionally, this literature review has highlighted the use of a 2D Lagrangian model, developed by Lee et al. in 2013, to predict the behavior of the water-sediment mixture in the jet/plume phase. The results from the 2D Lagrangian model are used as input for the four-equation model of Parker et al. in 1987. This coupling has enabled the examination of the impact of various discharge scenarios on the physical parameters of the current. Additionally, a specific scenario involving varying particle size is examined to investigate the effect of flocculation on the progression of the current. The results show that the characteristics of the generated turbidity current are highly dependent on the discharge conditions and particle size. This motivates further experimental studies on turbidity currents, including different initial conditions and detailed measurements for validation of numerical models.

A series of lock-exchange experiments are conducted in the dredging lab of Delft University of Technology. Different sediment types, with varying particle size distributions, are tested. High-speed camera and a specialized pixel-concentration calibration method are used to measure the local concentration at different length and time scales of the current propagation. The experimental results show that high initial concentrations of sediment with low particle size yield high front velocities. However, as the initial concentration increases to a certain threshold, particle size starts to lose its effect on the current. This implies that low concentration and larger particle sizes are more favorable at the impingement region. Additionally, the measured concentration distribution from these experiments is used to validate a newly implemented numerical mixture model as proposed by Goeree et al. in 2016. The front velocity and concentration profiles of the numerical model were found to be in good agreement with those in the experimental model.

The model was further extended by incorporating the population balance equation with the drift flux model to account for flocculation dynamics. The experimental work of Gillard et al. in 2019 is used as a calibration reference to the most critical parameters, such as the fractal dimension and breakage coefficient. Moreover, Gillard et al. in 2019 has measured the settling velocity of the flocs, which are utilized to calibrate the settling velocity closure, a critical parameter in the model. After gaining enough confidence from the previous validation and calibration process, a real case scenario is created to investigate the effect of flocculation on turbidity flows in the near-field

region. Thus, a comparison was made between the cases with and without flocculation, resulting in the first qualitative data on the effect of flocculation on turbidity currents in the near-field region. The results have shown that the aggregation process is prevalent and the particle size distribution within the mixture changes significantly across the near-field region. However, upon further analysis of the layer-averaged parameters of the side-ways turbidity current, it was found that the observed differences in hydrodynamics were not significant.

Finally, the numerical model is used to study the impact of various design and operational conditions, by varying discharge velocity, concentration, ambient current velocity, collector velocity on the behavior of turbidity flows in the near-field region. The results suggest that certain parameters can increase the flocculation rate, such as increasing the discharge concentration, collector velocity, and ambient current velocity. The results also highlighted the complex interplay between the discharge concentration, velocity ratio between discharge and collector, and initial concentration. Notably, in some cases, the turbidity current can even advance the collector. In conclusion, the numerical model analysis presented in this thesis provides a comprehensive understanding of the behavior of turbidity flows in the near-field region and highlights the significant impact of various design and operational conditions. These findings shed new light on the complex interplay between multiple factors and offer invaluable insights for optimizing the collector framework design, paving the way for mining activities with acceptable environmental impact.

Samenvatting

De uitputting van terrestrische minerale afzettingen en de toenemende vraag naar mineralen veroorzaken verstoringen in de wereldwijde toeleveringsketen. De verschuiving naar hernieuwbare technologieën vereist aanzienlijke hoeveelheden metalen die bijvoorbeeld worden gebruikt bij de productie van elektrische voertuigen en windturbines, waardoor de toeleveringsketen extra onder druk komt te staan. De diepzeebodem bevat aanzienlijke reserves aan mineralen die bijna een eeuw geleden werden ontdekt maar door gebrek aan technologie en vraag onbenut bleven. Met de huidige technologische vooruitgang en vraag kan commerciële winning in de komende jaren worden gestart. Diepzeemijnbouw brengt verschillende uitdagingen met zich mee vanwege de gevoelige aard van de diepzee. De impact van mijnbouwactiviteiten op de omliggende regio wordt mogelijk beïnvloed door een turbiditeitsstroom, welke wordt gegenereerd door de mijnbouwapparatuur. Deze turbiditeitsstroom kan aanzienlijke schade toebrengen aan het kwetsbare mariene ecosysteem.
In deze context tracht deze studie tot een uitgebreid inzicht te komen van de turbiditeitsstroming die het gevolg zijn van de winning van polymetallische nodulen, een soort diepzee-afzetting. Om deze turbiditeitsstroom te ontginnen, is speciale apparatuur nodig, zoals een collector, een verticaal transportsysteem en een ondersteuningsschip. Tot op heden is de meest volwassen technologie die in dit proces wordt gebruikt de hydraulische collector, die over de zeebodem beweegt en de nodulen verzamelt. Nadat de nodulen zijn verzameld door de hydraulische collector, wordt een verticaal transportsysteem gebruikt om ze over te brengen naar een ondersteunend schip. Op het schip worden denodulen zorgvuldig behandeld terwijl de resterende effluenten terug in de waterkolom worden geloosd. Tijdens het verzamelproces wordt onvermijdelijk een mengsel van water en sediment samen met denodulen verzameld. Dit mengsel wordt via de achterkant van de collector in de omgeving afgevoerd. Dit proces verhoogt het turbiditeitsniveau van de omgeving en waarschijnlijk ook buiten

het mijngebied, waardoor het risico bestaat dat de flora en fauna in de diepzee verloren gaan.
Deze studie begint met het onderzoeken van de state-of-the-art kennis van het fysische gedrag van de desbetreffende stromingen en vergelijkt deze met pluimen, jets en turbiditeitsstroming nabij de collector, resulterend in een classificatie van stromingstypes, lengte- en tijdschalen in het near-field-gebied, dat de basisprincipes van de overeenkomstige turbiditeitsstroming behandelt. Bovendien heeft dit literatuuronderzoek concludeerd dat het gebruik van een 2D Lagrangiaans model, ontwikkeld door Lee et al in 2013, geschikt is om het gedrag van het water-sedimentmengsel in de jet/pluimte voorspellen. De resultaten van het 2D Lagrangiaans model worden gebruikt als input voor het model van Parker et al. in 1987. Deze koppeling maakt het mogelijk om de impact van verschillende afvoerscenario's te onderzoeken. Daarnaast wordt een specifiek scenario met variërende deeltjesgrootte onderzocht om het effect van flocculatie op het verloop van de stroming te onderzoeken. De resultaten laten zien dat de karakteristieken van de gegenereerde turbiditeitsstroming sterk afhankelijk zijn van de ontladingsomstandigheden en de deeltjesgrootte. Dit beargumenteerd verder experimenteel onderzoek naar turbiditeitsstroming, inclusief verschillende begincondities en gedetailleerde metingen voor validatie van numerieke modellen.
In het baggerlab van de Technische Universiteit Delft wordt een reeks sluis experimenten uitgevoerd. Verschillende soorten sediment, met verschillende deeltjesgrootteverdelingen, worden getest. Hogesnelheidscamera's en een gespecialiseerde kalibratiemethode voor pixelconcentratie worden gebruikt om de lokale concentratie op verschillende lengte- en tijdschalen van de stroming te meten. De experimentele resultaten laten zien dat hoge initiële concentraties sediment met lage deeltjesgrootte hoge frontsnelheden opleveren. Naarmate de beginconcentratie echter tot een bepaalde drempel overstijgt, begint de deeltjesgrootte zijn effect op de stroom te verliezen. Dit houdt in dat een lage concentratie en grotere deeltjesgroottes gunstiger zijn in het botsingsgebied. Bovendien wordt de gemeten concentratieverdeling van deze experimenten gebruikt om een nieuw geïmplementeerd numeriek mengselmodel te valideren, zoals voorgesteld door Goeree et al in 2016. De snelheid en concentratieprofielen van het numerieke model bleken goed overeen te komen met die in het experimentele model.
Het model werd verder uitgebreid door de populatiebalansvergelijking op te nemen met het driftfluxmodel om rekening te houden met de flocculatiedynamiek. Het experimentele werk van Gillard et al. in 2019 wordt gebruikt

als kalibratiereferentie voor de meest kritische parameters, zoals de fractale dimensie en breukcoëfficiënt. Bovendien hebben Gillard et al. in 2019 de bezingsnelheid van de vlokken gemeten, die worden gebruikt om de sluitingsrelatie van de bezinkingssnelheid te kalibreren, een kritische parameter in het model. Nadat voldoende vertrouwen is verkregen uit het vorige validatie- en kalibratieproces, wordt een realistisch scenario gesimuleerd om het effect van flocculatie op turbiditeitsstroming in het nabije veldgebied te onderzoeken. Aldus werd een vergelijking gemaakt tussen de situaties met en zonder flocculatie, wat resulteerde in de eerste kwalitatieve afschatting van het effect van flocculatie op turbiditeitsstroming in het nabije veldgebied. De resultaten hebben aangetoond dat de deeltjesgrootteverdeling binnen het mengsel aanzienlijk verandert in het nabije-veldgebied. Bij verdere analyse van de laaggemiddelde parameters van de zijwaartse turbiditeitsstroming bleek echter dat de waargenomen verschillen in hydrodynamica niet significant waren.
Ten slotte wordt het numerieke model gebruikt om de impact van verschillende ontwerp- en operationele omstandigheden te bestuderen, door de afvoersnelheid, concentratie, omgevingsstroomsnelheid en collectorsnelheid te variëren op het gedrag van turbiditeitsstroming in het nabije veldgebied. De resultaten suggereren dat bepaalde parameters de flocculatiesnelheid kunnen verhogen, zoals de ontladingsconcentratie, collectorsnelheid en omgevingsstroomsnelheid. De resultaten benadrukten ook het complexe samenspel tussen de ontladingsconcentratie, de snelheidsverhouding tussen ontlading en collector en de initiële concentratie. Met name kan de turbiditeitsstroming in sommige gevallen zelfs de collector voorbij gaan.. Concluderend, de numerieke modelanalyse die in dit proefschrift wordt gepresenteerd, biedt een uitgebreid begrip van het gedrag van turbiditeitsstroming in het near-field-gebied en benadrukt de significante impact van verschillende ontwerp- en operationele omstandigheden. Deze bevindingen werpen een nieuw licht op het complexe samenspel tussen meerdere factoren en bieden waardevolle inzichten voor het optimaliseren van het ontwerp van het collectorraamwerk, wat de weg vrijmaakt voor mijnbouwactiviteiten in de diepzee met een aanvaardbare milieu-impact.

List of Tables

2.1 Estimated discharge conditions for various DSM cases for PNMT 18
2.2 Fraction distribution of sediment in the CCFZ (GSR, 2018; Zawadzki et al., 2020). 26
2.3 Percentages of mineral groups in clay in the CCFZ (Bischoff et al., 1979; Maciąg & Harff, 2020; Zawadzki et al., 2020). 26
2.4 Different entrainment coefficients values reported in the literature; 'J' is the jet type flow, 'P' is the plume type flow, 'L' is liquid, 'P' is pipe and 'c' is constriction. For method, 'w' is hot wire probe and 'l' is laser Doppler anemometer; z^* is the ratio z/d in which z is the distance from the source and d is the discharge diameter (Carazzo et al., 2006b). 35

3.1 Clay parameters used in the calculations of the erosion rate. . . . 44
3.2 Initial conditions of the numerical runs and the numerical results; V_e, $\alpha_{t,e}$, d_e and $V_e\alpha_{t,e}d_e$ are the results at the impingement point, while U_e, C_e, h_e and $U_eC_eh_e$ are the results at 100 m downstream the impingement point. 45

4.1 Main parameters of the experimental runs. 60
4.2 D_{10}, D_{50} and D_{90} in μm for Type1 and Type2. 60
4.3 Step-by-step sediment addition and sediment concentration ranges. 61
4.4 Values of b_1 and b_2 used for the three sediment types. The typical values of b_1 and b_2 are $18 < b_1 < 24$ and $1 < b_2 < 1.2$. 72

5.1 The values of d_f and E_b used in the numerical runs. 106
5.2 Boundary condition set up at different positions for all variables. 108

6.1 Test matrix showing various discharge scenarios from a PNMT. . 125

6.2 Summary of group comparisons: runs and associated discharge velocity 139

List of Figures

1.1 Marine mineral distribution on different topographic feature of the sea floor. Adopted from Sharma (2015). 2
1.2 (a) Top view of the ocean floor in CCFZ region at 4900 depth. (b)X-ray scan of a polymetallic nodule (Hein et al., 2020). 4
1.3 Polymetallic nodules deep sea mining system (Cuyvers et al., 2018). 6
1.4 Types of the sources of sediment plumes near the sea bed (MIT Mechanical Engineering, 2019). 7
1.5 Classification of turbidity flow in the near-field region. Particle size development by means of the flocculation process in the near-field region. 9
1.6 Outline of this dissertation. 11

2.1 Conceptual sketch of the evolution of the sediment-water mixture discharged from PNMT (near-field area). 19
2.2 An overview of the most relevant length scales accompanying DSM activities based on the work of (Fernando, 2012). 20
2.3 An overview of the most relevant time scales accompanying DSM activities based on the work of (Fernando, 2012). 20
2.4 Schematic diagram of a turbulent jet generated from slot. ZFE and ZEF regions are shown along the jet trajectory (J. H. Lee et al., 2003). 24
2.5 Forces acting on a non rotating settling particle in a quiescent flow, where F_g is the gravitational force, F_b is the buoyancy force, F_d is the drag force and u_{kr} is the settling velocity (J. Goeree, 2018). . 25
2.6 The structure of the head of a turbidity current (Middleton, 1993). 30
2.7 Gaussian and top hat profiles (McKernan et al., 2007), $b(x)$ is the mixing layer width. 32

3.1 Definition sketch for the case considered including a generated plume and turbidity current. 42
3.2 Comparison of the numerical results using different initial momentum fluxes; spatial evolution of a plume (**left**) and spatial evolution of a turbidity current (**right**). 49
3.3 Comparison between the numerical results of a run including the flocculation effect (dashed lines) and a run excluding the flocculation effect (solid lines). 51

4.1 Conceptual sketch of the evolution of the sediment–water mixture discharged from a PNMT. (**a**) Top view of the discharge process from a PNMT; (**b**) right-side view of the discharge process from a PNMT (Elerian et al., 2021); (**c**) section A-A shows the direction of a turbidity current. 57
4.2 Schematic representation of the tank used in the experiments. The dimensions of the lock and the tank and the water depth are shown. 59
4.3 (**a**) Final setup of the tank with the diffused light. The black tent is used to create the maximum contrast; (**b**) side view of the tank setup showing wooden panel with LED stripes; (**c**) side view of the LED stripes and the diffused paper in front of it; (**d**) the high speed/definition camera used in the experiments. 59
4.4 Shades of grey for Type1 sediment. 61
4.5 Calibration curve for one of the pixels for Type1 sediment. 62
4.6 Front position of the turbidity currents x_n as a function of the propagation time t. 65
4.7 Time needed by the current to reach the end of the visualized region as a function of the initial concentrations. 66
4.8 Log-Log plot of dimensionless time, T, vs. dimensionless front positions for all experimental runs. The solid lines represent the slopes 1 and 2/3 for the long and short lines, respectively. The right figure provides a more detailed look at the transition point of the current from slope 1 to slope 2/3. 67
4.9 Comparison of the concentration distribution of the currents. The rows represent the same initial concentration and the columns represent the same sediment type. All the runs are acquired at the same front position. 68
4.10 Geometry, mesh and boundary conditions used in the numerical simulations. 74

4.11 Grid-dependency study of numerical Run7. The front position of the current is plotted with respect to time for three different 2D meshes and one 3D mesh. 75

4.12 Sensitivity analysis for the number of the used fractions in the case of numerical run15. The front position of the current is plotted with respect to time for the number of used fractions of 1, 12, 24 and experimental results. 76

4.13 Validation cases for runs 1, 7 and 15. Front velocities of the numerical runs are compared to experimental runs. 78

4.14 Validation case for run1. Vertical concentration profiles are shown for the front and the body of the current. The first snapshot is taken when the front of the current has almost reached the middle of the tank. 79

4.15 Validation case for run7. Vertical concentration profiles are shown for the front and the body of the current. The first snapshot is taken when the front of the current has almost reached the middle of the tank. 80

4.16 Validation case for run15. Vertical concentration profiles are shown for the front and the body of the current. The first snapshot is taken when the front of the current has almost reached the middle of the tank. 81

5.1 Aggregation an breakage dynamics of the discrtized PBE, Equation 5.2, adapted from (Biggs & Lant, 2002). Following Equation 5.2, first term is formation of floc k due to collision of unequal particle sizes, second term is formation of floc k due to collision of equal particle sizes, third term is death of floc k due to collision with smaller particles, fourth term is death of floc k due to collision with equal or large particles, fifth term is death of floc k due to breakage, sixth term is formation of floc k due to breakage of large particles. 91

5.2 Flow chart of the solver algorithm in OpenFOAM. 96

5.3 PSD of the 8 MUC location in the CCZ Gillard et al., 2019. The blue points represents the corrected 27 fractions used in this chapter. 97

5.4 (a) Couette reactor setup. (b) The 2D mesh used in numerical runs. 99

5.5 Calibration of the modeled settling velocity u_{kr} using the experimental results of (Gillard et al., 2019). (A): calibration process for 500 mg/l and 10.4 s^{-1}. (B): calibration process for 175 mg/l and 5.7 s^{-1} . (C): calibration process for 105 mg/l and 2.4 s^{-1}. . . . 101

5.6 Calibration process in case of 500 mg/l mass concentration and 10.4 s^{-1} shear rate. All 3 figures show the development of d_{50} over time. (A) represents the sensitivity of the fractal dimension d_f on the numerical results, where the the breakage coefficient $E_b = 1 \times 10^{-6}$ is constant. (B) represents the sensitivity of the breakage coefficient, where for blue curves the $d_f = 2.3$ is constant. (C) represents the sensitivity of both parameters d_f and E_b on the development of d_{50}. 102

5.7 Calibration process for 175 mg/l mass concentration and 5.7 s^{-1} shear rate. All 3 figures show the development of d_{50} over time. (A) represents the sensitivity of the fractal dimension d_f on the numerical results, where the the breakage coefficient $E_b = 1 \times 10^{-6}$ is constant. (B) represents the sensitivity of the breakage coefficient, where for blue curves the $d_f = 2.3$ is constant. (C) represents the sensitivity of both parameters d_f and E_b on the development of d_{50}. 102

5.8 Calibration process in case of 105 mg/l mass concentration and 2.4 s^{-1} shear rate. All 3 figures show the development of d_{50} over time. (A) represents the sensitivity of the fractal dimension d_f on the numerical results, where the the breakage coefficient $E_b = 1 \times 10^{-6}$ is constant. (B) represents the sensitivity of the breakage coefficient, where for blue curves the $d_f = 2.3$ is constant. (C) represents the sensitivity of both parameters d_f and E_b on the development of d_{50}. 103

5.9 Geometry used in all numerical simulations with the name of the relevant B.C. The top figures depict half of the domain, utilizing symmetry B.C as indicated by the red tag, while the bottom figures show the geometry for the PNMT. The unrepresented half of the domain is mirrored along the ZX plane for post-processing analysis. The flow direction is in the positive X direction with a positive discharge. 107

5.10 Comparison of sediment flux in coarse, medium and fine mesh. In each case, three x-normal slices are considered at 50 m, 80 m and 110 m. 109

5.11 Fraction fluxes across the the three x-normal slices, slice1 at 50m, slice2 at 80m and slice3 at 110m. (A) α_t flux, (B) α_2 flux , (C) α_{22} flux , (D) α_{28} flux 110
5.12 Z-normal sections for the flocculation and no flocculation cases are taken at the BOTTOM boundary **(left)** and 1m from the bottom **(right)**. The top row shows the no-flocculation case, while the lower row shows the flocculation case. 112
5.13 Z and X normal sections show the relative differences between the flocculation and no-flocculation cases. The Z-normal sections are taken at the BOTTOM boundary **(left)** and 1m from the bottom **(right)** which is section C-C, while the X-normal sections are taken at 50m and 110m from the INLET boundary. 113
5.14 Layer-averaged parameters of the sideways turbidity current. The flocculation scenarios are compared on the left, where the fractal dimension d_f and the breakage coefficient E_b are changing. The graphs on the right compare the flocculation scenario and no-flocculation scenario. 115

6.1 Steady state analysis of two distinct groups of runs at different locations: 35m **A** and 70m **B**. 128
6.2 The impact of PNMT Forward velocity on volumetric concentration and shear rate for Runs 1 and 3. The figures present Z-normal sections at a distance of 1 cm from the bottom. 129
6.3 The impact of PNMT Forward velocity on volumetric concentration and shear rate for Runs 2 and 5. The figures present Z-normal sections at a distance of 1 cm from the bottom. 130
6.4 Examining the influence of PNMT forward velocity on sideways-propagating turbidity currents in Runs 1, 2, 3, and 5. An YZ plane section captured at the Steady State Location of 70m from the INLET Boundaries. Example of the Sideways-Propagating Turbidity Current Shown in Panel A 131
6.5 Normalised total sediment flux (**left**) and normalised largest fraction flux, α_{28} (**right**). A 4m profile at 70m in X and 25m in Y direction is taken to examine the side way turbidity current. . . . 133
6.6 Comparing total Sediment, largest Fraction (α_{28}), and side-way Velocity (y direction) in Runs 1 3 (**left**) and Runs 2 5 (**right**). A 4m profile at 70m in X and 25m in Y direction is taken to examine the side way turbidity current. 134

6.7 The volumetric concentration and shear rate are shown at two depths, 1 cm and 100 cm from the bottom, in the left and right columns, respectively. The top two figures show the difference in the total volumetric concentration ($\alpha_{t,diff}$), the middle two figures show the difference in the volumetric concentration of the largest flocs $\alpha_{28,diff}$, and the bottom two figures show the difference in the shear rate of the largest flocs. The $U_{a.v}$ is the ambient velocity. 136

6.8 Comparing normalised total Sediment flux, total sediment distribution, largest Fraction (α_{28}), and side-way Velocity (y direction) in Runs 1 and 6. A 4m profile at 70m in X and 25m in Y direction is taken to examine the side way turbidity current. The $U_{a.v}$ is the ambient velocity. 138

6.9 The effects of discharge velocity on volumetric concentration and shear rate differences are compared at a distance of 1cm. Runs 1 and 2, and Runs 3 and 5, have the same discharge velocities of 0.5 m/s and 0.75 m/s, respectively. In contrast, Runs 8 and 9 have lower and higher discharge velocities of 0.25 m/s and 0.75 m/s, respectively. 140

6.10 The normalised sediment flux **(left)** and the normalised largest fraction flux **(right)** for groups of runs of (1,2), (3,5), (8,9).. For Runs 8 and 9, the 4m profile is captured at the intersection of 35 in the X direction and 30 in the Y direction 142

6.11 The total volumetric concentration **(left)** and velocity profiles **(right)** for group of runs of (1,2), (3,5), (8,9). For Runs 8 and 9, the 4m profile is captured at the intersection of 35 in the X direction and 30 in the Y direction. 143

6.12 The volumetric concentration field and shear rates for Runs 7, 1, and 10 on the left and right are shown here. In these runs, the PNMT forward velocity is 0.5 m/s. 145

6.13 The volumetric concentration field and shear rates for Runs 8, 4, and 11 on the left and right are shown here. In these runs, the PNMT forward velocity is 0.25 m/s. 146

6.14 Sections of the PNMT region in Runs 4 and 11 demonstrate the potential for turbidity currents to flow beneath the PNMT and advance the collector over time. 147

6.15 This plot shows four variables at the intersection of 70 in the X direction and 30 in the Y direction: the total sediment flux **(top-left)**, the largest fraction flux **(top-right)**, the sideways propagating current velocity **(bottom-left)**, and the total volumetric concentration **(bottom-right)**. 149
6.16 This plot shows the integration of the sediment flux **(left y axis)** and α_{28} flux **(right y axis)**, for the 4 variables of interest, namely PNMT velocity **(top-left)**, discharge velocity **(top-right)**, ambient velocity **(bottom-left)**, and the initial concentration **(bottom-right)**. 150
6.17 This plot shows the integration of the sediment flux **(left y axis)** and α_{28} flux **(right y axis)**, for a changing velocity ratio. 151

Chapter 1

Introduction

1.1 Background

At the United Nations Climate Change Conference in 2015, the attendees agreed to a legally-binding international treaty that was approved by nearly all countries to combat climate change (United Nations, 2015). This treaty is known as the "Paris Agreement". To meet this agreement, the European Union (EU) has set a target of generating at least 32.5% of its energy from renewable sources by 2030 (Bobba et al., 2018). Achieving this goal will require critical raw materials such as lithium, cobalt, and rare earth metals, which play a significant role in the development of renewable technologies like wind turbines, electric vehicles, and solar panels (Guillaume, 2023). In addition, the decreasing diversity of supply for these materials also makes their availability a potential risk for the production of clean technologies. This is part of the EU's effort to reach a climate neutral continent.

The growing demand for metals has created pressure on the worldwide supply chain, resulting in the depletion of terrestrial deposits. As a result, extracting these metals has become more challenging and expensive. This strain has caused a number of issues, including higher prices, supply shortages, and increased competition for resources. Given the challenges facing the global supply chain for metals and other resources, the interest has increased to

consider unconventional sources that may provide access to new supplies of critical raw material. One such source is the deep sea, which is known to be rich in metals such as cobalt, nickel, and manganese, as well as other valuable minerals.

Just like the terrestrial landscape, the seabed is a complex and varied terrain, with a wide range of topographic features and geological structures. As shown in Figure 1.1, there are different forms of marine minerals that can be found on those terrains, including manganese nodules, cobalt crusts, and polymetallic sulfides. The extraction of marine minerals from the deep sea has been the subject of research and development for almost 7 decades, but interest in this area has increased significantly in the last decade (Miller et al., 2021). As a new industry in its feasibility testing phase, deep-sea mining (DSM) presents a range of challenges and potential impacts, including environmental pressures such as noise, light, and sediment clouds, which require careful consideration and management.

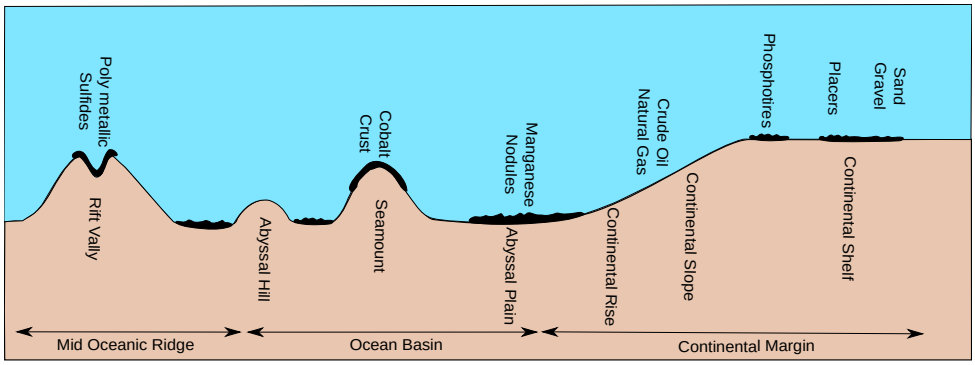

Figure 1.1: Marine mineral distribution on different topographic feature of the sea floor. Adopted from Sharma (2015).

In polymetallic nodules mining, which is the main topic of this study, the mining process can generate large amounts of sediment, which can be dispersed as a plume/turbidity current in the water column (Muñoz-Royo et al., 2022). This turbidity current can travel kilometers and can potentially have significant impacts on the surrounding ecosystem (Sharma, 2015). In addition to the increased turbidity level in the water column caused by the plume or turbidity current, the fresh sediment deposited from them can clog the feeding paths of benthic organisms. To minimize these impacts and their extent, it is important to carefully assess and manage the potential impacts

of sediment plume and the turbidity current on the surrounding ecosystem, (Cuyvers et al., 2018; Hein et al., 2020).

Polymetallic nodules are a type of marine mineral deposit found on the ocean floor of the abyssal plains at depths of 4-6 km. They are formed over millions of years as minerals precipitate out of the seawater and accumulate around a nucleus, such as a rock or a shell fragment (Hein et al., 2020). In recent years, advances in ocean engineering and geo-engineering technologies have enabled the discovery of large deposits of polymetallic nodules on the deep-sea floor. Acoustic mapping conducted by Wong et al. (2020) has estimated that the Clarion-Clipperton Fracture Zone (CCFZ) in the northeast equatorial Pacific contains approximately 21 billion dry tons of polymetallic nodules, which are known to hold over 6 billion dry metric tons of valuable metals such as manganese, nickel, copper, and cobalt (Petersen et al., 2016). The discovery of those nodules in the CCFZ and other areas of the deep-sea floor has generated interest in the potential for DSM operations to extract these valuable minerals (Figure 1.2) (Hein et al., 2020).

One of the key challenges of polymetallic nodules mining is the development of the technology that can extract the minerals from the seabed in an efficient, cost-effective manner and with limited and acceptable environmental impact. This includes the development of specialized equipment and techniques to safely and accurately extract the minerals from the seabed. Due to the technical challenges and potential impacts of polymetallic nodules mining, various companies and research institutes around the world are working together to develop the technology and expertise needed to extract these minerals. These collaborations are focused on developing new technologies and solutions that can help to reduce the cost of production, increase efficacy and mitigate environmental pressure.

Interest in mining marine minerals has focused primarily on international waters, which has led to a need for regulating deep-sea mining (DSM) activities in these areas. Consequently, the International Seabed Authority (ISA) was established as an intergovernmental organization to manage, regulate, and control all mineral-related activities in the international seabed area for the benefit of humankind, as stipulated by countries that signed the United Nations Convention on the Law of the Sea (UNCLOS). Since 2001, ISA has signed contracts with 29 contractors for exploring deep-sea minerals, including polymetallic nodules.

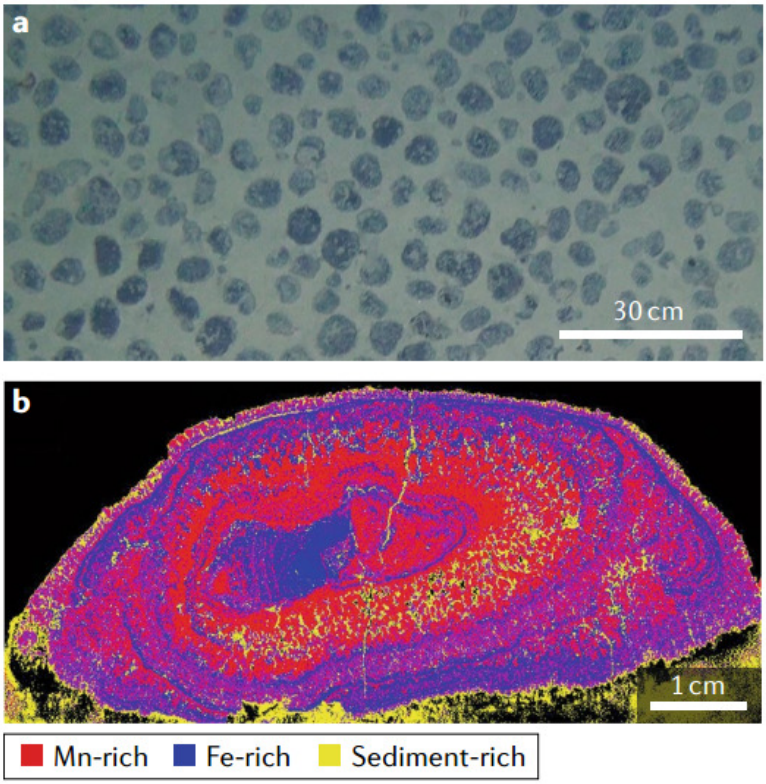

Figure 1.2: (a) Top view of the ocean floor in CCFZ region at 4900 depth. (b)X-ray scan of a polymetallic nodule (Hein et al., 2020).

While there are various technologies and visions for mining polymetallic nodules, this thesis focuses primarily on hydraulic PNMT, which is currently the most mature technology in the field of polymetallic nodules mining. A polymetallic nodules mining system is composed of three main parts, namely the PNMT, the Vertical Transport System (VTS), and the Production Support Vessel (PSV). The PNMT collects the nodules from the sea floor and primarily separates the nodules from the excess water and fine sediments, which are discharged directly to the surrounding environment. The nodules are then transferred by the VTS to the PSV, where they are further separated from the containing Sediments, Waste, and Other Effluents (SWOEs). Finally, a VTS is used again to return the water-SWOEs mixture, to the deep sea. Figure 1.3 depicts a typical deep sea mining (DSM) system scenario. With this scenario,

there are four main sources of sediment plumes. Among these sources, three are located near the seabed, as illustrated in Figure 1.4.

1. The discharge of the sediment–water mixture from a PNMT, which remains after the separation process (Decrop & Wachter, 2019).
2. The SWOE discharge from the VTS after the end of the dewatering and ore handling process on the PSV (Rzeznik et al., 2019; van Grunsven et al., 2018).
3. The sediment disturbance resulting from the movement of the PNMT's tracks.
4. The sediment resulting from spillage that occurs during the hydraulic collection process.

Studying all sources of sediment plumes simultaneously can be challenging due to the significant variations among them. For example, the sediment disturbance resulting from PNMT activities such as discharge, spillage, and tracks interacts with the seabed (Figure 1.4), whereas the discharge from the VTS does not. To simplify the investigation, we will focus solely on the initial source of discharge from the PNMT.

One of the main classifications associated with PNMT turbidity flows is the division into two regions of interest: a near-field region and a far-field region. The near-field region is characterized by low length and time scales, typically in the order of meters and minutes. This region refers specifically to the area near the PNMT, where engineering solutions may have an impact. The far-field region, on the other hand, is beyond the near-field region, with typical length and time scales on the order of kilometers and days, respectively. The spatial and temporal scales associated with the transition between near and far field regions are not well understood. Although there is still much to be learned about the link between these regions, this classification allows for a solid understanding of the nature of flows in each region, which will likely impact the development process of the PNMT.

Predicting the fate of the sediment particles contained in the generated sediment plume/turbidity current is the fundamental focus of any near-field study. Yet, little is currently known about particle dynamics in the near-field

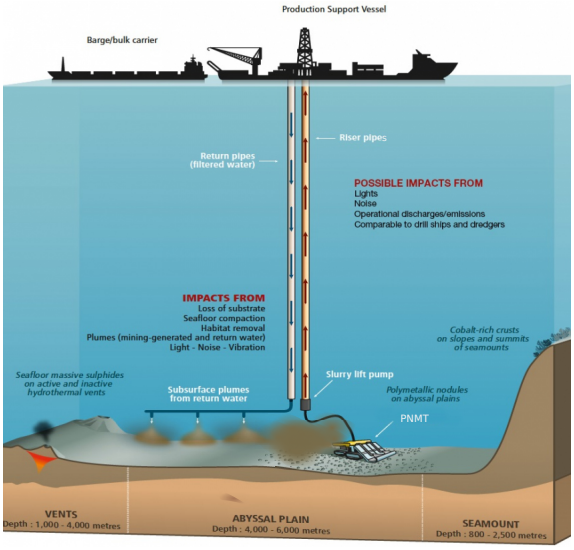

Figure 1.3: Polymetallic nodules deep sea mining system (Cuyvers et al., 2018).

area, as the presence of organic matter and the cohesive state of deep sea sediment introduce extra complications in understanding the behavior of turbidity flows. When sediment particles collide due to mixing, and in the presence of an organic substance, they may stick together to form a 'floc'. This is primarily because of the chemical interactions that occur between the surfaces of the two particles at the moment of collision. In the literature, this process is known as 'flocculation'. The details of flocculation mechanisms are unique to each sediment type, which adds complications to the prediction of particle dynamics.

Early efforts to characterize the flocculation process during DSM operations suggested that the aggregation process between sediment particles can increase the settling potential of the resulting suspended sediment from a mining operation (Gillard et al., 2019; Spearman et al., 2020). Therefore, the turbidity levels in both the near-field and far-field regions may decrease, reducing the environmental impact. Although mixing increases the probability of collisions and subsequent flocculation, excessive mixing can disrupt the newly-formed flocs and prevent further aggregation. It would therefore appear that the paramount to obtaining a deeper understanding of the turbulence structure in the wake region might introduce a thorough understanding to the flocculation

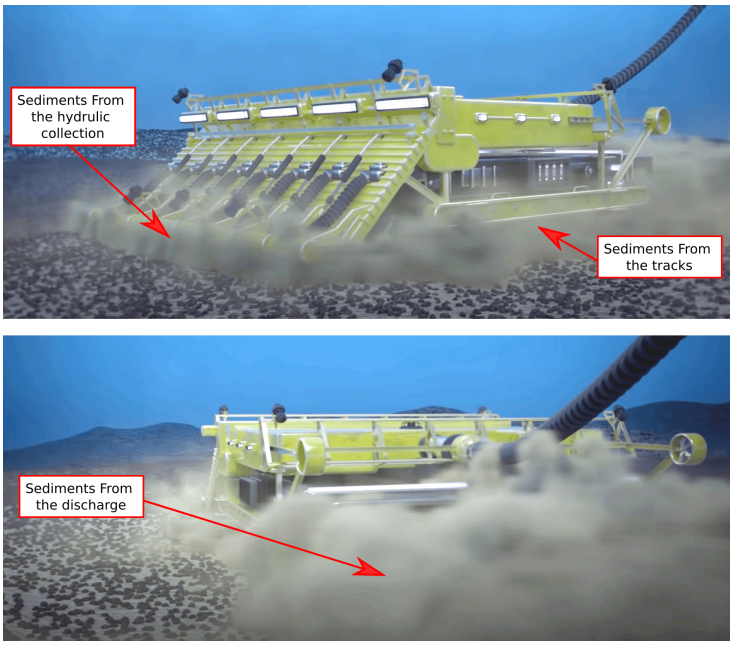

Figure 1.4: Types of the sources of sediment plumes near the sea bed (MIT Mechanical Engineering, 2019).

process.

1.2 Scope

Predicting the behavior of turbidity flows in the near-field region is crucial for accurately estimating their potential environmental impact. The water-sediment mixture's behavior in this region is commonly evaluated based on the discharge parameters, which dictate the dispersion trends of the resulting turbidity flows. Our current understanding of the structure of turbidity flows associated with discharge parameters in the near-field region is limited due to a lack of quantitative data on these currents. This makes it difficult to determine the role of flocculation in reducing the impact of these currents. While there have been some direct measurements of mixture velocity and concentration in the field, these measurements are limited and have not provided enough information to draw definitive conclusions (Figure 1.5). Therefore, acquiring a

comprehensive comprehension of the function of flocculation in the dispersion of turbidity currents can offer a viable approach for mitigating turbidity levels in the nearby vicinity.

Studying a full-scale discharge process in the field is a challenging and intricate task, as it requires comprehensive measuring techniques to accurately quantify the physical processes that occur during the mining process. This is, however, what took place in the work of Haalboom et al. (2023) and Muñoz-Royo et al. (2022). Even though conducting field experiments is still costly and difficult, as many variables are encountered in the problem. Thus, testing all discharge scenarios in the field seems unfeasible, not to mention the uncertainties resulting from the flocculation process. This highlights the importance of scaled-laboratory studies for gaining better insights into the influence of particle size and flocculation process on the turbidity-flows dispersion. This could be the key to the development of advanced numerical models that can accurately describe particle dynamics, allowing for the prediction of turbidity flows in the near-field region. This understanding of sediment dynamics can inform the design of the PNMT, ultimately leading to a conceptual framework for a PNMT with acceptable environmental impact. This study presents a newly-developed numerical model that can predict the development of near-field-generated turbidity flows, taking into account the influence of the flocculation process on the dispersion of the turbidity flows. The model considers the relevant discharge parameters and oceanic conditions in its predictions. Therefore, the numerical investigations presented in this study can provide a wealth of insights into the structure and physical behavior of turbidity flows in the near-field region, particularly with regard to dispersion trends, ultimately leading to a improved design of the PNMT.

1.3 Objectives and Research Questions

The design of a PNMT is crucial, as it directly affects the deep-sea environment. This can be achieved through conducting comprehensive laboratory experiments and numerical simulations of turbidity flows in the near-field region. These experiments and simulations focus on understanding physical processes, such as sediment transport, flocculation, and deposition, within the near-field region. This understanding will, in turn, lead to the development of an improved design framework for the discharge process. The objective

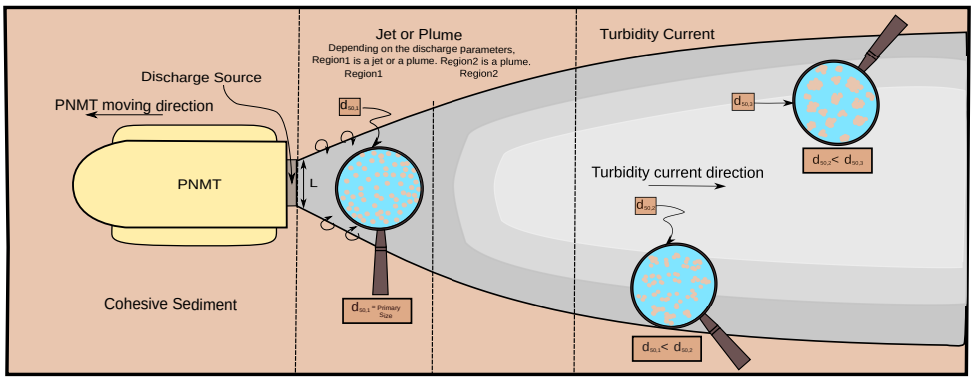

Figure 1.5: Classification of turbidity flow in the near-field region. Particle size development by means of the flocculation process in the near-field region.

of this study is to investigate the effects of flocculation on the dispersion of the generated turbidity current, as well as the influence of discharge parameters, including flow velocity and sediment concentration, on sediment plume/turbidity current dispersion. While the goal is not to provide exact values for these parameters, our aim is to develop a fundamental understanding of their impact on turbidity current dispersion in the near-field region. This knowledge will enable a deeper understanding of turbidity flow as a function of discharge parameters, sediment properties, mixture velocity and volume, and oceanic conditions. Therefore, the following research questions will be addressed within the context of the near-field region:

1. How do sediment particle size and concentration influence the development of the side-way propagating turbidity current?
2. How does flocculation influence the turbidity current behind the PNMT?
3. How do different system designs affect the dispersion of the generated turbidity current?

1.4 Dissertation Outline

The dissertation structure proceeds as follow (see fig.1.6): Chapter 2 surveys the essential state-of-the-art knowledge of generated turbidity flows behind

a PNMT. A detailed classification of the flow types in the near-field region is presented. Furthermore, Chapter 2 presents an analysis of the relevant length and time scales of the generated flows, after which the most important parameters that control the development of the turbid flows in the near-field region are investigated. The aim of this analysis is to provide a better insight into the main parameters that affect the plume/turbidity current dispersion in the near-field region.

In chapter 3, employing different discharge scenarios, the 2D Lagrangian model that was developed by Lee et al. (2013) and the layer-averaged four equation model of Parker et al. (1986) are utilized to predict the plume/turbidity current in the near-field region. One run is made with a changing particle size along the spatial and temporal scales of the generated turbidity current, in order to mimic the effect of the flocculation process. Furthermore a comparison between the flocculation case and the no-flocculation case is carried out, attempting to understand the effect of flocculation on the turbidity current evolution.

Chapter 4 focuses on the experimental and numerical modeling of turbidity currents. Prior to studying the flocculation process, it is crucial to understand the impact of particle size and varying concentration values on the development of turbidity currents. To achieve this, a lock-exchange experimental setup is employed using non-cohesive sediment. The results highlight the criticality of these parameters. Additionally, the drift-flux model is validated through a drift-flux modeling approach, and good agreement is found between the experimental and numerical results.

Chapter 5 presents the Population Balance Equation (PBE), which is coupled to the multi-fraction drift-flux model presented in Chapter 4. The PBE is responsible for modelling the flocculation process. The critical parameters of the flocculation process is calibrated using the experimental work of (Gillard et al., 2019). Furthermore, the new model is used to investigate the influence of the flocculation process in the near-field region for a moving PNMT.

Chapter 6 continues the investigation of the real-case studies, where different discharge parameters, such as initial velocities and concentration are investigated. The dispersion trends of turbidity flows in the near-field region are compared, yielding the first detailed and quantitative visualizations of sediment plumes in the near-field region.

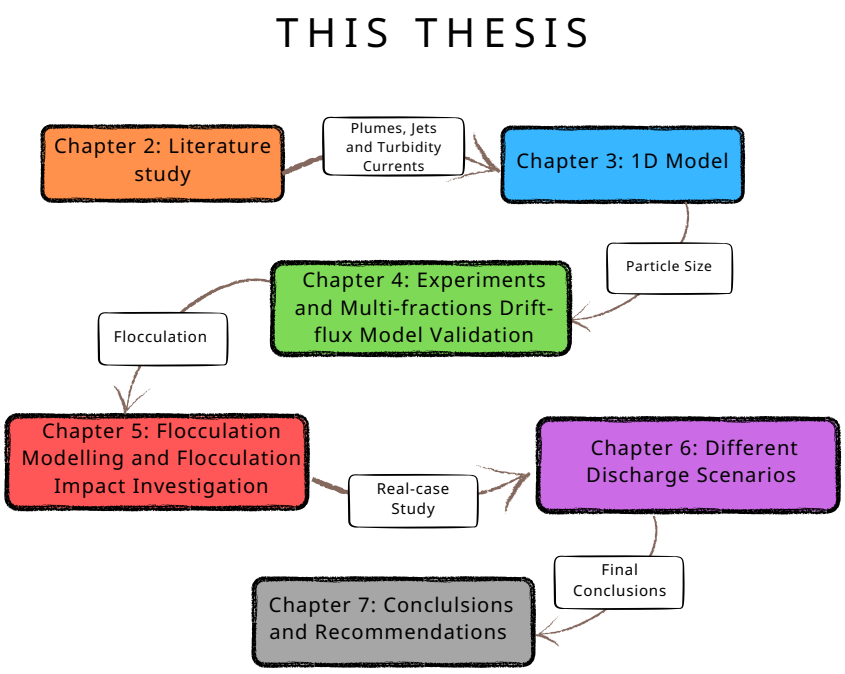

Figure 1.6: Outline of this dissertation.

In conclusion, chapter 7 of the dissertation addresses the research questions and offers recommendations for further experimental investigation in the field and the lab and numerical investigations. By doing so, it seeks to enhance our comprehension of the physical processes taking place in the near-field region and promote a more comprehensive approach to future research

Chapter 2

The State-of-The-Art-Knowledge

Abstract

This Chapter begins with surveying the-state-of-the-art knowledge of the evolution of the discharge from a PNMT, where discharge characteristics and generation of turbidity currents are discussed. Moreover, the existing water entrainment theories and coefficients are analysed. It is shown how plumes and jets can be classified using the flux balance approach.

Parts of this chapter have been published as Elerian, M.; Alhaddad, S.; Helmons, R.; van Rhee, C. Near-Field Analysis of Turbidity Flows Generated by Polymetallic Nodule Mining Tools. Mining 2021, 1, 251–278

2.1 Introduction

The effect of sediments disturbance resulting from DSM applications on the local physico-chemical conditions, i.e. soil composition and organic carbon content, of the disturbed area was investigated experimentally by Sharma et al. (2001). The physical parameters (e.g. velocity and concentration profiles) of sediment plumes resulting from dredging operations were studied by Decrop et al. (2013) and de Wit, van Rhee, et al. (2014). The work of Grunsven et al. (2018) documented numerical and experimental results of plume discharge from a VTS. A CFD analysis was performed by Decrop and Wachter (2019) for a horizontal discharge from a PNMT to investigated the effect of different discharge conditions (see the controlling parameters of a discharge process in Subsection 2.2.2) on the plume dispersion. A pre-prototype PNMT was developed and tested in the Belgian and German exploration areas; based on the results, a comprehensive monitoring program for the local environment was developed BGR (2019). The work of Spearman et al. (2020) and Gillard et al. (2019) showed that the particle size distribution (PSD) governed the travelling distance of fine suspended sediment. They found that the particle size changes as a result of the aggregation-breakup process between sediments (see Section 3.5 for more details about flocculation process).

In the last decades, valuable insight has been gained into DSM processes through various projects, where environmental impacts of DSM were investigated e.g. (Corliss, 1985; Department of Commerce, 1977; Muñoz-Royo et al., 2021; Oebius et al., 2001; Reichart et al., 2013; Schriever & Thiel, 2013; Sharma et al., 2001; Spearman et al., 2020; Thiel, 2003; Thiel et al., 1989). Some of DSM research projects are mentioned as follow:

- The DOMES (Deep Ocean Mining Environmental Study) project was one of the leading projects, which aimed to obtain and investigate the necessary data for an independent impact assessment of DSM activities. DOMES was divided into two main phases as follows (Department of Commerce, 1977):

    1. Gaining quantitative data on the biological communities prior to mining and developing a framework to predict the impact of manganese nodule mining on the marine environment;

2. Determining the accuracy of the environmental impact predictions obtained in the first phase through monitoring of pilot mining tests;

As a result of this project, a quantitative baseline of environmental parameters and a predictive framework were developed to characterize DSM environmental impacts. Furthermore, preliminary environmental guidelines for DSM were defined;

- The Marine E-tech project took place in the Tropic Seamount in the north east Atlantic near the Canary Islands and aimed to study the environment sensitivity to Fe-Mn crusts DSM operations. The Fe-Mn crusts differentiate from polymetallic nodules as a result of different locations, depths and DSM operation techniques. The local influencing variables (e.g. temperature, pressure) that govern the composition and formation of the Fe-Mn nodules were investigated. An ROV (Remotely operated underwater vehicle) was used to generate sediment plume and the plume dispersion was studied. The measurements showed that the plumes were significantly smaller than predicted because the effect of flocculation was not taken into account (Spearman et al., 2020);

- The TREASURE (Towards Responsible Extraction Of Submarine Mineral Resources) project studied SWOE discharge from the VTS (Reichart et al., 2013). Within the scope of TREASURE, numerical simulations were performed using drift-flux modelling approach (for details on drift-flux modelling, see J. Goeree (2018) to predict the VTS discharged plume characteristics (e.g. velocity and concentration) (Grunsven et al., 2016). In addition, Grunsven et al. (2018) carried out detailed laboratory experiments to test different discharge parameters such as initial concentrations, momentum and distance to the bed on the plume dispersion. The numerical results (e.g. velocity and concentration profiles) were compared against the experimental results and good agreement was found between them;

- The PLUMEX2018 field experiments were conducted in the Southern California Bight at the beginning of 2018 (Kulkarni et al., 2018). MIT-MSEAS model (multi-resolution primitive equation regional ocean modeling system) was used to predict the plume dispersion, i.e. direction, velocity and concentration. Good agreement was found between the

MIT-MSEAS model and the PLUMEX field experiments (Muñoz-Royo et al., 2021);

- JPI-Oceans Mining Impact II research project aimed to develop a new framework for environmental monitoring and predictions for the environmental impacts of mining operations (Haeckel, 2018). Global Sea Mineral Resources (GSR), a subsidiary of DEME group, designed and tested a PNMT in Clarion-Clipperton Fracture Zone (CCFZ) within the Belgian license area to assess its environmental impact (BGR, 2019). GSR performed detailed measurements about the current environment (climate, geo-morphological, physical oceanographic, seabed substrate characteristics, natural hazards, noise and light). Moreover, a biological baseline was assessed based on habitat heterogeneity. The potential environmental impact was divided into six categories:

  1. habitat/nodule removal;
  2. plume formation;
  3. biogeochemical changes of the sediment particles;
  4. potential release of toxic sediment into lower water column;
  5. emissions to air;
  6. natural hazard (weather condition, storms).

The objective of this chapter is to present an analysis of the characterizations of plumes generated by PNMT in terms of transport, spreading and deposition of sediments. This will help determine the optimal discharge conditions to minimize the environmental impact caused by sediment plumes. In this regard, the emphasis will be on the near-field effects (see subsection 2.2.1 for the near/far field definitions), where engineering and design of equipment can significantly influence the spread and deposition of the generated plume.

This chapter proceeds as follows. An overview of the discharge process and the key parameters controlling it are provided. Moreover, we present the relevant length and time scales associated with polymetallic nodules mining process and an overview of sediment-laden jets and plumes. The most important physical aspects of jets, plumes, and turbidity currents analyzed.

2.2 Discharge Process

In this section, we first present an overview of the PNMT discharge process in order to study the turbidity flows generated by DSM. Secondly, a classification of the discharge properties and the physical parameters of the PNMT discharge process are described.

2.2.1 Overview

The main differences between the two discharge sources in a polymetallic nodules mining operation are the orientation (vertical from the VTS and mostly horizontal from the PNMT), distance to the seabed, flow rate and concentration of the suspended sediments. Some studies showed that the SWOE discharge location ranges from near the seabed to just below oxygen minimum layer (800-1,000 m water depth) (Grunsven et al., 2018; Oebius et al., 2001; Rzeznik et al., 2019; Schriever & Thiel, 2013), while distance to the seabed of a PNMT depends on the discharge position on the PNMT, ranging from 1 to 3 m. SWOE discharge flow rate and concentration are estimated to be about 0.56 m^3/s and 8 g/L, respectively (Muñoz-Royo et al., 2021; Oebius et al., 2001). Table 2.1 shows the estimated solid flux rate and sediment concentration range of a PNMT discharge.

Bed disturbances mainly result from the movement of a PNMT and the pick-up process (Sharma et al., 2001), which could be hydraulic, mechanical or hybrid. A benthic disturbance experiment mimicking PNMT disturbances was conducted to investigate particles resettlement on marine ecosystem during DSM operation (Sharma et al., 2001). They found that the particles migrate to the adjacent areas outside the mining zone, causing a change in physico-chemical bed properties. These migrated particles potentially clog the feeding paths of the benthic organisms.

Discharging these sediment-water mixtures without carefully optimizing the discharge parameters might unnecessarily enlarge the area affected by plume dispersion. A few studies are found in the current body of the research about the discharge process from the PNMT e.g. (Decrop & Wachter, 2019). In this respect, we present in Section following Chapter3 our investigation of the sediment-water discharge from a PNMT. We divide the horizontal discharge

Table 2.1: Estimated discharge conditions for various DSM cases for PNMT

Application	Solid Flux Per Unit Width	Concentration Range	D_{10}	D_{50}	D_{90}
Seafloor Massive Sulfides (SMS) (Verichev et al., 2014)	163 kg/s	250 g/L	9 *mum*	40 *mum*	70 *mum*
Nodules (Decrop & Wachter, 2019)	65.9–212.3 kg/s	10–170 g/L	-	10 *mum*	-
Nodules (Global Sea Mineral Resources NV, 2018)	65.9–212.3 kg/s	10–170 g/L	2 *mum*	15 *mum*	70 *mum*
Fe-Mn crusts (Spearman et al., 2020)	0.2 kg/s	20–100 mg/L	-	-	-
Phosphorite (Lescinski et al., 2014 b)	827 kg/s	449 g/L	10 *mum*	80 *mum*	300 *mum*

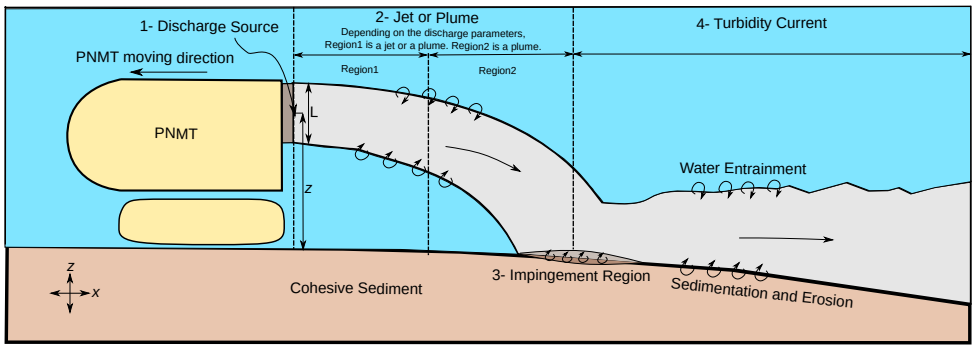

Figure 2.1: Conceptual sketch of the evolution of the sediment-water mixture discharged from PNMT (near-field area).

of a sediment-water mixture from a PNMT into four main parts of interest as follows (see Figure 2.1):

1. Discharge source: Contains the initial conditions such as momentum, concentration of suspended sediments and the distance to the sea bed z. The physical parameters depend on the design of the PNMT (e.g., methods of collection and separation);

2. Jet or plume regime: In this region, depending on the flow discharge parameters, the flow can be jet or plume. Later, when the buoyancy force is dominant the flow becomes a plume (see Subsection 2.2.2 and Subsection 2.4.2);

3. Impingement region: This region is located on the sea bed. Here, the negative buoyant plume changes its direction due to the direct interaction with the seabed. Sediment deposition and possible sea bed erosion are expected to take place within this region;

4. Turbidity current: This current is formed beyond the impingement region.

In the literature, classifying of sediment plumes is often related to length and time scales. Accordingly, terms like near-field or far-field regions are defined as follows: (see Figure 2.2 and 2.3):

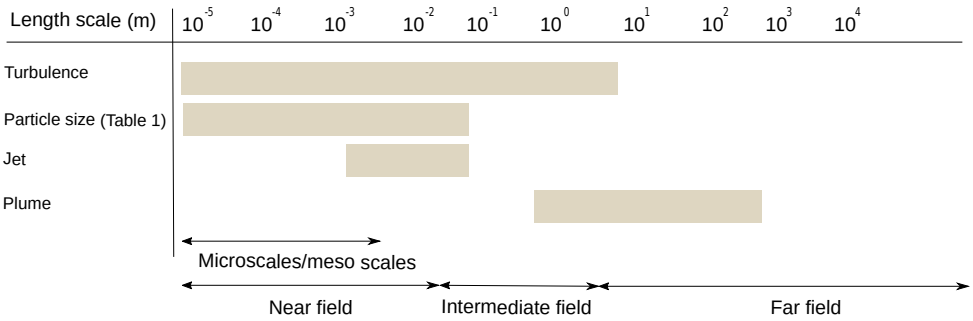

Figure 2.2: An overview of the most relevant length scales accompanying DSM activities based on the work of (Fernando, 2012).

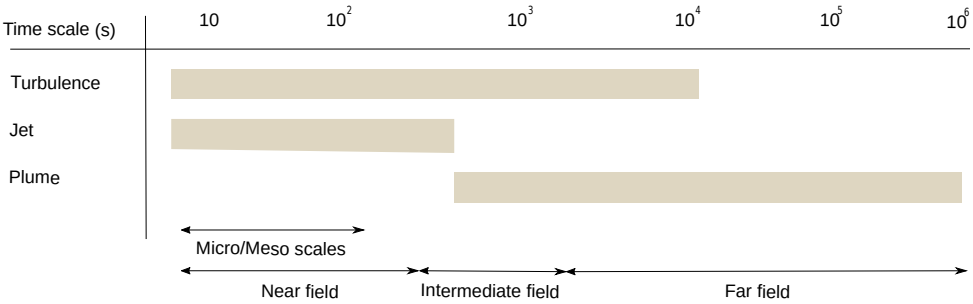

Figure 2.3: An overview of the most relevant time scales accompanying DSM activities based on the work of (Fernando, 2012).

- Near-field region: defined as the region close to the discharge apparatus and it is mostly controlled by the discharge conditions. The flows in this region have a typical length scale up to few hundreds of meters and a time scale in the range of seconds to minutes;
- Far-field region: defined as the region where the plume trajectory is dominated by the environmental parameters, such as currents and seabed topology. The flows in this region have large time and length scales, which are typically in the range of days and kilometers, respectively.

2.2.2 Physical Parameters

The discharge properties can be divided into three main groups as follows (H. Chen, 1991):

1. Mixture properties;
2. Ambient conditions;
3. Geometrical conditions.

Concerning mixture properties, the sediment-water discharge parameters (momentum, buoyancy and volume) control the flow regime at the discharge source. The sediment plume dispersion is highly dependent on the ambient conditions, such as turbulence level and background stratification that are of high importance for quantifying the plume dispersion within the near/far-field regions. The discharge geometry and its orientation are two of the key aspects that need to be well considered during the design process of a PNMT.

The discharge source is defined as the release point of the sediment-water mixture at the back of a PNMT. The source condition is characterized by momentum flux M_o, buoyancy flux B_o, volume flux Q_o and reduced gravity g'_o of a mixture. These parameters are determined as follows:

$$Q_o = A * u_o, \tag{2.1}$$
$$M_o(non - Boussinesq) = \rho * Q_o * u_o, \tag{2.2}$$
$$M_o(Boussinesq) = Q_o * u_o, \tag{2.3}$$
$$g'_o = g * \Delta\rho/\rho_o, \tag{2.4}$$
$$B_o = Q_o * g'_o, \tag{2.5}$$

where A is the cross-sectional area of the discharge geometry, $\Delta\rho = \rho - \rho_o$ where ρ_o is the ambient density, ρ is the discharge density and u_o is the discharge velocity. Boussinesq neglect density difference while non-Boussinesq approach assumes a difference in density between the discharged and ambient flows.

The turbulence level is indicated by Reynolds number (Re). Furthermore, the ratio between the inertial force and the gravitational force represents the densimetric Froude number (Fr), which classifies the discharged flow into different flow regimes ($Fr = 1$, critical flow, $Fr > 1$, supercritical flow, $Fr < 1$, subcritical flow). The mixing process of a buoyant jet can be classified based on Richardson number (Ri); if $Ri > 1$, the flow is dominated by buoyancy,

whereas if $Ri < 1$, the flow is dominated by momentum (de Wit, van Rhee, et al., 2014).

$$Re = \frac{\rho u_o L}{\mu}, \tag{2.6}$$

$$Fr = \frac{u_o}{\sqrt{gL\Delta\rho/\rho_o}}, \tag{2.7}$$

$$Ri = \frac{g\Delta\rho/\rho_o L}{u_o^2}, \tag{2.8}$$

where μ is the dynamic viscosity and L is the characteristic length, which is calculated based on the discharge geometry in the discharge origin (see Figure 2.1). A design framework characterizing the discharge process of the sediment-water mixture generated by PNMT is needed to analyse the sediment plume dispersion and the characteristics of the formed deposition layer. Beside the discharge defining, the nodule pick-up and separation processes have a great importance in controlling the initial conditions of the sediment-water discharge parameters (see Equations 2.1 - 2.5). These processes are highly affect the mixture discharge, i.e. increased erosion of the sea bed leads to high flux of sediments at the discharge source.

2.3 Flow Specification

Different flow regimes (e.g. jet, plume and turbidity current) are expected in the near-field area and these depend on the discharge parameters described in the previous section. These flow regimes occur within certain length and time scales. We here present the expected length and time scales for the underlying physical processes associated with a polymetallic nodules mining process. Moreover, we provide an overview of the physics governing sediment particle suspensions and a brief review of sediment-laden jets and plumes.

2.3.1 Length and Time Scales

The characteristic length and time scales in DSM applications vary over a wide range of magnitudes. Figures 2.2 and Figure 2.3 represent the expected

length and time scales associated with a polymetallic nodules mining process. For a dimensional analysis, the most important length scales of a discharge process are the momentum length scale L_m and the buoyancy length scale L_b (H. Chen, 1991; J. H. Lee et al., 2003), where L_m is defined as the distance where the momentum of the discharge is dominant, i.e. jet-like, and L_b is defined as the distance where buoyancy is dominant i.e. plume-like (Fischer et al., 1979). In other words, L_b represents the distance at which the flow velocity decreases to the ambient velocity (H. Chen, 1991). Regarding jet flow, there is an established jet core near the discharge source, which is not affected by the ambient entrainment. Therefore, J. H. Lee et al. (2003) divided the jet region into 2 zones: zone of flow establishment (ZFE) and zone of established flow (ZEF) (see Figure 2.4). A Lagrangian model was presented by J. H. Lee et al. (2003) for a buoyant jet, which can predict the ZEF and ZFE. Far from the discharge source, buoyancy forces dominate the flow. Mining operations affect the mined areas, however, the turbidity current resulting from the discharge process might also affect the region besides the mined area, as it could potentially travel for a long distance. Recently, using industrial scale particle transport model, Gillard et al. (2019) estimated this distance to be in the range of 4 to 9 km.

2.3.2 Particle-laden Plumes

Particle Physics

Different ranges of particle size are encountered in DSM projects. This section outlines the main physics of a moving particle in a flow and the hindered settling concept.

A single spherical particle settling in a quiescent and an infinite domain is governed by five forces: the drag F_d, gravitational F_g, buoyancy F_b, added mass F_a and history F_h forces (J. Goeree, 2018; Prosperetti & Tryggvason, 2009) (see Figure 2.5).

The added mass force and history force can be omitted in the scope of this work, because these forces are considered unsteady terms and less significant compared to the other forces. Hence, the particle motion equation can be

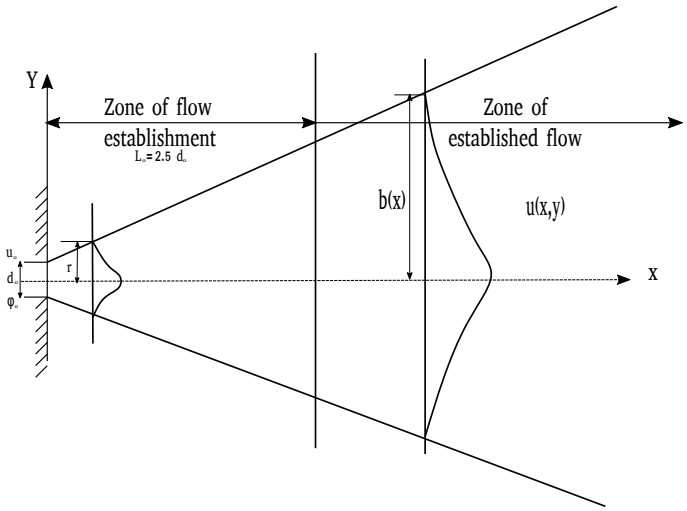

Figure 2.4: Schematic diagram of a turbulent jet generated from slot. ZFE and ZEF regions are shown along the jet trajectory (J. H. Lee et al., 2003).

expressed as follows (J. Goeree, 2018):

$$m_p \frac{d\mathbf{u_k}}{dt} = m_k g + \rho_0 v_k g - \frac{1}{2} C_d A_p \rho_0 |\mathbf{u_l} - \mathbf{u_k}|(\mathbf{u_l} - \mathbf{u_k}), \tag{2.9}$$

where A_p, v_k are the projected area of the particle and the particle size respectively, C_d is the drag coefficient, $\mathbf{u_k}$ is the velocity of the particle, $\mathbf{u_l}$ is the carrier fluid velocity, ρ_0 is the carrier fluid density, m_k is the particle mass and g is the gravitational acceleration. The drag coefficient has many formulas in the literature depending on the particle shape and roughness. These formulas were collected and classified according to the particle Reynolds number Re_k (Clift et al., 1979). The particle Reynolds number is the ratio between the particle inertial and viscous forces, moreover it is a key parameter in determining particle motion. It is worth mentioning that these formulas were derived for spherical particles. The shape of the particle has a strong influence on the motion of the particle. A general expression for the settling velocity was derived by Ferguson and Church (2004) as follows:

$$u_{kr} = \frac{R d_k^2}{b_1 \mu_f + (0.75 b_2 R g d_k^3)^{1/2}}, \tag{2.10}$$

where μ_f is the kinematic viscosity, $R = (\rho_k - \rho_l)/\rho_k$, ρ_k is the particle density,

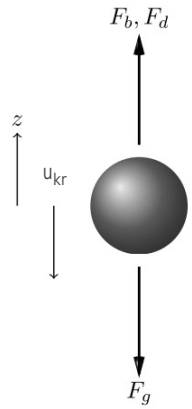

Figure 2.5: Forces acting on a non rotating settling particle in a quiescent flow, where F_g is the gravitational force, F_b is the buoyancy force, F_d is the drag force and u_{kr} is the settling velocity (J. Goeree, 2018).

ρ_l is the carrier fluid density, b_1 is reported according to particle shape and lies between the value of $(18 < b_1 < 24)$ and b_2 is the drag coefficient, $b_2 = 0.4$ for spherical particles and $1 < b_2 < 1.2$ for non-spherical particles.

Stokes number (St) represents the ratio between the particle response time τ_p (the time taken by a particle to adapt to the fluid motion) and the hydrodynamic time scale τ_h ($\tau_h = L/u$ where L is the typical length scale and u is the flow velocity at this length scale).

$$St = \frac{\tau_k}{\tau_h} = \frac{\tau_p \mathbf{u_k}}{L}. \tag{2.11}$$

In case of small particles, $St << 1$, the particle is guided by the flow motion, whilst for big particles, $St >> 1$, the flow does not affect the particle motion (J. Goeree, 2018).

Hindered settling represents the reduction of the settling velocity due to the interaction of the particle with the neighboring particles (i.e. collisions, displaced water, group settling). Based on a sedimentation and fluidization experiments, Richardson and Zaki (1954) calculated the hindered settling velocity for individual particle suspended within a mixture as follow:

Table 2.2: Fraction distribution of sediment in the CCFZ (GSR, 2018; Zawadzki et al., 2020).

Name of Sediment Fraction	**Diameter Limits (Micro) WRB Classification**	**GSR Data Average** (%)	**NTNU Data BC062 (%)**	**NTNU Data BC064 (%)**	**IOM Data Average (%)**
Clay	<2	12	11.3	14.5	23.24
Silt	2–63	76.2	85.7	82.5	70.36
Sand	63–2000	11.8	3	3	6.13

Table 2.3: Percentages of mineral groups in clay in the CCFZ (Bischoff et al., 1979; Maciąg & Harff, 2020; Zawadzki et al., 2020).

	IOM 1	**IOM 2**	**IOM 3**	**Site A**	**Site B**	**Site C**	**GSR**	**IOM**
Smectite (%)	12.71	17.33	16.49	52	38	40	36.41	16.3
Illite (%)	13.82	12.05	14.25	31	42	50	48.34	13.2
Kaolinite (%)	0.65	0.43	0.54				10.33	1
Chlorite (%)	1.7	1.85	2.35				4.92	1.5
Amorphic (%)	50.47	47.09	44.42					

$$u_{kr}(\alpha_t) = V_m(\alpha_t) u_{kr}, \tag{2.12}$$

where $V_m(\alpha_t)$ is the hindered settling function depending on Re_k and $u_{kr}(\alpha_t)$ is the hindered settling velocity which is related to the volumetric mixture concentration α_t. According to Richardson and Zaki (1954), the hindered settling function considers particle Reynolds number and the concentration value as follows:

$$\begin{aligned} V_m(\alpha_t) &= (1-\alpha_t)^n \quad \text{if} \quad \alpha_t < \alpha_{t,max}, \\ V_m(\alpha_t) &= 0 \quad \text{if} \quad \alpha_t = \alpha_{t,max}, \end{aligned} \tag{2.13}$$

where n is called Richardson and Zaki index and it depends on the Reynolds number of the particles.

$$n = \begin{cases} 4.65 \quad \text{if} \quad Re_k < 0.2 \\ 4.35 Re_k^{-0.03} \quad \text{if} \quad 0.2 < Re_k < 1 \\ 4.45 Re_k^{-0.1} \quad \text{if} \quad 1 < Re_k < 500 \\ 2.39 \quad \text{if} \quad 500 < Re_k \end{cases} \tag{2.14}$$

Polymetallic nodules are abundantly available in the Clarion Clipperton Fracture Zone (CCFZ) region, which is located in the Pacific Ocean (Oebius et al., 2001). Sediment in CCFZ consists of several fractions such as biogenicooze, terrigenous or pelagic clay, volcano debris, hydrogenous material and metalliferous sediment.

The blue Nodules project is a horizon 2020 project (EU research and Innovation program), which ran between February 2016 and July 2020. The project aimed to develop and test a novel PNMT in CCFZ region. Within the scope of Blue Nodules project, NTNU (Norwegian University of Science and Technology), a partner in the project, analysed the obtained CCFZ sediment samples. The sediment compositions for different sites in CCFZ are compared in Table 2.2 and Table 2.3, where BC064 and BC062 are two box core samples obtained from GSR (Global Sea Mineral Resources) contract area. IOM (Interoceanmetal Joint Organization) data is collected from IOM license area, which is located in the eastern part of the CCFZ (GSR, 2018; Zawadzki et al., 2020). For further details on CCFZ sediment composition, the reader is referred to the Blue Nodules project public reports, GSR public reports (G. S. M. R. GSR, 2018; Maciąg & Harff, 2020; Zawadzki et al., 2020).

Sediment Laden Jets and Plumes

A fundamental understanding of the physical parameters of discharge e.g. velocity, concentration, turbulence is needed to investigate the effect of the PNMT discharge on the sea environment. Increasing particle deposition rate and reducing plume dispersion rate would minimize the environmental impact.

Bleninger et al. (2002) and Neves et al. (2002) carried out small-scale experiments on horizontal jet discharges to measure the particles deposition. A large scatter in the deposition rate measurements was noted due to difficulties in ensuring constant concentration discharge and steady-state flow rate during the discharge process. Lab experiments were conducted to study the sedimentation from horizontal and inclined buoyant jets in a stationary environment (Lane-Serff & Moran, 2005). They introduced an integral model to determine the deposition behavior from an inclined, turbulent, buoyant jet. A dimensionless fall speed parameter, i.e. is defined as the ratio between the settling velocity and the entrainment velocity, was incorporated into the model to measure the dependency of the source velocity on the deposition near

the discharge source. The model was validated with laboratory experiments where deposition behavior, plume shape and sedimentation near the source were assessed. The earlier experiments on sediment-laden jets and plumes had the potential pitfall of not sustaining the steadiness of concentration and uniform shape at the jet exit (W. Lee et al., 2013).

A theoretical Lagrangian model horizontal jets discharged in a stationary environment was presented by (W. Lee et al., 2013). They investigated the deposition mechanisms of a horizontal particle-laden jet in terms of longitudinal distance and spreading angle. Their Lagrangian model was used by (Terfous et al., 2016) to validate the experimental work of (Cuthbertson et al., 2008; Lane-Serff & Moran, 2005; W. Lee et al., 2013). This model is adopted in Chapter 3.

The impingement region (Figure 2.1) entails a complex behavior of the flow due to the interaction between the discharged mixture and the ocean bed. At this region, the flow makes a turn and converts from a plume to a wall-bounded flow (i.e. turbidity current (Hage et al., 2019), due to the presence of the ocean bed. This current propagates downstream of the ambient flow and interacts with the bed.

2.3.3 Turbidity Current

Turbidity currents can be described as particle-laden underflows, which are driven by the excess hydrostatic pressure resulting from the density difference between the ambient water and the sediment-water mixture (Kneller & Buckee, 2000; Parsons et al., 2001). Within this current, turbulence is developed due to the continuous motion of the current over the bed and the generated shear stresses as a result of the mixing process with the ambient water at the upper boundary of the current.

Turbidity currents can be triggered by several phenomena, such as internal waves or tides (Normandeau et al., 2014), river plumes (Parsons et al., 2001) and breaching flows slides (Alhaddad et al., 2020). Mining process by a PNMT is also expected to trigger a turbidity current at the impingement region by the sediment-water discharge. Here, we refer to this current as a mining-generated turbidity current. The interaction between the discharge and

the seabed determines the behaviour of the generated turbidity current; the hydraulic properties prior to the impingement region are the main information to characterise the generated turbidity current.

Turbidity currents can occur in turbulent and laminar regimes. The flow regime is classified with Reynolds number (flow thickness is the characteristic length scale), where $Re < 1000$ is laminar, above that, the flow is turbulent. The deposition and re-suspension of sediment is highly affected by the turbulence structure (Kneller & Buckee, 2000). Turbidity currents are divided into three parts: head, body and tail (see Figure 2.6). From the perspective of hydraulics, the head has different properties than the region behind it (body and tail) (Keulegan, 1958; Middleton, 1993). The mass and momentum at the head differ significantly from the body and tail, as the head displaces the ambient fluid. Hence, the head is the densest part, as it experiences a friction resistance. Furthermore, the head is considered a 'locus of erosion' (Allen, 1971; Middleton, 1966), impacting the deposition and bed morphology. The head forms a nose starting at the lower region due to the no-slip boundary condition at the bed and the friction resistance at the upper region (Allen, 1971). At the back of the head, vortices start to take place due to the effect of the velocity shear and turbulence in the ambient fluid. These vortices define the dynamics of the head and can be identified as Kelvin-Helmholtz instabilities (Simpson & Britter, 1980). As a result of these instabilities, the back of the head forms a sharp discontinuity in the thickness of the current. However, the average velocity of the body region has to be larger than the forward velocity of the head to achieve constant rate of advance. (Middleton, 1993). The entrainment of the ambient fluid into the turbidity current and the change in the amount of suspended solids, due to net erosion or net deposition at the bed, depend on the characteristics of the current and these also lead to changes in velocity, concentration and particle size over time. Based on velocity and concentration profiles, it is possible to derive characterizing layer averaged parameters of a turbidity current. Parker et al. (1987) derived a set of equations to estimate the layer-averaged characteristics for a turbidity

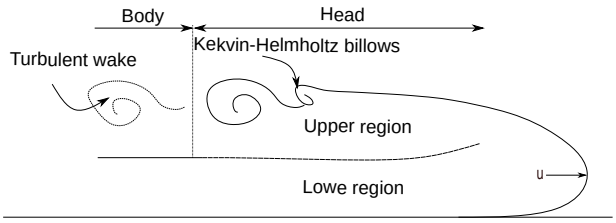

Figure 2.6: The structure of the head of a turbidity current (Middleton, 1993).

current as follows:

$$Uh = \int_0^{z_\infty} u \; dz, \tag{2.15}$$

$$U^2 h = \int_0^{z_\infty} u^2 \; dz, \tag{2.16}$$

$$UhC = \int_0^{z_\infty} cu \; dz, \tag{2.17}$$

where the $U[m/s]$ is the layer-averaged velocity, h $[m]$ the height of the current, $C[-]$ is the layer-averaged concentration, $z[m]$ is the upward normal coordinate, $c[-]$ is the local concentration and $u[m/s]$ is the local velocity and z is the vertical coordinate.

Many mathematical models are available to describe the phenomenon of turbidity current. These models can be divided into two main categories (Middleton, 1993). The first category is based on the vertical averaging technique, which describes the velocity and concentration with a single point (layer-averaged magnitude) along the traveling distance of the current. The characterization of the structure of each model depends on the assumptions made for conservation of these flow parameters. Conservation of momentum as one equation model was used in the work of Kirwan et al. (1986), while Johnson (1962) has involved four equations, i.e. conservation of mass, momentum, sediment mass, energy equations to derive his model.

The second category drives the whole velocity and concentration profiles from a turbulence model. The equations of the total kinetic energy k and its dissipation ϵ have been used as a turbulence closure. Spatial averaging (Large eddy simulation) can also be used as a closure for the turbulence (Alhaddad et al., 2020; Henniger & Kleiser, 2011; Ooi et al., 2007; Zedler & Street, 2001).

2.4 Flow Physics

The literature reports many physical approaches that characterize the flow physics in the near-field region. Here, we describe the most important physics governing the discharged flow in the near-field region. We also summarize the differences between the Gaussian and top-hat approaches, which were used in previous studies of plume integral models. Moreover, we outline the flux balance approach, the entrainment theory and the turbidity current.

2.4.1 Gaussian and Top-hat Profiles

Many researchers (Delichatsios, 1979; Middleton, 1966; Morton et al., 1956; Morton, 1959; Turner, 1962; Yu, 1990) used integral models to describe the physics of plumes. Gaussian and top-hat profiles are the main assumptions for these models. The study of Davidson (1986) extensively compares the governing equations of plumes using Gaussian and top-hat assumptions. Top-hat profile uses a constant velocity and concentration distribution over the entire plume domain, where the velocity and concentration are average values of the dominant eddies (see Figure 2.7). Additionally, the large eddies within the plume are responsible for the overall transport of momentum and mass, while the small eddies have no effect. Top-hat profiles are used mostly in the Lagrangian approaches (J. H. Lee et al., 2003). On the other hand, the Gaussian profile uses a Gaussian function to describe the velocity and concentration profiles, which are more suitable for Eulerian approaches (J. H. Lee et al., 2003). Using top-hat assumption would lead to larger entrainment coefficient compared to the Gaussian profile(Hanna, 2012).

Describing the plumes spreading behavior using the top-hat profiles offers an analytical simplicity because of the simple equations that can be used directly at the source and do not need any prior treatment for the initial condition (momentum, buoyancy, volume fluxes). Gaussian and top-hat approaches are crude assumptions to describe the self-similarity of the plumes (Davidson, 1986). Furthermore, the difference between these two approaches is small in terms of the predictions of the physical parameters. Moreover, the additional physical parameters that come within the Gaussian analysis have a minor role on describing the mean plume characteristics.

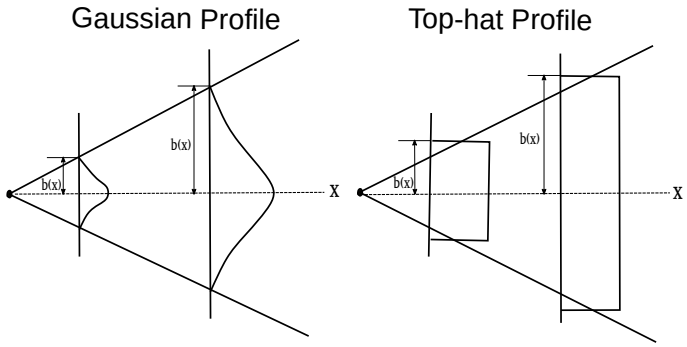

Figure 2.7: Gaussian and top hat profiles (McKernan et al., 2007), $b(x)$ is the mixing layer width.

Various cases of turbulent jets geometries e.g., slot and round shape were studied in the work of (W. Lee et al., 2013). They illustrated the governing equations that describe the jet propagation, i.e. velocity and concentration profiles along the jet width, for each of these cases. They provided an analysis for a turbulent jet from a slot in which the velocity and the concentration profiles are described in Gaussian function (2D, x-y, Cartesian coordinates).

2.4.2 Flux Balance Approach

Flux balance parameter Γ is an analytical parameter that introduces a theoretical framework of plumes (Hunt & Van den Bremer, 2011). The flux balance parameter Γ is defined as the ratio of buoyancy force to inertia force (Morton et al., 1956). The flux balance parameter can be expressed as follows (Hunt & Van den Bremer, 2011):

$$\Gamma_o = \frac{5B_oQ_0^2}{8\alpha\sqrt{\pi}M_{B,o}^{5/2}} \qquad \text{Boussinesq plumes,} \tag{2.18}$$

$$\Gamma_o = \frac{5B_oG_0^2}{8\alpha\sqrt{\pi}M_o^{5/2}} \qquad \text{non Boussinesq plumes,} \tag{2.19}$$

where Γ_o, B_o, G_o and Q_o are the initial flux balance, buoyancy, mass and volume fluxes respectively, α is the entrainment coefficient (see the entrainment

theory in the 2.4.3) and $M_{B,o}$ is the initial momentum flux under Boussinesq approximation.

Using flux balance parameter, based on the discharge conditions, it is possible to classify the discharged flow to different regime as follows:

1. $\Gamma_o = 1$ is pure plume;
2. $0 < \Gamma_o < 1$ is forced plumes;
3. $\Gamma_o > 1$ is lazy plume;
4. $\Gamma_o = 0$ is pure jet.

The plume is considered pure when its momentum and buoyancy fluxes are the same at the discharge source (Marjanovic et al., 2019). The plume is regarded as lazy when its buoyancy forces are dominant at the discharge source (Morton & Middleton, 1973), while the plume is regarded as a forced plume (also known as a buoyant jet) when its momentum forces are dominant at the discharge source (Morton, 1959). The pure jet remains a jet until it dissipates due to viscous diffusion(Marjanovic et al., 2019).

Additionally, Γ can be introduced as a square ratio between the source length L_s and jet length L_m, i.e. the momentum dominated region (Carlotti & Hunt, 2005).

$$\Gamma = (\frac{L_s}{L_m})^2, \tag{2.20}$$

where, for Boussinesq plumes;

$$L_m = \frac{\sqrt{10} M_B^{3/4}}{3\pi^{1/4}\alpha^{1/2}B^{1/2}}, \qquad L_s = \frac{5Q}{6\sqrt{\pi}\alpha M_B^{1/2}}, \tag{2.21}$$

and for non-Boussinesq plumes;

$$L_m = \frac{\sqrt{10} M^{3/4}}{3\pi^{1/4}\alpha^{1/2}B^{1/2}}, \qquad L_s = \frac{5G}{6\sqrt{\pi}\alpha M^{1/2}}. \tag{2.22}$$

2.4.3 Water Entrainment Theory

Jets an plumes are shear flows generated by buoyant and inertial sources. The interaction of jets and plumes with surroundings is known as the entrainment process. The development of a jet or a plume causes a velocity shearing that creates turbulent eddies that entrain the surrounding fluid (Marjanovic et al., 2019). The integral models of turbulent jets and plumes use the entrainment hypothesis as a closure relation for the turbulence. The entrainment hypothesis links the entrainment velocity u_e, the rate at which ambient water is entrained across the edge of turbulent plume, to the characteristic velocity of the plume by a single coefficient of proportionality, α, which is called the entrainment coefficient (Morton et al., 1956; Rooney & Linden, 1996; Turner, 1986). The entrainment velocity is calculated as follows:

$$u_e = \begin{cases} \alpha w & \text{for Boussinesq,} \\ \alpha w \sqrt{\eta} & \text{for non-Boussinesq,} \end{cases} \tag{2.23}$$

where η is the ratio of the plume density to the ambient density. The classical approach of the entrainment hypothesis is based on the macroscopic conservation of momentum, mass and volume fluxes. It has also a self-similar behaviour of the turbulence in a dimensionless form over the downstream distance from the source (Morton et al., 1956). A range of entrainment coefficients values (see Table 2.4) for different authors have been reported in the literature (Carazzo et al., 2006a). The entrainment coefficient ranges are $0.10 < \alpha < 0.16$ for plumes and $0.065 < \alpha < 0.080$ for jets (these values were calculated assuming a top-hat profile and a self-similar behaviour of the plume) (Carazzo et al., 2006a). The variations in α occur due to the different set-ups of the experiments and the resulting experimental error. The systematic differences between the reported values of α for plumes and jets suggest that α depends on the ratio between buoyancy and inertia (Γ parameter, see Subsection 2.4.2).

As mentioned above, the entrainment coefficient is the only parameter that represents the turbulence effect on the mean flow parameters. In this regard, van Reeuwijk et al. (2016) proposed to impose restrictions on the entrainment coefficient by the mean kinetic energy equation. These restrictions are referred to as the entrainment relation. This relation couples the entrainment coefficient to the physical process, such as the buoyancy effect and turbulence production, while the entrainment models are closure relations, which are obtained after all

Table 2.4: Different entrainment coefficients values reported in the literature; 'J' is the jet type flow, 'P' is the plume type flow, 'L' is liquid, 'P' is pipe and 'c' is constriction. For method, 'w' is hot wire probe and 'l' is laser Doppler anemometer; z^* is the ratio z/d in which z is the distance from the source and d is the discharge diameter (Carazzo et al., 2006b).

Source	Flow	Fluid	Nozzle	Method	Re	z^*	α
Forstall Gaylord (1955)	J	L	P	w	-	10-20	0.070
Wang Law (2002)	J	L	P	l	12700	40-80	0.075
Papanicolaou List (1988)	J	L	c	l	2460-10900	40-50	0.074
Papanicolaou List (1988)	J	L	c	l	2460-10900	50-80	0.079
Papanicolaou List (1988)	P	L	c	l	600	22-40	0.130
Papanicolaou List (1988)	P	L	c	l	600	41-53	0.126
Papanicolaou List (1988)	P	L	c	l	600	56-85	0.121
Wang Law (2002)	P	L	c	l	1550-12700	31-55	0.124

the coefficients of the entrainment relation are parameterised (Morton et al., 1956; Priestley & Ball, 1955).

The mathematical models of Morton et al. (1956) and Priestley and Ball (1955) are developed by the integration of time averaged Navier-Stokes equations across a plane perpendicular to the mean flow direction (axial cross section). The result of this integration is a system of coupled ordinary differential equations. The mathematical model of Morton et al. (1956) depends on the volume flux, momentum flux and buoyancy flux, while Priestley and Ball (1955) based their model on the momentum, buoyancy and mean kinetic energy, where the equations of Priestley and Ball (1955) rely on the turbulence kinetic energy and Reynolds stresses. A few years later, Telford (1966) presented a theory on an isolated plume in still air and a new hypothesis is formulated which the turbulence intensity directly affects the entrainment coefficient. Hence, a new equation is added to solve the turbulence kinetic energy. Utilizing the works of Morton et al. (1956) and Priestley and Ball (1955), the momentum, buoyancy, volume and kinetic energy conservation equations were combined (Fox, 1970). It was the first attempt to impose the constraints on α based on conservation of kinetic energy.

Plumes and jets are conical shapes that develop in a self-similar fashion (Hunt & Van den Bremer, 2011). Re-scaling dependent variables on the radial coordinate using characteristic scales such as w_m velocity, b_m buoyancy and r_m local width is a way to view the self similarity (van Reeuwijk et al., 2016). The effective β entrainment radius and effective density parameter

Δ for Boussinesq and non-Boussinesq flows were introduced as follow (Van den Bremer & Hunt, 2010):

$$\begin{aligned} \beta = b \quad & \& \ \Delta = 1 - \eta \quad && \text{Boussinesq}, \\ \beta = b\sqrt{\eta} \quad & \& \ \Delta = \frac{1-\eta}{\eta} \quad && \text{non-Boussinesq}. \end{aligned} \tag{2.24}$$

A self-similar solution for the plume characteristics from the governing equations in z coordinate of steady-state plumes with top-hat profile was derived as follows (Van den Bremer & Hunt, 2010):

$$\beta = \frac{6\alpha}{5} z, \tag{2.25}$$

$$w = (\frac{3}{4\pi})^{1/3} (\frac{5}{6\alpha})^{2/3} B^{1/3} z^{-1/3}, \tag{2.26}$$

$$\Delta = (\frac{B^{2/3}}{g})(\frac{4}{3\pi^2})^{1/3} (\frac{5}{6\alpha})^{4/3} B^{2/3} z^{-5/3}. \tag{2.27}$$

A method to calculate the characteristic scales, which does not rely directly on the Gaussian shape assumption but on the flow integral quantities was proposed as follows (van Reeuwijk et al., 2016) :

$$r_m = \frac{Q}{M^{1/2}} \qquad w_m = \frac{M}{Q} \qquad b_m = \frac{B}{r_m^2}, \tag{2.28}$$

M and Q are the momentum and volume fluxes respectively and B is buoyancy in integral form. (Craske et al., 2015).

$$b_m = F/Q = F/w_m r_m^2. \tag{2.29}$$

Integrating the continuity equation from the work of (Morton et al., 1956) over radial direction leads to the dilution in jets and plumes;

$$\frac{1}{r_m} \frac{dQ}{d\zeta} = -2[ru]_\infty. \tag{2.30}$$

Here, $[ru]_\infty$ is the entrainment volume flux into a plume or a jet per unit height and ζ is a dimensionless vertical coordinate equal to $\int_0^z r_m^{-1} dz'$. From the entrainment assumption ($u = \alpha u_e$) the next equation can be derived;

$$-[ru]_{\infty} = \alpha r_m w_m. \tag{2.31}$$

Substitution of 2.31 into 2.30 leads to;

$$\alpha = \frac{1}{2Q}\frac{dQ}{d\zeta}. \tag{2.32}$$

Equation 2.32 shows that the entrainment coefficient is defined as half of the increase of volume flux over a plume or jet radius r_m. This relation calculates the amount of the fluid entraining jets or plumes per unit r_m, where more entrainment leads to higher values of α (van Reeuwijk et al., 2016).

2.5 Synthesis and Outlook

This chapter was conducted to survey the state-of-the-art knowledge and physical processes of the sediment-water mixture discharged from a PNMT. This resulted in the identification of some relevant knowledge gaps.

It is expected that a wake would form behind the PNMT, while it moves forward. Further research is required to address the impact of this wake, as it might be a trigger mechanism for increasing the turbulent shear rates within the turbidity flow, thereby increasing the flocculation probability. On the other hand, the wake is turbulent and promotes water entrainment and the dilution of the discharged mixture. Properly-scaled lab experiments and validated numerical models will be beneficial to quantify this effect.

It is of great importance to study the interaction between the discharged mixture and the sediment bed, in particular at the impingement region in order to define the upstream boundary conditions of the mining-generated turbidity current. Integrated research approach combining soil and fluid mechanics is required to develop an in-depth understanding of this interaction.

Studying turbidity flows in the near-field region is a complex process. This is mainly because of the different fluid physics that are present in such activity. For example, flocculation between particles affects the critical parameters such as velocity and concentration of DSM-generated turbidity current. Therefore,

gaining insights into the whole physical behaviour of turbidity flows in the near-field region by means of numerical modelling is crucial for any PNMT design process. This will be the topic of Chapter 3.

Chapter 3

Dynamics of the Near-Field Generated Flows

Abstract

The models of W. Lee et al. (2013) and Parker et al. (1986) are combined and utilised to study the evolution of both the generated sediment plume and the subsequent turbidity current. The results show that a smaller sediment flux at the impingement point, where the plume is transformed into a turbidity current, results in a shorter run-out distance of the turbidity current, consequently being more favourable from an environmental point of view.

Parts of this chapter have been published as Elerian, M.; Alhaddad, S.; Helmons, R.; van Rhee, C. Near-Field Analysis of Turbidity Flows Generated by Polymetallic Nodule Mining Tools. Mining 2021, 1, 251–278

In this chapter, we investigate the effect of all properties of the sediment-water mixture discharged from a PNMT on the hydrodynamics of the generated plume and turbidity current. This eventually aims at selecting the optimal discharge scenarios from an environmental point of view. The model of W. Lee et al. (2013) and the four-equation model of Parker et al. (1986) are employed to study the mining-generated plume and subsequent turbidity currents. Furthermore, flocculation effect on the discharged turbidity current is discussed. Finally, key directions for future research is provided.

In our modelling approach, we consider that we have two separate, but connected regions. The first region entails the trajectory of the plume starting from the discharge source and ending at the impingement point, while the second region includes the generation and evolution of a turbidity current downstream the impingement point (see Figure 2.1). The governing equations of these two regions and the numerical results are presented in the following subsections.

3.1 Lagrangian Plume Model

The two-layer Lagrangian jet model which was developed by Lee et al. (2013) is used here to simulate the evolution of the jet/plume from the discharge source until the impingement point at the seabed. This model was validated by Terfous et al. (2019) against the experimental results of Lane-Serff and Moran (2005), Cuthbertson et al. (2008) and Lee et al. (2013), justifying our choice of this model. The Lagrangian formulation approaches a changing cross section and a coordinate system that both march in time with discrete time steps. The model follows a slice-wise approach, meaning that there is a plume slice at each time step (see Figure 3.1), which has its unique characteristics, assuming a uniform top-hat profile.

The discharge trajectory depends on water entrainment, plume bending and plume growth. The entrainment flux is calculated using Equation 3.2 and the entrainment coefficient α is calculated based on densimertic Froude number Fr using Equation 3.1 (J. H. Lee & Cheung, 1990). The initial angle of the plume $\alpha_{p,0}$ at the discharge source is 0° (with the horizontal axis) and the initial mass of the plume can be calculated using $M_{p,0} = \rho\pi b_0^2 h_0$, where a is the slice width and $b_0 = a_0 = d_0/2$ is the slice length. The time step

$\Delta t = 0.1a_0/V_0$ is calculated based on the initial velocity magnitude V_0 and initial diameter and it is consistent throughout the marching procedure. The subscripts 0, i and $i+1$ denote quantities of initial condition, previous time step and current time step, respectively. Following Terfous et al. (2019), the governing equations are expressed and solved in the following sequence:

$$\alpha_{i+1} = \sqrt{2}\frac{0.057 + 0.554 \sin \alpha_p}{Fr_i^2}, \tag{3.1}$$

$$E_{\alpha_k,i+1} = 2\pi\alpha_{i+1}V_i\rho_a b_i a_i \Delta t, \tag{3.2}$$

$$M_{i+1,p} = M_{i,p} + E_{\alpha_k,i}\Delta t, \tag{3.3}$$

$$\alpha_{t,i+1} = \frac{M_{i,p}\alpha_{t,i}}{M_{i+1,p}}, \tag{3.4}$$

$$u_{i+1} = \frac{M_{i,p}u_i}{M_{i+1,p}}, \tag{3.5}$$

$$w_{i+1} = \frac{M_{i,p}u_i + M_{i+1,p}(\frac{\Delta\rho}{\rho})_{i+1}g\Delta t}{M_{i+1,p}}, \tag{3.6}$$

$$V_{i+1} = \sqrt{u_i^2 + w_i^2}, \tag{3.7}$$

$$a_{i+1} = \frac{V_i}{V_{i+1}}a_i, \tag{3.8}$$

$$b_{i+1} = \sqrt{\frac{M_{i+1,p}}{\rho_{i+1}\pi h_{i+1}}}, \tag{3.9}$$

$$\alpha_{p,\ i+1} = \arcsin(\frac{w_{i+1}}{V_{i+1}}), \tag{3.10}$$

$$x_{i+1} = x_i + u_{i+1}\Delta t, \tag{3.11}$$

$$z_{i+1} = z_i + w_{i+1}\Delta t, \tag{3.12}$$

where u and w are the velocities in x and z coordinates, respectively, and α_t is the volumetric concentration.

3.2 Four-Equation Model for Turbidity Currents

The layer-averaged, four-equation model of Parker et al. (1986) was developed by integrating the four conservation equations of momentum, fluid mass, sediment mass and turbulent kinetic energy over the height of the turbidity

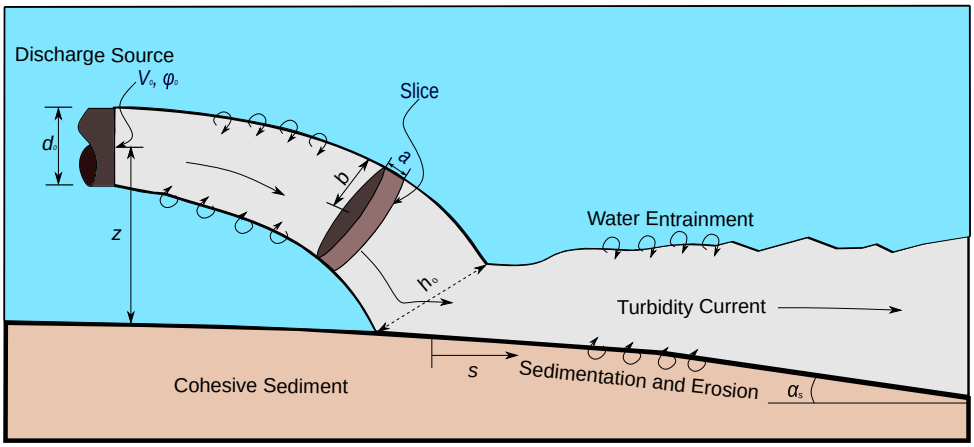

Figure 3.1: Definition sketch for the case considered including a generated plume and turbidity current.

current. The water entrainment, shear stress and sediment entrainment are included as source terms. Following Parker et al. (1986), the four equations can be expressed as follows:

$$\frac{\mathrm{d}h}{\mathrm{d}s} = \frac{-\mathrm{Ri}\,\sin\alpha_s + (2 - \frac{1}{2}\mathrm{Ri})e_w + u_*^2/U^2 + \frac{1}{2}\mathrm{Ri}\,v_{er,n}(1-n)/UC}{1 - \mathrm{Ri}}, \tag{3.13}$$

$$\frac{\mathrm{d}U}{\mathrm{d}s} = \frac{U}{h}\frac{\mathrm{Ri}\,\sin\alpha_s - (1 + \frac{1}{2}\mathrm{Ri})e_w - u_*^2/U^2 - \frac{1}{2}\mathrm{Ri}\,v_{er,n}(1-n)/UC}{1 - \mathrm{Ri}}, \tag{3.14}$$

$$\frac{\mathrm{d}(UCh)}{\mathrm{d}s} = v_{er,n}(1-n), \tag{3.15}$$

$$\frac{dK}{ds} = \frac{U^2}{h}(\frac{1}{2}e_w(1-Ri) + \frac{u_*^2}{U^2} - e_w\frac{K}{U^2} - \frac{\epsilon_o h}{U^3} - Ri\frac{w_s}{U} - \frac{1}{2}Ri\;v_{er,n}(1-n)/UC), \tag{3.16}$$

where h is the current height, α_s is the bed slope angle, Ri is Richardson number, U is the layer-averaged velocity, C is the layer-averaged concentration, K is the layer-averaged turbulent kinetic energy, ϵ_0 is the layer-averaged mean rate of turbulent energy dissipation, n is the bed porosity, e_w is the water entrianment coefficient for turbidity currents, $v_{er,n}$ is the net erosion

velocity perpendicular to the bed surface resulting from the combined effects of deposition and erosion and w_s is the hindered settling velocity. The bed shear velocity is calculated by the relation $u^* = \sqrt{\alpha_k K}$ in which α_k is a constant (0.05 to 0.5). The water entrainment coefficient e_w is calculated as follows (Parker et al., 1986):

$$e_w = \frac{0.00153}{0.0204 + \mathrm{Ri}}, \tag{3.17}$$

and ϵ_0 is calculated using the relation:

$$\epsilon_0 = \beta_0 * \frac{K^2}{h}, \tag{3.18}$$

$$\beta_0 = \frac{0.5 e_w (1 - Ri - 2C_f^*/\alpha_k) + C_f^*}{(C_f^*/\alpha_k)^{1.5}}, \tag{3.19}$$

where β_0 is a dimensionless parameter and C_f^* is a pseudo friction coefficient.

The erosion velocity for clay is calculated using the relation presented in (J. Winterwerp et al., 2012) as follows.

$$v_{er} = \frac{c_v(1-n)}{\alpha_m D_{50}} \frac{\tau_b - \tau_{cr}}{c_u}, \tag{3.20}$$

where c_v is the consolidation/swelling coefficient, α_m is a factor equal to 10, c_u is the undrained shear rate, τ_b is the bed shear stress and $\tau_{cr} = \gamma_{cr} PI^{0.2}$ is the critical shear stress and in which PI is the plasticity index and $\gamma_{cr} = 0.7$ Pa for $0.35 < \tau_{cr} < 1.4$ Pa.

To account for sediment deposition, the sedimentation velocity is calculated $v_s = (c_b u_{kr} \cos\alpha_s)/(1-n)$ in which c_b is the near-bed volumetric sediment concentration and is estimated by the relation $c_b = r_0\ C$ in which $r_0 = 1 + 31.5(u_*/u_{kr})^{-1.46}$ is a dimensionless parameter. The settling velocity for a single particle $u_{kr,o}$ is calculated based on equation 5.19 and hindered velocity u_{kr} is calculated based equation 2.12 as follows:

$$u_{kr} = u_{kr,o}(1 - C_b)^n. \tag{3.21}$$

It is to be noted that more advanced models can be used for the numerical computations of turbidity currents. Nonetheless, we use a simple model in our analysis, as our objective is to study the relationship between the initial conditions at the discharge source and the run-out distance of the mining-generated turbidity current, rather than obtaining precise results.

Table 3.1: Clay parameters used in the calculations of the erosion rate.

d_{50}	ρ_k	PI	γ_{cr}	n	c_v	c_u
0.012 mm	1350 kg/m^3	70%	0.7	0.67	8×10^{-6} m^2/s	0.2 kPa

3.3 Model Application

Figure 3.1 shows the case considered in the numerical simulations. The origin of the z coordinate is at the center of the discharge source. The stream-wise coordinate in the downstream region is denoted as s.

A typical forward velocity of a PNMT ranges between 0.25 m/s to 0.5 m/s. To reduce the environmental effect of the discharge, engineers aim to have a discharge velocity equal to the forward velocity of the PNMT. In our analysis, therefore, we consider a stationary PNMT with two discharge velocities of 0.25 m/s and 0.5 m/s and three different scenarios for the volumetric discharge concentration: 1.5%, 2% and 2.5%. The corresponding diameters of the discharge, which result in identical volumetric suspended sediment transport rate per unit width UCH, are 0.45 m, 0.34 m and 0.27 m, respectively.

At the impingement point, the flow makes a sharp turn and a turbidity current is formed, which travels downstream and interacts with the bed surface. Consequently, depending on conditions, net erosion or deposition upon the bed could take place. For simplification, we assume that we have a complete transfer of the plume characteristics to the downstream region, which has a constant bed slope angle of 3°, in agreement with the average slope found in the eastern part of the Clarion Clipperton Zone (CCZ) (GSR, 2018).

Table 3.1 summarizes the sediment properties used in the numerical computations. Most of these properties are obtained form the technical report of Global Sea Mineral Resources NV on the field experiments conducted in the eastern part of the CCZ (GSR, 2018). It is to be noted that non-Newtonian aspect is not considered in our numerical analysis, but it might be relevant for real cases.

Table 3.2: Initial conditions of the numerical runs and the numerical results; V_e, $\alpha_{t,e}$, d_e and $V_e\alpha_{t,e}d_e$ are the results at the impingement point, while U_e, C_e, h_e and $U_eC_eh_e$ are the results at 100 m downstream the impingement point.

Runs	**Initial Condition**					**Plume Model**					**Turbidity Current Model**			
	$Z[m]$	$\alpha_{t,o}[-]$	$d_o[m]$	$V_o[m/s]$	$\alpha_{t,o}d_oV_o \times 10^{-3}(m^2/s)$	$L_t[m]$	$\alpha_{t,e}[-]$	$d_e[m]$	$V_e[m/s]$	$U_oC_oh_o \times 10^{-3}(m^2/s)$	$U_e[m/s]$	$C_e[-]$	$h_e[m]$	$U_eC_eh_ex10^{-3}(m^2/s)$
1	0	0.015	0.45	0.25	1.69	-	-	-	-	1.69	0.274	0.0067	0.91	1.672
2		0.02	0.34	0.25	1.69	-	-	-	-	1.69	0.274	0.0075	0.81	1.669
3		0.025	0.27	0.25	1.69	-	-	-	-	1.69	0.274	0.0081	0.75	1.670
4	0.5	0.015	0.45	0.25	1.69	0.97	0.009	0.62	0.22	1.22	0.235	0.0051	1.00	1.206
5		0.02	0.34	0.25	1.69	0.86	0.013	0.43	0.25	1.33	0.235	0.0051	1.00	1.206
6		0.025	0.27	0.25	1.69	0.76	0.017	0.32	0.27	1.42	0.274	0.0059	0.91	1.322
7	1.5	0.015	0.45	0.25	1.69	1.62	0.006	0.72	0.24	1.05	0.254	0.0065	0.85	1.398
8		0.02	0.34	0.25	1.69	1.42	0.010	0.44	0.30	1.27	0.220	0.0038	1.26	1.050
9		0.025	0.27	0.25	1.69	1.29	0.013	0.32	0.35	1.44	0.244	0.0047	1.11	1.269
10		0.015	0.45	0.5	1.69	3.48	0.010	0.61	0.43	2.48	0.257	0.0054	1.03	1.434
11		0.02	0.34	0.5	1.69	3.05	0.013	0.43	0.47	2.67	0.323	0.0060	1.31	2.440
12		0.025	0.27	0.5	1.69	2.73	0.017	0.32	0.52	2.83	0.332	0.0060	1.31	2.605

3.4 Comparison of Results

For simplicity, we assume that the run-out distance of the turbidity current is the main criterion to assess its environmental harmfulness. Additionally, a turbidity current of a lower volumetric suspended sediment at the end of the considered numerical domain tends to die out earlier and thus has a shorter run-out distance. As this Chapter deals with the near-field flows, we analyse the results up to 100 m downstream the impingement point.

Various discharge scenarios were explored and compared as illustrated in Table 3.2. The values of U, C, h and UCh (volumetric suspended sediment transport rate per unit width) at $s = 100$ m are documented. The evolution of the plume and the turbidity current along the downstream region is shown in Figure 3.2 for a discharge source located at an elevation of $z = 1.5$ m. The cases involving a discharge velocity of 0.25 m/s and 0.5 m/s have an identical initial volumetric suspended sediment transport rate of 1.69e-3 m^2/s and 3.38e-3 m^2/s, respectively. Although the discharge has the same volumetric suspended sediment at the discharge source, the plume evolution results in different upstream boundary conditions for the turbidity current. In these cases, a discharge of a lower concentration results in a shorter run-out distance. The results also show that a higher discharge velocity results in a longer plume trajectory and a higher initial velocity for the turbidity current, which in turn leads to a longer run-out distance.

To study the effect of the elevation of the discharge source on the hydrodynamics of the turbidity current, additional two runs were conducted; a run with a discharge duct located directly on the sea bed and a run with a discharge source located at an elevation of $z = 0.5$ m (see Table 3.2). It is found that a smaller elevation results in a less diluted, less energetic turbidity current and thus a shorter run-out distance.

The numerical results show that the overall behavior of the turbidity current does not vary between the considered cases; the layer thickness increases downstream, the layer-averaged concentration decreases downstream, and the turbidity current initially decelerates until it reaches a constant layer-averaged velocity.

Overall comparison of the numerical results shows that the volumetric suspended sediment of the plume at the impingement point is crucial for

the environmental impact of the turbidity current. In other words, a lower volumetric suspended sediment at the impingement point leads to a shorter run-out distance of the turbidity current, being less harmful.

3.5 Flocculation

3.5.1 Background

Ocean bed is mainly composed of cohesive sediments (or "mud"), which consist of granular, organic, mineral solids in a liquid phase. The solids are clay, sand and silt and the liquid phase is water (J. C. Winterwerp & Van Kesteren, 2004). Due to the sticking properties of the cohesive sediment, which result from the presence of clay and organic materials, the particles may undergo break-up and aggregation processes; the latter is known as flocculation. This process occurs on the micro-scale level between sediment particles and causes them to aggregate into larger flocs. Flocculation occurs through three mechanisms;

1. Brownian motion, i.e. the random movement of the particles;
2. Differential settling, i.e. the particles with the high settling velocities collide with the particles with low settling velocities and aggregate together;
3. Turbulence mixing;

The turbulent mixing and concentration values within the turbidity flows are the main factors governing the flocculation process which they are responsible for the cohesive particles to come into contact resulting large flocs (J. C. Winterwerp & Van Kesteren, 2004). The shape factor of the flocs is expected to play a major role in determining the settling velocities as flocs tend to form irregular shapes (Gillard et al., 2019).

To understand the flocculation process in dredging operations, (Smith & Friedrichs, 2011) conducted a field experiment to quantify the flocs density and their volumetric fractions. A special attention was paid to the suspended flocs in order to study bed consolidation during the dredging process. It was found that the flocs of densities $\rho_{bed\ flocs} < 1200\ kg/m^3$ represent 0.5 to 0.8 of

the suspended mass, while the flocs (1200 $kg/m^3 > \rho_{bed\ flocs} > 1800\ kg/m^3$) represent 0.2 to 0.5 of the total suspended mass. Based on these results, they concluded that the settling velocity and floc sizes increase gradually with time, and high concentration value of the suspended sediments were found to be favorable for floc formation.

For polymetallic nodules mining applications, Gillard et al. (2019) conducted a series of experiments with different flow conditions e.g. shear rate, concentration to study the flocculation process between sediment particles. They performed the experiments with CCFZ sediment, with different concentrations (105, 175, 500 mgL^{-1}) and different shear rates (2.4, 5.7, 10.4 $s^{-}1$). They found that concentration of 500 mgL^{-1} and shear rate of 2.4 $s^{-}1$ leads to a high flocculation efficiency, inducing high settling flux. Furthermore, they calculated the settling velocities of the particle sizes 70 to 1357 μm (floc), which were in the range of 7 to 355 md^{-1}. Based on these results, they concluded that the particles would deposit rapidly with the typical deep-sea flow conditions. In addition, in the near-field region, a portion of sediments settles, creating the so-called "blanketing", which is defined as a thin layer of deposited sediments over the ocean bed. Using the experimental observations, Gillard et al. (2019) estimated that the blanketing effect would reach 9 km far away from the mining site.

Laboratory experiments were conducted to test the flocculation effect on the settling velocity of the particles and crust debris using in situ samples from sea water obtained near a seamount surface with concentrations of 20 and 100 mg/L (Spearman et al., 2020). It was found that flocculation takes place in both crust debris and sediment particles. Nonetheless, the measurements showed that the debris (1700 kg/m^3) has a lower density than the sediment (2600 kg/m^3). Moreover, the mean settling velocities were reported as 11 mm/s and 9 mm/s for the sediment and the debris, respectively. It is noticed that the mean settling velocities obtained by Gillard et al. (2019) were lower than Spearman et al. (2020) due to the existence of extra-cellular polymers and bacteria in the real sea water and the electrostatic properties of the crust particles.

The above mentioned observations indicate that the flocculation could be a key phenomenon in enhancing the particles settling and reducing the plume concentration. The sediment concentration and turbulence levels are much higher in the near-field region compared to the far-field region. As a result,

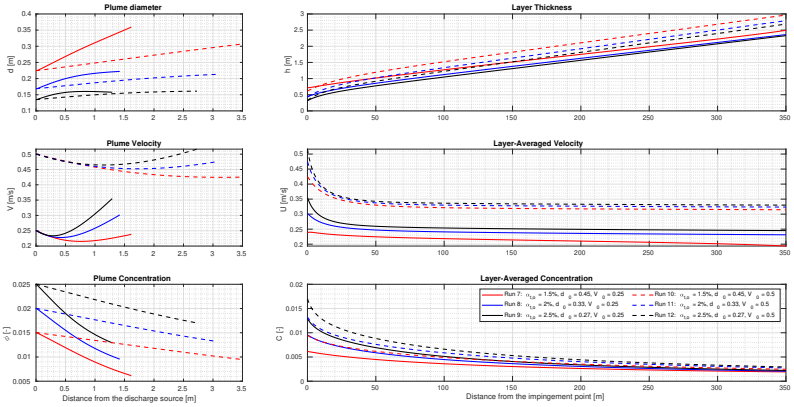

Figure 3.2: Comparison of the numerical results using different initial momentum fluxes; spatial evolution of a plume (**left**) and spatial evolution of a turbidity current (**right**).

optimizing the discharge concentration and shear rate is highly needed to enhance flocculation potential. Furthermore, an assessment of the deposited layer parameters (e.g. porosity, consolidation, structure) is required for the environmental impact assessment. It is expected that the discharged flow would experience non-Newtonian behaviour in case of high sediment concentrations. The threshold of the transition between the Newtonian and non-Newtonian behaviour of the discharged flow remains an open question.

3.5.2 Numerical Assessment of Floccluation Effect

To explore the floccluation effect on the mixture discharged from a PNMT, we utilize the numerical model of turbidity currents described in Subsection 3.2. It is to be noted that the flocculation effect on the first region of the discharge (jet/plume) is neglected here due to the short residence time of particles. We take into account the increase of the particle size and settling velocity along the run-out distance of the turbidity current as a result of flocculation. Moreover, since the residence time plays a major role in forming flocs, we extended the numerical domain to 350 m in s-direction to capture flocculation effect.

For the sake of comparison, we carried out two additional runs using the

initial conditions of Run 8 (Table 3.2): a run excluding flocculation effect, Run $8_{N.F}$, and another run including flocculation effect, Run 8_F. To the best of our knowledge, Gillard et al. (2019) is the only experimental study that investigated the flocculation effect using CCFZ sediments under shear rates comparable to those occur in polymetallic mining operations. Therefore, we adopt the measurements of Gillard et al. (2019) in our run to account for flocculation.; their observations showed that a particle size of 12 μm within 10-50 minutes and under shear rate of 2.4-10.4 s^{-1} could reach from 250 to 550 μm. Based on the results of Run $8_{N.F}$, we calculated the traveling time needed for the turbidity current to reach $s = 350$ m and it was nearly 25 minutes. Additionally, we calculated the shear rate and it was comparable to the values of Gillard et al. (2019) mentioned above. Within 25 minutes, following the measurements of Gillard et al. (2019), the suspended particle size would gradually increase from 12 μm to 550 μm. Run 8_F was performed using the same initial condition of Run $8_{N.F}$ with the difference that the particle size increase every step and the settling velocity are updated accordingly following the formula given by Gillard et al. (2019) for 10.4 s^{-1} shear rate and 500 mg/L particle concentration as follow:

$$u_{kr} = \frac{219}{1 + e^{\frac{279.1 - d_{50}}{111.3}}}. \tag{3.22}$$

The evolution of the turbidity current along the downstream for Run 8_F and Run $8_{N.F}$ is shown in Figure 3.3. The results manifestly show the floculation effect on the hydrodynamics of the turbidity current; floculation results in a slower and lower-concentrated turbidity current. This suggests that flocculation effect could be observed in the near-field region. In practice, this implies that optimizing the flow conditions (e.g. concentration and shear rate) in the near-field region to enhance the flocculation process would be effective in increasing the sedimentation rate of particles in the far-field region.

3.6 Synthesis and Outlook

The dispersion of the mining plumes could be reduced by the effect of flocculation. Shear rates and residence time of particles within a turbidity flow play a major role in triggering the flocculation process. Therefore, it is recommended

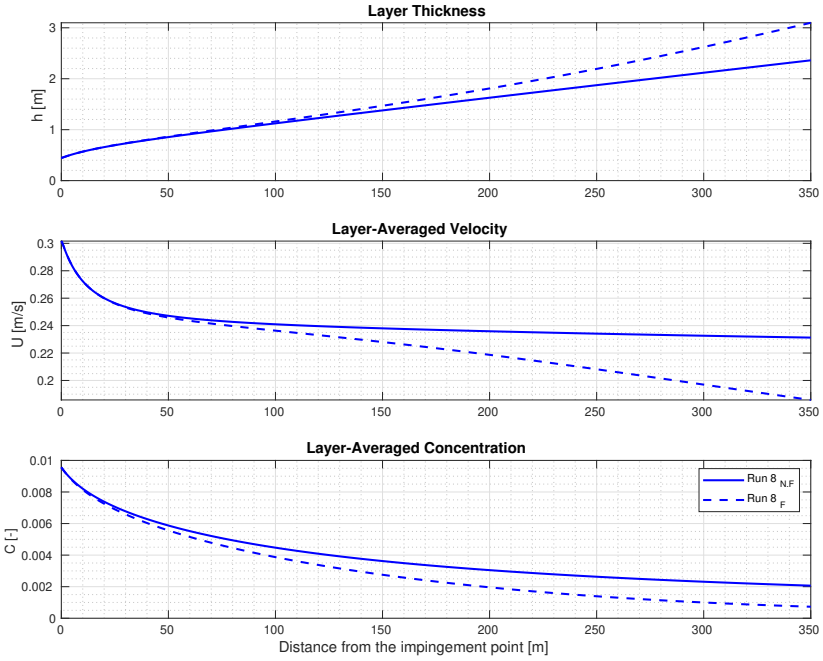

Figure 3.3: Comparison between the numerical results of a run including the flocculation effect (dashed lines) and a run excluding the flocculation effect (solid lines).

to conduct experimental research to point out possibilities to enhance the flocculation phenomenon in the near-field area.

The numerical assessment conducted within this chapter revealed that the volumetric suspended sediment of a plume at the impingement point primarily indicates the extent of the environmental hazard posed by the generated turbidity current. A smaller volumetric suspended sediment would produce a shorter run-out turbidity current. This finding can be taken into account in designing the PNMT to minimise the environmental impact of the mining process.

The results that are showed in this chapter allowed for a fundamental understanding of the general behaviour of the turbidity current parameters, i.e. velocity, thickness and concentration. Therefore, it is recommended to conduct an experimental research to point out more critical parameters such as particle

size. Additionally, an advanced, validated numerical model that can include different fractions of sediment particle would offer a complementary tool to obtain detailed results of the flow and hence develop a solid understanding to the anatomy of turbidity flows in the near-field region. Chapter4 discusses these concepts in a detailed way.

Chapter 4

DSM-Generated Turbidity Currents

Abstract

The discharge of the PNMT mixture has a significant impact on the deep-sea environment by triggering turbidity currents that alter deep-sea turbidity levels. These changes can have detrimental effects on the surrounding fauna, including changes in behavior and increased mortality rates of benthic organisms. In order to minimize the affected area and optimize discharge properties, this chapter delves into the various physical parameters that describe a generated turbidity current, such as propagation speed and concentration distribution. Additionally, we present a numerical modeling approach that can accurately predict the physical parameters of these currents in the near-field region.

This chapter has been published as Elerian, M., Van Rhee, C., Helmons, R. (2022). Experimental and numerical modelling of deep-sea-mining-generated turbidity currents. Minerals, 12(5). https://doi.org/10.3390/ min12050558 18

4.1 Introduction

Overall, gravity currents are characterized by a heavier fluid flowing underneath a lighter fluid, creating a mixing zone in between (Chowdhury & Testik, 2011). Turbidity currents are sediment-laden gravity currents, with forward motion being caused by gravity acting on the density difference between the denser water–sediment mixture and the lighter ambient fluid. Note that the concentration of the suspended sediment within the current is subject to changes throughout the propagation of the current, i.e., sediment deposition, sediment (re-)suspension (erosion) and entrainment of the ambient water.

Generally speaking, turbidity currents are challenging to investigate in the field (Georgoulas et al., 2010) because of the high cost of the field experiments, and the same applies to mining-generated turbidity currents. However, scaled laboratory experiments are an alternative and widely used option for investigating turbidity currents, with lock-exchange experiments being a particularly simple and useful experimental technique to study turbidity currents (Altinakar et al., 1990; Gladstone et al., 1998; Huppert & Simpson, 1980; Rottman & Simpson, 1983). This type of experiments involves suddenly releasing a higher density fluid into a slightly lower density fluid.

Employing lock-exchange experiments, a two-layer shallow-water model including the effect of water entrainment is developed by Adduce et al. (2012). Moreover, using an image analysis technique the propagation velocity of the current and concentration profiles are quantified by Nogueira et al. (2013a). Lock-exchange experiments are carried out by Nogueira et al. (2013b) to study the effect of bottom roughness on current hydrodynamics. Furthermore, unconfined lock-exchange experiments are also used to study the effect of the lock width on the dynamics of the current by Lombardi et al. (2018).

The effect of particle size on the propagation of turbidity currents is also discussed in literature. The effect of poorly sorted sediments (i.e., wide range of grain sizes) on the deposition behaviour of a turbidity current is investigated by Altinakar et al. (1990) and Härtel et al. (2000). Lock-exchange techniques are also utilized by Gladstone et al. (1998) to examine the effect of bi- and poly-disperse particle mixtures (silicon carbide particles with a particle density of $\rho_p = 3217$ kg/m^3) on the propagation of turbidity currents with a fixed initial volumetric concentration of 0.349% at the lock.

Mathematical and numerical models are also employed to investigate turbidity currents (Cantero et al., 2003; Elerian et al., 2021; Necker et al., 2002; Ooi et al., 2007), but with consideration of a proper validation against field or laboratory experiments. Many numerical studies have been carried out to investigate the characteristics of turbidity currents. Direct numerical simulations are performed for lock-exchange experiments to analyse the structure of the head (Necker et al., 2002). The work of Cantero et al. (2003) presents the effect of the sedimentation on the propagation of the current. Moreover, two- and three-dimensional CFD simulations are used by Ooi et al. (2007) to investigate the effect of the turbulence vortices on the breakdown of turbidity currents into different sections, i.e., body and tail. Two-dimensional Large Eddy Simulations are performed by Cantero et al. (2003) to simulate a lock-exchange experiment. Eulerian-Eulerian approach is also used to investigate the effect of particle inertia on current propagation (Henniger et al., 2008). Additionally, turbidity currents generated in lock-exchange experiments are studied by Garcia (1994) through LES simulations, comparing the results to an older DNS simulation to assess the quality of this approach.

The well-known Euler–Euler model approaches the turbidity current as separate phases of fluid and solids which are considered interpenetrating continua. From this perspective, the model consists of fluid and solid momentum equations. These equations are coupled by means of source terms (Schouten et al., 2021), which are obtained from the application of the kinetic theory. Mixture models such as the drift–flux model, on the other hand, approach turbidity currents as a single continuum. In other words, the model requires that a single momentum equation to be solved for the mixture as a whole (Drew, 1983; Ishii, 1975). Note that so-called drift velocities are a correction of the "drift" of particles relative to mixture momentum. Many researchers have worked on developing the two-phase drift–flux model, i.e., liquid and single solid phases (Drew, 1983; Ishii, 1975; Manninen et al., 1996; Van Rhee, 2002; Zuber & Findlay, 1965). Recently, a clear mathematical framework for a multiple-phase drift–flux model was presented, where each particle size represents a phase. In this respect, J. Goeree, 2018 reported a closure to the relative velocity of the different phases (see Section 4.4). The main assumptions of drift–flux model are (J. Goeree, 2018):

1. Settling velocity of particles is small compared with the bulk velocity of the mixture;

2. Particles react instantaneously to velocity changes.

The propagation of bi-disperse currents (i.e., two particle sizes are present in the mixture) is investigated by Georgoulas et al. (2010), where the lock-exchange experiments done by Gladstone et al. (1998) are simulated and validated by Georgoulas et al. (2010) using an Euler–Euler modelling approach.

Beyond the impingement region, the generated turbidity current is directed towards all directions, as shown in the top view in Figure 4.1. As mentioned before, it is challenging to investigate full-scale generated turbidity currents due to the high costs of the field experiment involved. In order to simplify the process of investigating such a complicated current, we hypothesize that the full-scale turbidity current consists of many small currents next to each other. Taking a small section from a developed mining-generated current such as section A-A in Figure 4.1, we find that a current generated in a lock-exchange experiment is representative of these small currents in terms of front velocities. In this regard, lock-exchange experiments can be a valuable tool to investigate the effect of different parameters on the propagation behaviour of the current, e.g., initial concentration and particle size. However, it is important to note that the lock-exchange generated currents are not scaled to those generated in mining contexts due to various limitations, such as the free surface area in the lock-exchange experiment and a moving discharge source. We believe that the conclusions drawn from this chapter will improve approaches to designing the discharge process.

In the present study, we use lock-exchange experiments to investigate the effect of particle size and initial concentration on the behaviour of turbidity currents. We test different initial concentrations for three sediment types with particle densities of $\rho_p = 2460$ kg/m^3 to 2650 kg/m^3 which is similar to sediment densities in abyssal plains (see Section 4.2 for the methodology of the lock-exchange experiments). Moreover, we model the turbidity current by taking multiple fractions into account. Supported by our experimental study, using minimal computational efforts, we aim to demonstrate that the drift–flux model is capable of predicting the main physical parameters (e.g., forward velocity, concentration profiles) associated with turbidity currents. The findings of this chapter contribute to defining a discharge framework for mining technology to minimize environmental impact. We present our lock-exchange experimental methodology in Section 4.2. In Section 4.3, the

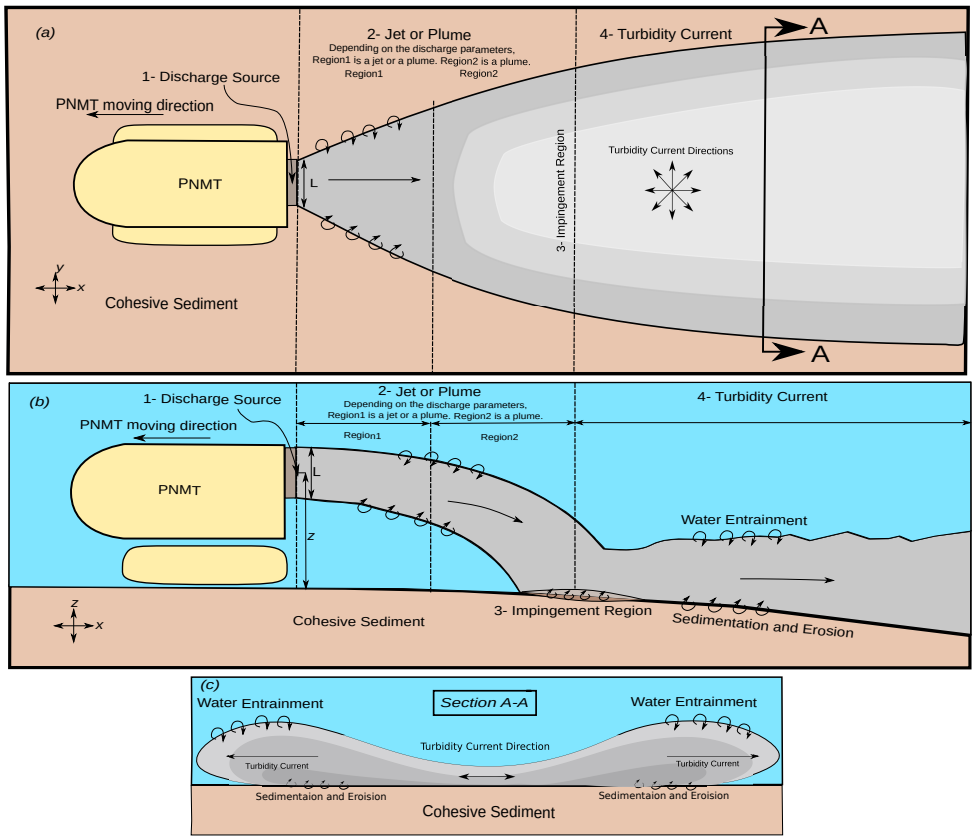

Figure 4.1: Conceptual sketch of the evolution of the sediment–water mixture discharged from a PNMT. (**a**) Top view of the discharge process from a PNMT; (**b**) right-side view of the discharge process from a PNMT (Elerian et al., 2021); (**c**) section A-A shows the direction of a turbidity current.

experimental results, such as front speed and concentration profiles, are discussed. In Section 4.4, we describe the numerical methodology based on the drift–flux modelling approach. The numerical results are compared with the laboratory experiments in Section 4.5. Finally, conclusions are drawn in Section 4.6.

4.2 Experimental Apparatus and Laboratory Experiments

4.2.1 Lock-Exchange Experiments

The lock-exchange experiments are conducted in a rectangular perspex tank with dimensions: $L = 3$ m, $W = 0.2$ m and $D = 0.4$ m. For all runs, the gate is positioned at a horizontal distance of $x_o = 0.2$ m (Figure 4.2). A background plate with white LED strips is installed at the back of the tank. A chapter sheet is fixed in front of the white LED strips to generate homogeneous diffused light (Figure 4.3). A black tent is built around the setup to create a high level of contrast between the tank and the surrounding area. A "IL5HM8512D Fastec" high-speed camera with a Navitar 17 mm lens are used to record video footage of each run (Figure 4.3). A mixer is used to mix the sediment with the fresh water in the lock (behind the gate at x_o) for 1 to 2 min before removing the gate. Three sediment types are tested. Table 6.1 shows the particle size range, sediment type and density of each type. Type1 sediment consists of round, white synthetic glass beads, Type2 is made up of fine silica sand particles (Millisil M10, irregular particle shape) and Type3 is a mixture of equal parts Type1 and Type2 (50-50 mass). The sediment types were selected to represent a range of particle sizes from coarse to fine. The D_{10}, D_{50} and D_{90} for Type1 and Type2 are reported in Table 4.2.

The tank is filled with fresh tap water to a depth of $H = 0.35$ m for each run. Based on the water volume inside the lock, the required initial concentration is determined by the mass of sediment added in the lock and mixed with the fresh water. The run starts when the gate is suddenly removed, initiating a turbidity current in the tank. The experimental run ends when the current is out of the video boundaries ($L_o = 2.4$ m, Figure 4.3). The propagation of each turbidity current is recorded with a rate of 130 frames per second, 8 bit depth (i.e., number of bits used to define the colour channels).

4.2.2 Concentration Calibration Method

The same setup (tank and the camera) is used to perform the calibration process. This process begins with filling the mixing section with fresh tap water, after which a pre-weighed mass of sediment is added and mixed. After

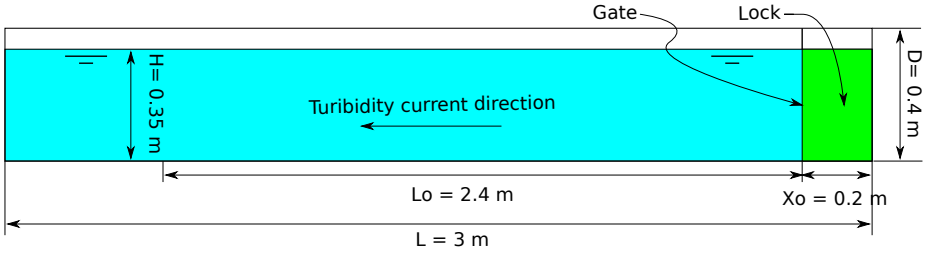

Figure 4.2: Schematic representation of the tank used in the experiments. The dimensions of the lock and the tank and the water depth are shown.

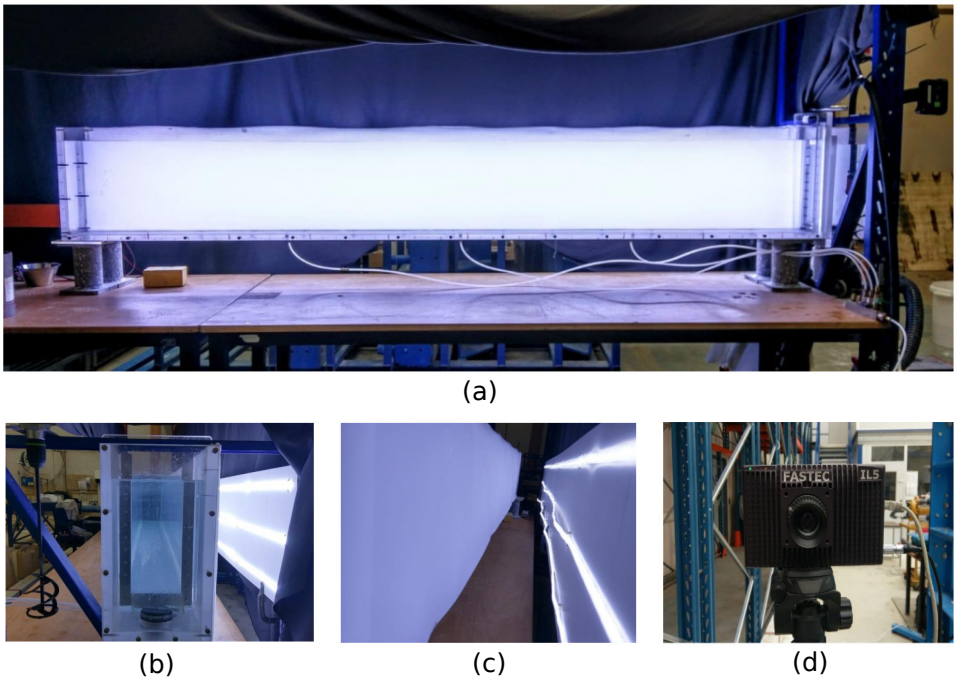

Figure 4.3: (**a**) Final setup of the tank with the diffused light. The black tent is used to create the maximum contrast; (**b**) side view of the tank setup showing wooden panel with LED stripes; (**c**) side view of the LED stripes and the diffused paper in front of it; (**d**) the high speed/definition camera used in the experiments.

Table 4.1: Main parameters of the experimental runs.

Runs	Sediment Type	Particle Size Range[μm]	Mass	Volumetric Concentration[%]	Density of Particles [kg/m^3]
1	Type 1	65-105	0.172	0.5	2460
2	Type 1	65-105	0.344	1	2460
3	Type 1	65-105	0.517	1.5	2460
4	Type 1	65-105	0.689	2	2460
5	Type 1	65-105	0.861	2.5	2460
6	Type 1	65-105	1.033	3	2460
7	Type 2	4-60	0.037	0.1	2650
8	Type 2	4-60	0.093	0.25	2650
9	Type 2	4-60	0.186	0.5	2650
10	Type 2	4-60	0.371	1	2650
11	Type 2	4-60	0.557	1.5	2650
12	Type 2	4-60	0.742	2	2650
13	Type 2	4-60	0.928	2.5	2650
14	Type 2	4-60	1.113	3	2650
15	Type 3	4-105	0.036	0.1	2460-2650
16	Type 3	4-105	0.089	0.25	2460-2650
17	Type 3	4-105	0.179	0.5	2460-2650
18	Type 3	4-105	0.358	1	2460-2650
19	Type 3	4-105	0.537	1.5	2460-2650
20	Type 3	4-105	0.715	2	2460-2650
21	Type 3	4-105	0.894	2.5	2460-2650
22	Type 3	4-105	1.073	3	2460-2650

Table 4.2: D_{10}, D_{50} and D_{90} in μm for Type1 and Type2.

	D_{10}	D_{50}	D_{90}
Type 1	59.09	88.6	132.7
Type2	1.6	17	51

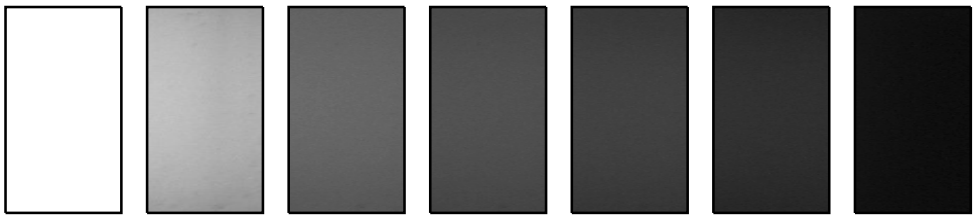

Figure 4.4: Shades of grey for Type1 sediment.

Table 4.3: Step-by-step sediment addition and sediment concentration ranges.

Sediment	**Concentration Ranges**	**Increments**
Type1	0.0–0.1%	0.01%
	0.1–0.5%	0.05%
	0.5–1.0%	0.10%
	1.0–2.0%	0.25%
Type2	0.0–0.1%	0.01%
	0.1–0.5%	0.05%
Type3	0.0–0.1%	0.01%
	0.1–0.5%	0.05%

the water and sediment have been properly mixed, a snapshot is taken of the mixing section. Subsequently, another pre-weighed portion of sediment is added to the mixture and recorded. This process of adding sediment proceeds until the resulting pixel values reach about 255 (i.e., a pixel value of 255 is the camera's limit for determining different shades of grey, with pixel values ranging from 0 for white to 255 for black, see Figure 4.4). As a result, every snapshot shows a certain level of concentration. Table 4.3 shows the concentration ranges and sediment addition steps for each sediment type. For example, Figure 4.4 shows the calibration process of Type2 sediment, with each snapshot showing a certain volumetric concentration level. The calibration process must be repeated for each sediment type due to differences in the particle reflection index.

The snapshots are identical in terms of length and width, i.e., they feature an equal number of pixels. A Gaussian blur is applied to each snapshot to average the value across the pixel range. Pixels values are not identical across snapshots due to the heterogeneous intensity of the background light. To correct this discrepancy, the pixel value of each pixel is recorded throughout

the addition process, following the fact that the pixel indices are fixed in all snapshots. Finally, the concentration-pixel matrix is determined, yielding a calibration curve for each pixel (Figure 4.5).

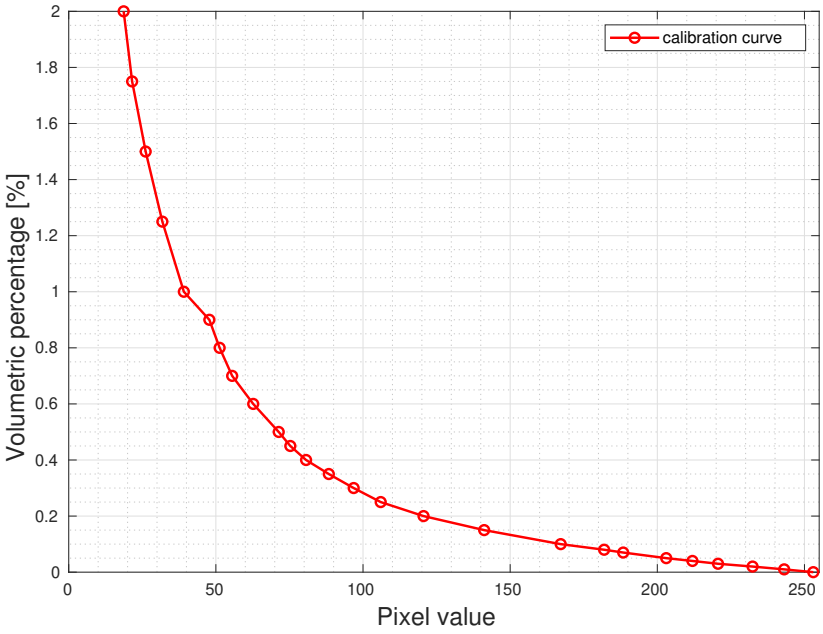

Figure 4.5: Calibration curve for one of the pixels for Type1 sediment.

4.2.3 Concentration Measurements

The concentration measurement begins with targeting a specific frame of interest. An algorithm is developed using Python to calculate the concentration. The algorithm proceeds as follows:

1. Gaussian blur is applied to the targeted frame;
2. The pixel value matrix of the clear water tank frame (the frame taken before opening the lock gate) is obtained;
3. The pixel value matrix of the targeted frame is obtained;

4. The two matrices of both frames are compared to each other pixel by pixel;

5. If a pixel value change is detected between the two frames, based on a pixel value of the clear water tank frame, the concentration–pixel value curve is called;

6. From the concentration-pixel value curve (Figure 4.5), using the pixel value of the targeted frame, the concentration of this pixel is calculated;

7. Finally, the targeted frame concentration matrix is calculated, after which the grey scale images are converted into colour maps (red, green and blue) based on concentration values (see Section 4.3.2).

4.2.4 Front Velocity Measurements

The calculation of the front velocity begins when a distinctive head is formed. An algorithm is developed in Python to calculate the front velocity using a subtraction procedure. The algorithm proceeds as follows:

1. The first frame of the recorded video (clear water tank) is obtained;

2. The subsequent frames, with a time step of 0.23 s, are subtracted from the first frame in terms of pixel values. Note that the time step represents 30 frames. This number of frames was selected in order to smoothen the distance–time curves;

3. The resulting frame from each subtraction step is converted into a binary image with a pixel value of 25 as a threshold;

4. The resulting binary image is used to track the front position over time.

4.3 Experimental Results

This section presents the experimental results and discusses front velocity and concentration maps. In this section, concentration and velocity calculations are based on a two-dimensional approach.

4.3.1 Front Velocities

One of the most commonly studied quantities in lock-exchange experiments is front speed. According to literature (Huppert & Simpson, 1980; Rottman & Simpson, 1983), based on the front speed, a turbidity current in a lock-exchange experiment exhibits three phases: slumping phase, self-similar phase and viscous-buoyancy phase. The slumping phase occurs near the lock gate, where the dense fluid near the lock starts to collapse. This phase features the formation of a turbidity current front, also known as the head of the current. In this phase, constant propagation speed is observed due to the balance between inertia and buoyancy forces. After the slumping phase, the self-similar phase commences, where the propagation speed of the current is not constant anymore and starts to decrease. Eventually, since viscous forces dominate the flow, the viscous-buoyancy phase is initiated and the current dies out.

Figure 4.6 shows the measured front positions x_n for all runs as a function of the propagation time t. Velocity instabilities can be observed near the lock gate region, especially with low initial concentrations (i.e., runs 1 and 7). These instabilities are caused by the wave generated by removing the lock gate, since the driving buoyancy force of the low-concentration current might be lower than wave forces. There is an evident positive correlation between the initial concentration and front speed, independent of sediment type. The increase in particle suspension leads to higher buoyancy forces, which provide the current with momentum.

For each sediment type, Figure 4.7 compares the time needed by the currents as a function of the concentration inside the lock to reach the end of the visualization region. Interestingly, starting from an initial concentration of 1.5% (runs 11, 19) until the end (runs 14, 22), small differences can be observed in front velocity between Type2 and Type3. For initial concentrations of 2.5% (runs 5, 13, 21) and 3% (runs 6, 14, 22), the front velocities are found to be almost the same for all sediment types. Increasing initial concentration strengthens the presence of an important mechanism that increases particles suspension during the development of the current. The resulting high-buoyancy driving forces from the presence of the particles would increase turbulence intensity (i.e., the particles' gravity forces cannot overcome the turbulence forces, causing the particles to remain suspended). It is therefore obvious that

particle size does not play a major role with high concentrations, with the proviso that this may be different for turbidity currents with long run-out distances.

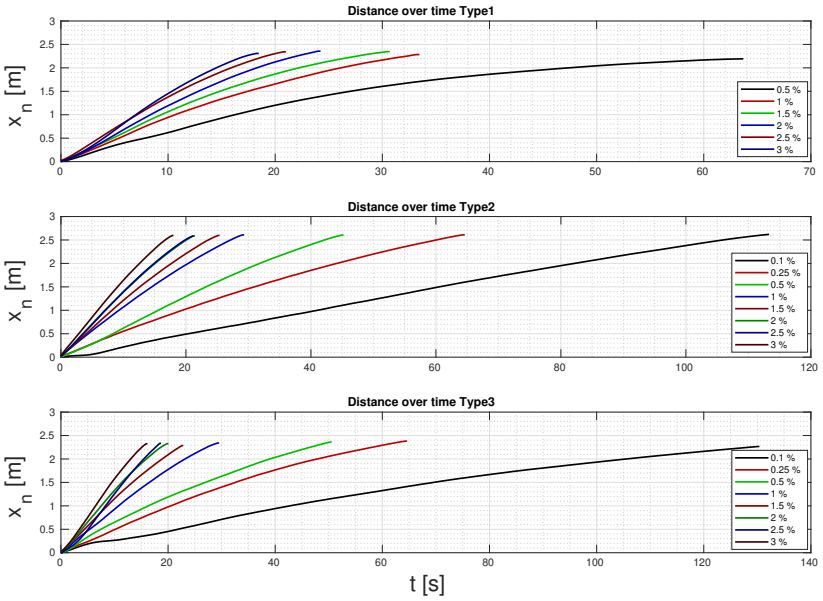

Figure 4.6: Front position of the turbidity currents x_n as a function of the propagation time t.

It is challenging to determine the different phases from Figure 4.6. The work of Rottman and Simpson (1983), studying saline gravity currents, showed that the slopes of dimensionless distance–time curves can define the different phases, with the slopes of 1, 2/3 and 1/3 of these curves defining the slumping, self-similar and viscous phases, respectively. To distinguish the different phases in our experiments, the normalized time-distance figures are plotted in Figure 4.8. The front position x_n is normalized to the lock length $x_o = 0.2$, where $X_n = x_n/x_o$ and the time is normalized in accordance with Froude number, where $T = t/(x_o/\sqrt{g'_o H})$. Reduced gravity g'_o is calculated using the following equation:

$$g'_o = \frac{g(\rho_m - \rho_c)}{\rho_c}, \tag{4.1}$$

where g is the the gravitational acceleration, ρ_c is water density and ρ_m is

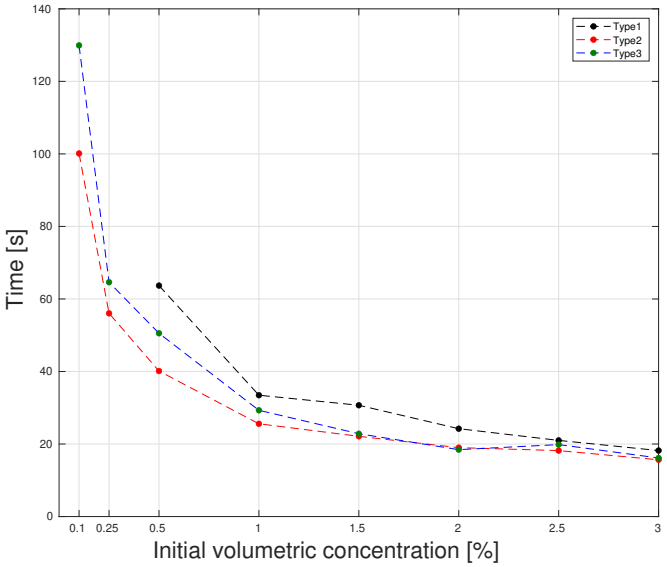

Figure 4.7: Time needed by the current to reach the end of the visualized region as a function of the initial concentrations.

initial mixture density. The curves shown in Figure 4.8 are characterized by two distinct slopes: The first slope ≈ 1 for the slumping phase and second slope $\approx 2/3$ for the self-similar phase. The 1/3 slope was not observed in any runs, implying that none of the experimental runs made it to the viscous phase. As expected, the slope values for the slumping and self-similar phases follow the findings of Rottman and Simpson (1983), since all currents exhibit the slumping phase. After the slumping phase, only run1, i.e., with the lowest initial concentration of Type1 sediment, exhibits the self-similar phase. All runs, except for run1, failed to transition to the self-similar phase. Runs 2–6 of Type1 and run 15–17 of Type3 show that front velocity starts to increase at the end of the visualized region. Nevertheless, no run exhibits a self-similar phase. Moreover, the transition time t* for run1 can be calculated from the intersection between the slopes of 1 and 2/3 of that curve; t^* is estimated to be 19.76 s.

The effect of sediment particle size can be observed by examining the dynamics of the currents, with Type2 sediment, consisting of fine particles,

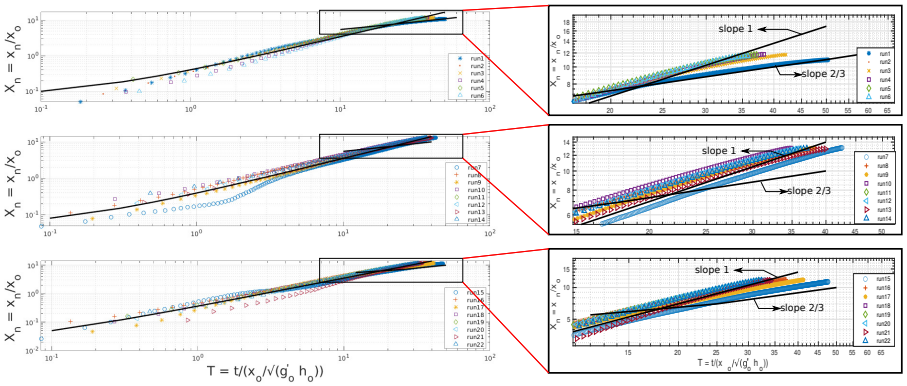

Figure 4.8: Log-Log plot of dimensionless time, T, vs. dimensionless front positions for all experimental runs. The solid lines represent the slopes 1 and 2/3 for the long and short lines, respectively. The right figure provides a more detailed look at the transition point of the current from slope 1 to slope 2/3.

revealing no decrease in front velocity. The low particle size and the irregular shapes of Type2 result in low particle settling velocities that cause no decrease in the current's front velocity. On the other hand, the effect of the coarser particles (in Type1, runs 1–4) is visible at the end of the visualized region, with the coarse particles settling and not contributing to the buoyancy driving forces of the current anymore. For this reason, the curves approach the 2/3 slope line near the end of the visualized region. With Type3, the front velocity observed in runs 15–17 decays at the end because of the deposition of the coarser particles. This can be seen from the slope of the curves, which approach the 2/3 slope. However, for remaining runs of Type3, as mentioned above, the coarser particles did not settle due to high turbulence forces resulting from high driving buoyancy forces. In other words, the curves of the remaining runs have a slope of 1 until the end of the visualization region. In essence, increasing the initial concentration delays the transition time towards the self-similar phase.

4.3.2 Concentration Distributions

With the calibration process described above, it is possible to measure the concentration of a running current at any time and location, assessing the

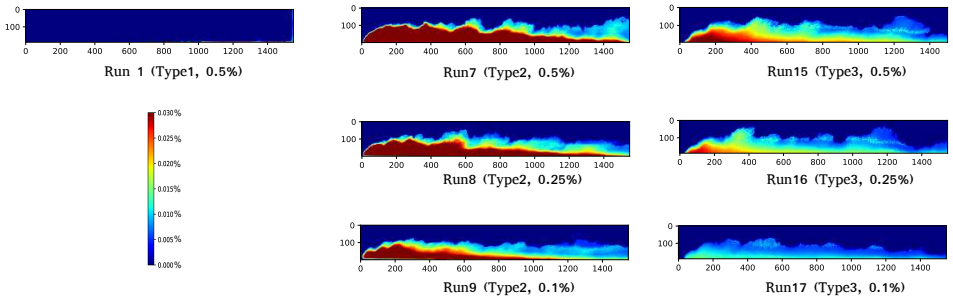

Figure 4.9: Comparison of the concentration distribution of the currents. The rows represent the same initial concentration and the columns represent the same sediment type. All the runs are acquired at the same front position.

vertical dispersion of the current. Figure 4.9 shows colour maps of different snapshots of runs 1,7–9 and 15–17 acquired at the same front position. The snapshots are taken with the front at the end of the visualized region to ensure the development of the current. The x and y-axes denote the pixel positions. In runs 15–17, currents with Type3 sediment have lower concentration distribution values than for Type2 along the whole length of the tank, due to the deposition of large particles. In these specific runs, the settling of coarse particles affects the dynamics of the current during current propagation, whereas the fine particles remain in suspension. Moreover, in run 1, most particles settle and the current is not visible anymore with the used threshold before it reaches the end of the visualized area. For runs 7–9, because of the sediment characteristics of Type2 (i.e., small particle size and irregular particles shape), the particles do not settle during the propagation period of the current. Taking everything into account, only for the runs shown in Figure 4.9.

1. Increasing initial concentration leads to higher concentration distribution values and high front speed of the current;

2. Increasing particle size reduces the concentration distribution values and the front velocity of the current.

4.4 Numerical Model Description

In this section, we present a drift–flux model that is used in turbidity current simulations. The drift–flux model is a mixture model where one momentum equation for the whole mixture is required. In this modelling approach, the particles follow the surrounding flow motion but also have a deposition behaviour. In order to justify our choice of drift–flux modeling approach, first, we have to ensure that the particles follow the flow and do not have their own trajectories. Fortunately, Stokes number (St) can be used to determine this criterion, where a particle's Stokes number is the ratio between particle response time τ_p to the flow characteristic time scale T_k of the flow:

$$St = \frac{\tau_p}{T_k} = \frac{\rho_p d_p^2/18\mu}{L/U}, \tag{4.2}$$

where ρ_p is particle concentration, d_p is particle diameter, μ is the liquid phase dynamic viscosity, L is the characteristic length scale and U is the velocity of the flow at the length scale. In our case, L and U are taken to be the thickness of the current and the front speed of the current, respectively. In case of $St << 1$, this means that the particle response time is much lower than the shortest eddy time scale, which means the particles remain within the flow eddies. If $St >> 1$, on the other hand, the particle's response time is much longer. Consequently, the particle does not follow the eddy. Coarse particles have a high Stokes number. Accordingly, following the experimental results mentioned in Section 4.3, using the diameter sizes of 60 and 105m for runs 6,14 and 22, which the highest front velocity, St is calculated to be 1.3×10^{-3}, 4.2×10^{-4} and 1.2×10^{-3}, respectively. As such, the drift–flux model is appropriate for the study in this chapter.

The main assumption of the drift–flux model is that the momentum of solid phases (i.e., each fraction represents a phase) rapidly adapts to the momentum of the liquid phase in a planar direction while continuing to move relative to the liquid phase in the gravitational direction (Burt, 2010). To put it differently, there is little or no momentum exchange between the solid and liquid phases (J. C. Goeree et al., 2016). The study in this chapter uses the mathematical multiple-fractions-drift–flux model that was recently reported by J. C. Goeree et al. (2016). Furthermore, this model is extended in OpenFOAM (an open-source CFD tool). OpenFOAM solves the governing equations sequentially using the Finite-Volume Method (FVM). Accordingly,

the equations are integrated at each computational cell, yielding discretized equations for each quantity.

4.4.1 Governing Equations

The drift–flux model is composed mainly of one mixture momentum equation, one mixture continuity equation and one phase transport equation for each particle size fraction. The mixture continuity equation is defined by the following relationship:

$$\frac{\partial \rho_m \mathbf{u_m}}{\partial t} + \nabla . \rho_m \mathbf{u_m} = 0, \tag{4.3}$$

and the mixture momentum equation can be described as follows:

$$\begin{aligned} \frac{\partial \rho_m \mathbf{u_m}}{\partial t} + \nabla . \rho_m \mathbf{u_m} \mathbf{u_m} = \nabla p_m + \nabla . ((\nu_m + \nu_t) \nabla \mathbf{u_m}) \\ - \sum_{k=1}^{n} \alpha_k \rho_k \mathbf{u_{km}} \mathbf{u_{km}} + \rho_m g + M_m, \end{aligned} \tag{4.4}$$

where the subscripts k and m denote the phase k and mixture m, p_m is the mixture pressure gradient, α_k is the volume fraction phase k, ν_m is the mixture kinematic viscosity, ν_t is the eddy viscosity, M_m is external source term, $\rho_m = \sum_{k=1}^{n} \rho_k \alpha_k$ is the mixture density, $\mathbf{u_{km}} = \mathbf{u_k} - \mathbf{u_m}$ is the relative velocity of the phase k to the mixture m, $\mathbf{u_k}$ is the phase velocity and $\mathbf{u_m}$ is the mixture velocity and is calculated as follows:

$$\mathbf{u_m} = \frac{1}{\rho_m} \sum_{k=1}^{n} \rho_k \alpha_k \mathbf{u_k}. \tag{4.5}$$

Interestingly, the third term on the right-hand side of equation 4.4,

$$\sum_{k=1}^{n} \alpha_k \rho_k \mathbf{u_{km}} \mathbf{u_{km}}, \tag{4.6}$$

is the advection term resulting from the existence of the solid particles. The phase transport equation is given as follows:

$$\frac{\partial \alpha_k}{\partial t} + \nabla . (\alpha_k \mathbf{u_k}) = \nabla . \Gamma_t \nabla \alpha_k, \tag{4.7}$$

$$\frac{\partial \alpha_k}{\partial t} + \nabla . (\alpha_k (\mathbf{u_m} + \mathbf{u_{km}})) = \nabla . \Gamma_t \nabla \alpha_k. \tag{4.8}$$

The right-hand side represents the particle turbulence diffusion. Γ_t is the turbulence diffusion coefficient, which is defined as the ratio between the eddy viscosity μ_t and turbulent Schmidt number Sc. In this chapter, Sc is taken to be 1. Note that we solve the phase transport equation only for the solid phases. To calculate the liquid phase, we use the following:

$$\sum_{k=1}^{n} \alpha_k = 1. \tag{4.9}$$

Based on that, $\alpha_c = 1 - \alpha_t$, where α_c is the volumetric concentration of the liquid phase and $\alpha_t = \sum_{k=2}^{n} \alpha_k$ is the volumetric concentration of total solid phases.

Following Equations (4.4) and (4.7), $\mathbf{u_{km}}$, ν_m, and ν_t require closure. Starting with $\mathbf{u_{km}}$, we employ the following equation using the relative velocity approach (J. C. Goeree et al., 2016):

$$\mathbf{u_{km}} = \mathbf{u_{kr}} - \sum_{k=1}^{n} c_k \mathbf{u_{kr}}, \tag{4.10}$$

where $\mathbf{u_{kr}} = \mathbf{u_k} - \mathbf{u_c}$, $\mathbf{u_{kr}}$ is the relative velocity of the phase k to the liquid phase c, which is also known as the terminal settling velocity, and c_k is the mass fraction of phase k. The terminal settling velocity u_{kr} is calculated for each solid phase using the following equation (Ferguson & Church, 2004):

$$u_{kr} = \frac{Rgd_p^2}{b_1\nu_f + (0.75b_2Rgd_p^3)^{1/2}}, \tag{4.11}$$

where ν_f is the kinematic viscosity of the liquid phase, g is the gravitational acceleration, $R = (\rho_p - \rho_a)/\rho_p$, ρ_p is the particle density, ρ_a is the liquid phase density, and b_1 and b_2 are presented in Table 4.4.

The effect of hindered settling is also taken into account, by using the Richardson and Zaki (1954) formula for hindered settling.

$$u_{kr} = V_m(\alpha_t), \tag{4.12}$$

$$V_m(\alpha_t) = (1 - \alpha_t)^{e-1} \quad \text{if} \quad \alpha_t < \alpha_{tmax}, \tag{4.13}$$

$$V_m(\alpha_t) = 0 \quad \text{if} \quad \alpha_t = \alpha_{tmax}, \tag{4.14}$$

Table 4.4: Values of b_1 and b_2 used for the three sediment types. The typical values of b_1 and b_2 are $18 < b_1 < 24$ and $1 < b_2 < 1.2$.

	Type1	**Type2**	**Type3**
b_1	18	24	22
b_2	0.4	12	1

where e is the so-called Richardson and Zaki index, which depends on a particle's Reynolds number that can be defined as the ratio between the particle inertial and viscous forces. We use the empirical equation of Rowe (1987) to calculate the value of e as follows:

$$e = \frac{a + bRe_p^d}{1 + cRe_p^d}, \tag{4.15}$$

where a, b, c, and d are experimental coefficients and are taken to be $4.7, 0.41, 0.175$ and 0.75, respectively.

The presence of the particles will influence the viscosity. Noting that the mixture is considered in the Newtonian regime, we use the formula of Thomas (1965) that describes the mixture viscosity as a function of the volume concentration of solids as follows:

$$\nu_m = \nu_f(1 + 2.5\alpha_t + 10.05\alpha_t^2 + Aexp(B\alpha_t)), \tag{4.16}$$

where A and B are empirical factors that are taken to be $= 0.00273$ and 16.6, respectively (J. C. Goeree et al., 2016).

Finally, to calculate ν_t in Equation 4.4, we use the buoyant $k - \epsilon$ model as a closure for turbulence, where k accounts for the turbulence kinetic energy and ϵ for the turbulence energy dissipation rate. The Buoyant $k - \epsilon$ model can be described by the following equations (Van Rhee, 2002):

$$\frac{\partial \rho_m k}{\partial t} + \nabla.(\rho_m k \mathbf{u_m}) = \nabla.[(\nu_m + \frac{\nu_t}{\sigma_k})\nabla k] + P_k + P_b + \rho_m \epsilon, \tag{4.17}$$

$$\frac{\partial \rho_m \epsilon}{\partial t} + \nabla.(\rho_m \epsilon \mathbf{u_m}) = \nabla.[(\nu_m + \frac{\nu_t}{\sigma_\epsilon})\nabla \epsilon] + C_{t1}\frac{\epsilon}{k}(P_k + C_{t3}P_b) - C_{t2}\rho_m \frac{\epsilon^2}{k}, \tag{4.18}$$

where $\sigma_k = 1$, $\sigma_\epsilon = 1.3$ are the turbulent Prandtl numbers, $C_{t1} = 1.44$, $C_{t2} = 1.92$, and $C_{t3} = 1$ are turbulence model constants. P_k is the generation of turbulence kinetic energy due to mean velocity gradients, and P_b is the generation of turbulence kinetic energy due to buoyancy. It is important to emphasize that, for non-stratified flows, the buoyancy term vanishes where $C_{t3} = 0$, while $C_{t3} = 1$ in the case of stable stratification. After solving the $k - \epsilon$ model, eddy viscosity ν_t can be calculated following this relation:

$$\nu_t = C_\mu \frac{k^2}{\epsilon}, \tag{4.19}$$

where $C_\mu = 0.09$ is a turbulence constant.

4.4.2 Application of the Numerical Model

Two-dimensional (2D) computational mesh representing the experimental set-up is shown in Figure 4.2. A 2D mesh is used further to reduce the computational efforts required. Figure 4.10 also shows the used Boundary Conditions (B.C); see Section 4.4.2. Two cell zones are defined, with first cell zone 1 representing clear water, i.e., $\alpha_c = 1$, $\alpha_t = 0$ and cell zone 2 representing the lock region where α_t has a value depending on the initial condition of the numerical run and $\alpha_c = 1 - \alpha_t$. The 2D mesh consists of 8000 mesh cells. Furthermore, in both zones, cell dimensions increase in the positive Z direction with a growth rate of 1.02, for the purpose of capturing the dynamics of the current near the bottom in greater detail. The cell dimensions are kept constant in the x-direction (see Figure 4.10).

Boundary Conditions

In this section, we summarize the general aspects and characteristics of the B.C used in the numerical runs presented here. Boundary conditions are specified for quantities $u_m, p_m, \alpha_k, \epsilon, k$.

For the velocities (u_m), at the free ambient water surface, a slip boundary condition is used. Thus, there are neither convective nor diffusive fluxes present at the top surface, but velocity values are calculated at the boundary. A no-slip condition, i.e., zero velocities at the boundaries, is applied to all solid boundaries of the tank domain. For the pressure p_m, a value of 1.013

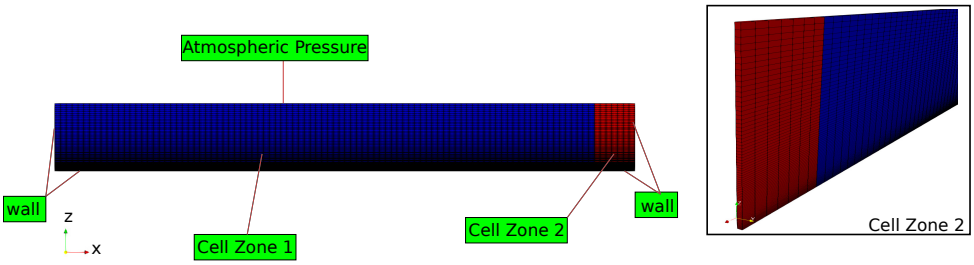

Figure 4.10: Geometry, mesh and boundary conditions used in the numerical simulations.

bar is used at the top surface of the tank to simulate the effect of atmospheric pressure, while zero gradient is used at all tank walls. In addition, the zero gradient for volume fractions α_k is assigned to all boundaries of the domain, including the free surface. A zero-gradient boundary condition guarantees that the volume fractions do not escape the domain, and that a bed builds up at the bottom boundary. The presence of walls affects the turbulent flow significantly. In the region near the wall, viscous damping and kinematic blocking reduce normal and tangential velocity fluctuations. Far from the near-wall region, turbulence increases rapidly because of the production of turbulent kinetic energy k. In the current study, wall functions are used for solid boundaries in order to link the viscosity-affected sub-layers between the fully turbulent and near-wall regions. For the free top surface, a zero- gradient BC is used for k and ϵ.

Grid Dependency

To investigate the influence of the mesh sizes, front position versus time is depicted for four different computational meshes. Three 2D meshes with 4800, 8000 and 16,800 cells and one three-dimensional (3D)mesh with 60,000 cells are selected to represent coarse, used, fine and 3D meshes, respectively. Experimental run7 is reproduced numerically, using the four proposed computational meshes, and the resulting distance–time figures are plotted in Figure 4.11. An adjustable time step is used, which means that a new time step is calculated at the end of the previous time step based on the Courant number $C = u\Delta t/\Delta x$. The Courant number represents how quickly information travels along the

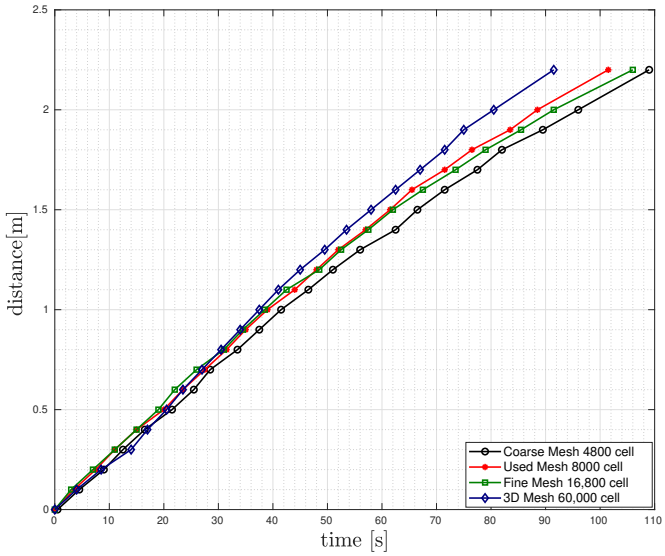

Figure 4.11: Grid-dependency study of numerical Run7. The front position of the current is plotted with respect to time for three different 2D meshes and one 3D mesh.

mesh cells. To have steady numerical runs, we keep C below 1.

The resulting distance–time curves for the four meshes compare very well, which means that the numerical solution can be considered mesh independent. To ascertain the mesh-independence of the solution in more detail, we also calculated the error in two cases: between used/fine meshes and used/3D meshes. Comparing the results of the used and fine meshes, we found that doubling the cell number yields an average difference of 1% in the values of time with respect to distance, while the average difference between the 3D and used meshes is found to be 6.43%. Both are in an acceptable range.

4.4.3 Number of Used Fractions Sensitivity Analysis

The number of the used fractions in the numerical runs is also a critical factor that can affect the simulation's accuracy in predicting the parameters associated with a turbidity current. Therefore, we must carry out a number-of-fractions sensitivity analysis to investigate the effect of the used

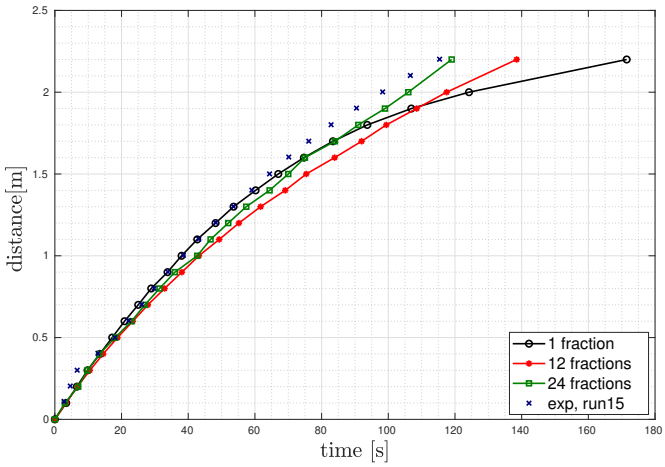

Figure 4.12: Sensitivity analysis for the number of the used fractions in the case of numerical run15. The front position of the current is plotted with respect to time for the number of used fractions of 1, 12, 24 and experimental results.

fractions number on the forward velocity of the currents. Run15 is reproduced numerically using number of fractions of 1, 12 and 24. The resulting distance–time curves for the numerical runs and the experimental run are plotted in Figure 4.12.

The potential energy that the mixture possesses before the gate is removed and the buoyancy forces resulting from the presence of solid particles are the main driving forces of a current. After removing the gate, the potential energy of a mixture transforms directly into kinetic energy. The effect of the kinetic energy on the driving force of the current decreases with time, and buoyancy forces become dominant. Following this understanding, in the first 60 s on the x-axis in Figure 4.12, front velocity compares well with experimental results because the driving forces were equal in all numerical runs. However, when the effect of the potential energy reduces and buoyancy forces become dominant, a degree of deviation is observed. As a result, beyond 60 s on the x-axis in Figure 4.12, in the case of 1 and 12 fractions used, a deviation from the experimental result can be observed. This deviation can be attributed to the change in buoyancy forces, since the number of fractions used significantly influences the buoyancy forces. As a result, the 24-fractions run compares well during the whole propagation time of the current, unlike the 1- and 12-fraction

runs. Therefore, using a more representable number of fractions of a sediment type in a numerical run will increase the accuracy of a simulated result.

4.5 Comparison of Numerical Simulations with Experiments

The predictions of the multi-phase drift–flux model are validated in this section. We compare the experimental results to the corresponding numerical results. Runs 1, 7 and 15 are reproduced numerically using the same initial conditions as in the experimental runs. Particle sizes were analysed through PSD testing for each sediment type in order to identify the quantities of each particle size present in the sediment. In addition, 14,12 and 24 fractions are used for Type1, Type2 and Type3, respectively. This information is used to set up the initial conditions of each numerical run.

Figure 4.13 compares the observed and simulated front position of the current versus time for runs 1, 7 and 15. The numerical model predicts the observed front position very well. This means that the simulations are capable of predicting the three phases of the current, i.e., the slumping, self-similar and viscous phases mentioned in the experimental results, Section 4.3.

Since it is also important to compare concentration distribution, two snapshots are taken at the same time frame and same front position in both the simulations and the experiments. The first snapshot is taken when the front of the current is almost at the middle of the tank, while the second snapshot is taken when the current reaches the end of the visualized region (see Figure 4.2). Two concentration profiles are taken per snapshot. For the first snapshot, the first profile is taken at the front of the current, at $\cong$ 1.6 m from the lock gate, while the second profile is taken at the body region of the current at a distance of $\cong$ 0.5 m from the lock gate. For the second snapshot, the front is taken to be at the end of the visualized region, which is $\cong$ 2.3 m from the lock gate and the second profile is at $\cong$ 1.2 m from the lock gate. In run1, only the first snapshot is taken at 24.5 s because the current is unquantifiable when it reaches the last third of the tank. For runs 7 and 15, the first snapshot is taken at 69.5 s and 73.1 s, while the second snapshot is taken at 113 s and 130 s, respectively.

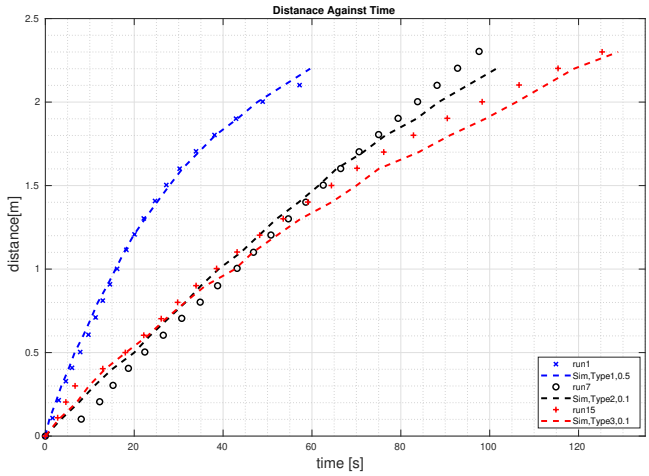

Figure 4.13: Validation cases for runs 1, 7 and 15. Front velocities of the numerical runs are compared to experimental runs.

Figures 4.14–4.16, show the experimental concentration profiles versus the simulated concentration profiles for runs 1, 7 and 15. Generally speaking, the numerical simulations show good agreement with the experimental data. Looking in more detail, a minor degree of divergence is observed between the experiments and simulations in all validation cases, which can be explained by two main factors:

1. The use of buoyant $k - \epsilon$ turbulence modelling, as this model introduces a degree of inaccuracy to the turbulence calculations.

2. The accuracy of the concentration calibration process in the experiments.

Various processes contribute to the turbulence process. One of the most important turbulence damping mechanisms in turbidity currents is damping by buoyancy forces, where solid-particle gravity forces oppose the upward flow fluctuations. This will result in a reduction in kinetic turbulence energy (Toorman et al., 2002). This mechanism could have a significant effect on the turbulence calculations even in low-concentration currents. Another damping mechanism is the reduction in turbulence kinetic energy due to the change

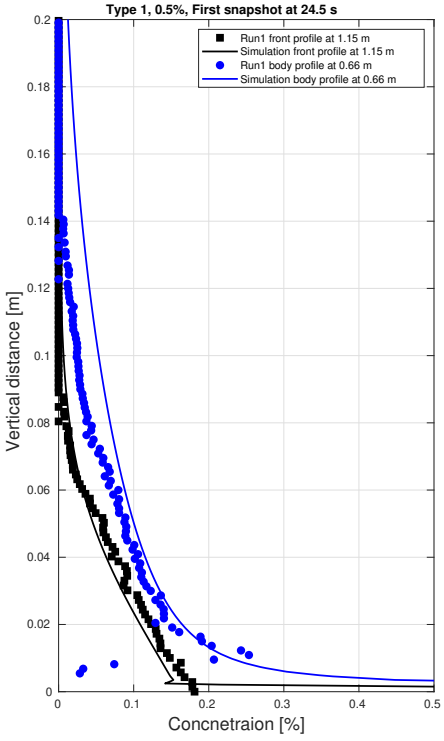

Figure 4.14: Validation case for run1. Vertical concentration profiles are shown for the front and the body of the current. The first snapshot is taken when the front of the current has almost reached the middle of the tank.

in the effective viscosity, which is why the presence of particles increases the bulk viscosity of the mixture (Toorman et al., 2002).

The standard $k - \epsilon$ model was originally developed on the basis of isotropic eddy viscosity and eddy diffusivity models. Accordingly, this model produces good estimations of turbulence calculations in non-stratified flows (Murakami et al., 1996). With stratified flows (e.g., turbidity currents), the model needs to be tweaked to account for the presence of sediment particles(Murakami et al., 1996). One of these modifications involves adding a buoyancy damping function term P_b to account for damped turbulence flux resulting from particle buoyancy. Note that this modification was made in the present study (see

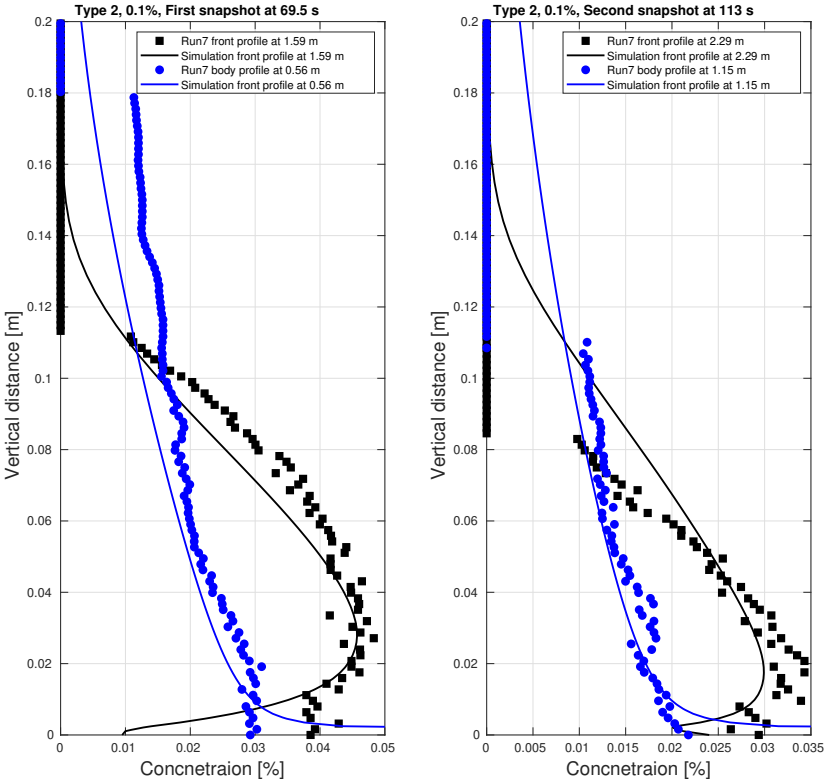

Figure 4.15: Validation case for run7. Vertical concentration profiles are shown for the front and the body of the current. The first snapshot is taken when the front of the current has almost reached the middle of the tank.

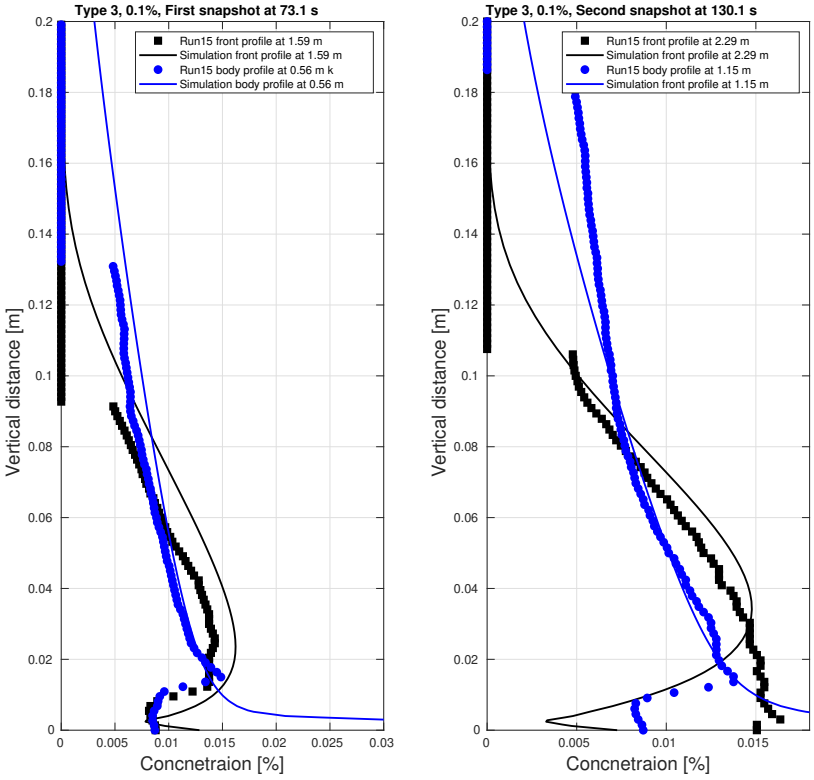

Figure 4.16: Validation case for run15. Vertical concentration profiles are shown for the front and the body of the current. The first snapshot is taken when the front of the current has almost reached the middle of the tank.

Equations (4.17) and (4.18)). However, our approach still lacks two other damping processes: the turbulence flux of momentum in the vertical direction and the extra vertical mixing between the flow layers due to the particles, i.e., turbulent wake resulting from particle deposition in the vertical direction. These two processes must be modelled in the $k - \epsilon$ model. In addition, an accurate estimation of the Schmidt number $Sc = \sigma_o F_m / F_s$ is needed, where F_m is the damping function for momentum, F_s is the damping function for the mixing and σ_o is the neutral Schmidt number. Normally, the F_m and F_s are calculated as a function of the Richardson number, which is defined as the ratio between buoyancy flux and flow shear (for more on estimating damping functions, see Toorman et al. (2002)). In addition to damping processes, another possible reason for the observed divergence is the wave at the tank surface caused by removing the lock gate, which is not taken into consideration. Moreover, there is a miss-estimation of the bed formed in the experiments because of the limitations of the calibration process (Section 4.2.2, Table 4.3). Keeping this in mind, the deviation between the experimental and numerical calculated concentration distribution at the bottom of the tank, i.e., first 2 cm on the y-axis Figures 4.14–4.16, can be attributed to the inaccuracy of the measured concentration distribution in the experiments.

To conclude, the damping processes mentioned here and the wave are the reasons for the minor degree of divergence observed in the vertical concentration profiles. However, for the sake of minimizing computational efforts and capturing the general trend of the current without extra costs, we consider that the multiple fractions drift–flux modelling approach can effectively predict the behaviour of a current in a good manner.

4.6 Conclusions

Particle size plays a major role in turbidity current propagation. In order to quantify turbidity currents generated by mining, this chapter investigated the effect of particle size and initial concentration on the propagation of turbidity currents experimentally and numerically. In the following context, the low-concentration turbidity currents and high-concentration turbidity currents are denoted to the currents of $\alpha \leq 1\%$ and $1\% \leq \alpha \leq 3\%$ of the initial concentration, respectively. Note that these conclusions are limited to by the tested run-out distance of the current, i.e., the tank length.

- Increasing initial concentrations inside the lock yields high front velocities independent of sediment type. In other words, the transition time to the self-similar phase increases when increasing the initial concentration.
- Increasing particle size leads to low front velocities. With coarse-particle, low-concentration currents, the turbidity current transitions to the self-similar phase more quickly, unlike fine-particle currents that take much longer to transition.
- Increasing initial concentrations neutralizes the particle size effect on current propagation.
- With high-concentration currents, coarse particles have little/no effect on the motion of the current compared to fine-particle currents with the same initial concentration, while in low-concentration currents, coarse particles settle and affect the forward velocity of the current.
- In case of fine-particle, low-concentration currents, low local concentration distribution values are observed during the propagation of the current.
- The new multiple fractions drift–flux model can satisfactorily predict how turbidity currents develop. It is important to remember that the number of fractions used is critical to the accuracy of the predictions, with a greater degree of accuracy being achieved when using a large number of fractions.

These findings can contribute to our understanding of the discharge process from a PNMT. Increasing particle size through flocculation and decreasing the initial concentration at the source might be beneficial in order to minimize environmental impact. Another key point is that the drift–flux model can be utilized to predict the behaviour of turbidity flows behind mining tools. Furthermore, the drift–flux model can be an acceptable choice to optimize the momentum, volume and buoyancy fluxes at the discharge source.

The aggregation-breakup processes that occur between sediment particles during the discharge process and during turbidity current propagation is a matter of importance in any discharge process assessment. However, despite the fact that there are some studies about flocculation processes for deep-sea mininig applications (Gillard et al., 2019; Spearman et al., 2020), a

comprehensive understanding of flocculation is still lacking. Moreover, a properly validated numerical model that can predict particle size in the near-field region is still needed.

Chapter 5

Flocculation Effect in DSM-Generated Turbid flows

Abstract

A new hydrodynamic model of the PNMT mixture that captures sediment particle aggregation and breakup. Flocculation is expected to play an important role in defining the dispersion behaviour of the turbidity flows and the subsequent turbidity currents. The drift-flux model and the PBE are coupled in order to predict fluid hydrodynamics. Special attention is given to the settling velocity closure, since the formed flocs are porous and complex in geometry. The flocculation parameters are calibrated using the experiments of Gillard et al. (2019). Finally, we investigate the effect of flocculation in the near-filed region by solving the new model numerically on a computational domain of the near-field region. The results show that flocculation can lower the velocity of -and sediment suspension- in the generated turbidity current at the large distances and time scales associated with the near-field region.

Parts of this chapter have been published as Elerian, M., Huang, Z., van Rhee, C., Helmons, R. (2023). Flocculation effect on turbidity flows generated by deep-sea mining: A numerical study. Ocean Engineering, 277, 114250.

5.1 Introduction

Due to the difficulties in conducting in-situ testing, our understanding of the generated turbidity flows is limited. Direct measurements of these flows are rare because of turbulence in the wake region, the complexity of measuring the impingement zone, and the limited research on the interaction between discharged plumes and plumes from tracks. The focus of this chapter is to examine the flocculation in the discharged mixture, which is still a subject of ongoing research with numerous uncertainties and areas for further exploration. Lab experiments are crucial in this regard, as they allow for calibration and validation of numerical models to predict the behavior of turbidity flows in near and far regions (Elerian et al., 2021). Modeling of local characteristics of generated turbidity currents, such as velocity and concentration, is crucial for environmental impact predictions in DSM studies. Such predictions should be based on credible data. In this context, we aim to partially fill the current knowledge gap about the behavior of particles in the near-field region by creating a new modeling approach that predicts turbidity flow dispersion in that area.

Early studies investigating DSM turbidity flows have been reported in the literature (Jankowski et al., 1994; Purkiani et al., 2021; Zielke et al., 1995), but, to date, there have been few near-field numerical investigations dealing with DSM-generated turbidity flows. Decrop and Wachter (2019) presents a comprehensive two-phase CFD simulation of a PNMT discharge scenario, taking into account a variety of realistic conditions. Recently, Ouillon et al. (2021) conducted DNS simulations for a moving PNMT discharge process using the Boussinesq approach. This approach solves for a transport equation for buoyancy, along with Navier-Stokes and continuity equations. The results showed that when the PNMT's forward velocity is higher than the current's velocity, the forward velocity of the resulting turbidity current agrees with what is observed in lock-exchange tanks. While these studies give a basic understanding of the turbidity current structure in the near-field region, they do not consider the multiple particle size fractions and their interactions, such as aggregation and break-up processes. This could result in an incorrect estimation of particle settling velocity, which plays a significant role in determining the plume's behavior.

When particles collide in the presence of organic material and are in a

cohesive state, they can form a structure known as a "floc" through a process called "flocculation". Recently, researchers have recognized that flocculation plays a crucial role in DSM turbidity flows (Ali et al., 2022; Gillard et al., 2019; Gillard & Thomsen, 2019; Helmons et al., 2022; Muñoz-Royo et al., 2022; Spearman et al., 2020). Interestingly, Gillard et al., 2019 showed in a controlled laboratory experiment that under specific mixing conditions, the median particle size (d_{50}) of a CCZ (Clarion Clipperton Fracture Zone) sediment mixture can increase from 12 μm to 600 μm within just 7 minutes, indicating a rapid aggregation process between sediment particles. This leads to the firm conviction that flocculation could potentially serve as a crucial solution in reducing the impact of turbidity flows.

Shear-induced flocculation of multi-fraction sediment is primarily influenced by aggregation and break-up mechanisms, as revealed through experiments and numerical modeling of particle size distribution (PSD). Considerable effort has gone into developing a mathematical description of flocculation mechanisms, resulting in the creation of the "Population Balance Equation (PBE)"(Hounslow et al., 1988). PBE has gained widespread adoption among researchers in multiple fields for analyzing flocculation processes under fixed flow shear rates (Jeldres et al., 2015; Maggi, 2009; Mietta et al., 2011; Quezada et al., 2020; Ruan et al., 2021). The results obtained from PBE have been shown to have a strong correlation with experimental findings (Cahill et al., 1987; Fernández-Barbero et al., 1996; Russel et al., 1991). As most engineering problems are dynamic, with changing flow conditions over time, researchers often couple Computational Fluid Dynamics (CFD) models with PBE to efficiently analyze mixture dynamics and particle-size changes simultaneously (Bhole et al., 2008; Golzarijalal et al., 2018; Shi et al., 2019; Silva et al., 2008). These studies employ an Euler-Euler modeling approach, treating the water-sediment mixture as separate fluid and solid fractions based on size, as interpenetrating continua. PBE is coupled with the Euler-Euler model and both are solved simultaneously, resulting in a computationally intensive process. Each particle fraction requires its own momentum equation and PBE, adding to the complexity of solving the source terms that couple the momentum equations for both the liquid phase and the particle fraction.

In contrast to other models that treat particle fractions as separate phases, the drift-flux model takes a mixture approach, where the entire mixture is represented by a single momentum equation. However, this approach requires the inclusion of a phase transport equation for each particle fraction (J.

Goeree, 2018). Furthermore, the drift-flux model has been applied in different engineering applications (Alhaddad et al., 2020; Decrop & Wachter, 2019; de Wit, Talmon, et al., 2014; Elerian et al., 2022; J. Goeree, 2018; Van Rhee, 2002), supporting our choice for the model. To the best of our knowledge, the drift-flux model has been coupled with PBE in previous studies by Shen et al. (2018) and F. Chen et al. (2006), but both used only two or three phase PBE, which may affect the accuracy of predictions on a high-resolution grid. As shown in the work of Elerian et al., 2022, increasing the number of fractions leads to improved accuracy in predicting the forward velocity of turbidity currents. However, the suitability of their approach depends on the type of problem being studied and the desired outcomes. Our investigation focuses on the near-field region, with a higher resolution in the spatial, temporal, and phase domains than has been studied in previous works. This higher resolution has implications for the details of turbulence modeling and, in turn, flocculation modeling.

Building on the findings of Gillard et al. (2019), we have developed a new numerical model to improve the accuracy of turbidity-flow prediction behind a PNMT. This model includes the calibration of the most critical flocculation parameters. Our model's predictive capability stems from the combination of the drift-flux modeling approach, validated by Elerian et al., 2022, implemented in OpenFOAM, and the population balance modeling approach developed by Hounslow et al., 1988. The coupling of these two approaches would enhance the model's accuracy in predicting turbidity-flow. This will yield an improved understanding of turbidity flows in the near-field, from which we can gain insights into how discharge parameters impact the mixture dispersion in the near and far field regions. This could open up new opportunities for engineering solutions to address this issue. This chapter starts by outlining the PBE and the coupling procedure with the drift-flux model, as discussed in Chapter 4, in Section 5.2. Next, we calibrate the essential parameters of flocculation using the experimental work of Gillard et al. (2019) in Section 5.3. To demonstrate the impact of flocculation, we present a case study in Section 5.4. Finally, we draw conclusions in Section 5.5.

5.2 Mathematical Model

The flow of water-sediment mixtures, such as DSM turbidity flows, is described by the variable-density, incompressible Navier-Stokes equations. In the context of multi-phase flow, it is worth noting that the particle size distribution is partitioned into bins, with each treated as a separate phase. Previously in Chapter 4, we discussed the mathematical model used for this purpose, which was implemented using OpenFOAM, an open-source CFD code. However, this model does not account for the flocculation process. Hence, in the following subsection, we discuss the Population Balance Equation (PBE) and its closures and coupling procedures to the drift-Flux model reported in Chapter 4.

5.2.1 Population Balance Equation (PBE)

Aggregation and breakup are the two main processes that govern phase transition among solid particles. Despite flocculation being a complex process, Hounslow et al. (1988) presents a simple discretized equation that captures the transition of particles between phases. This discretization approach is based on size classes or size groups, in which the entire size range of sediment particles is divided into a specific number of groups. Each individual class is identified by its size, meaning that class k contains one size-based fraction. For simplicity, each class is treated as a phase, with the subscript k representing the class. The discretization approach is based on the idea that the volume of a particle in phase $k+1$ is double that of a particle in phase k.

$$v_{k+1} = 2v_k, \tag{5.1}$$

where v_k is the particle size in class k. Bearing this in mind, the discretized form of PBE can be described as follows:

$$\frac{dN_k}{dt} = \sum_{j=1}^{k-2} 2^{j-k+1}\gamma\beta_{k-1,j}N_{k-1}N_j + \frac{1}{2}\gamma\beta_{k-1,k-1}N_{k-1}^2 - N_k\sum_{j=1}^{k-1} 2^{j-k}\gamma\beta_{k,j}N_j - N_k\sum_{j=k}^{kmax}\gamma\beta_{k,j}N_j - S_kN_k + \sum_{j=i}^{imax}\zeta_{k,j}S_jN_j, \tag{5.2}$$

where $N_k(\#/m^3) = \alpha_k/\upsilon_k$ is the number concentration in particles of phase k, γ is the collision efficiency, $\beta_{k,j}(m^3/s)$ is the collision frequency between particles in groups k and j, $S_k(s^{-1})$ is the breakage rate of particles in group k and ζ is the breakage distribution function which determines the volume fraction of particles of group k resulting from the fragmentation of particles of group j. Figure 5.1 provides a graphical representation of the RHS source terms of Equation 5.2, in which four functions that represent the particulate system are present; these functions are:

1. Collision efficiency γ,
2. Collision frequency $\beta_{k,j}$,
3. Breakage rate S_k,
4. Breakage distribution function ζ.

Such functions require closures, as they are the main driver of the phase transition process. Each closure will be discussed in the following subsections.

Collision Efficiency (γ)

The aggregation probability between two particles from different phases k and j can be described by the collision efficiency γ, which ranges from 0 to 1. When every collision results in floc formation, $\gamma = 1$. On the other hand, when no collision leads to floc formation, $\gamma = 0$. Determining the collision efficiency is a complex process as it depends on the surface properties of the

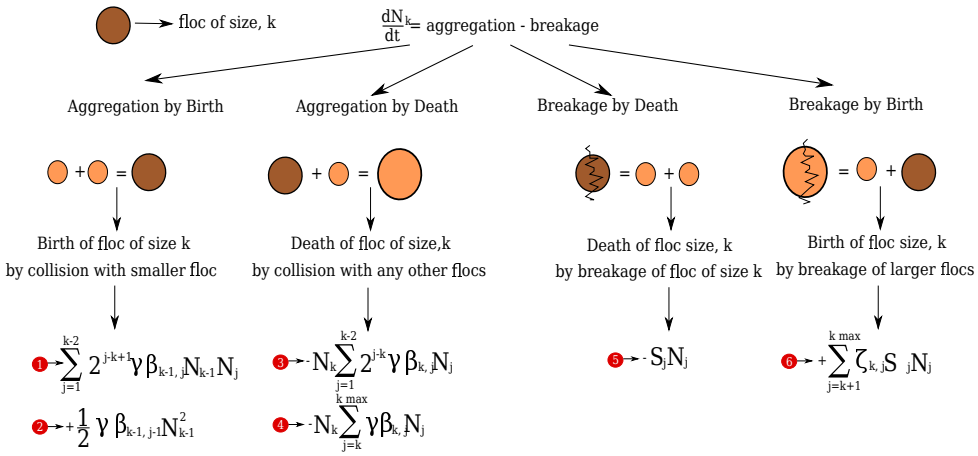

Figure 5.1: Aggregation an breakage dynamics of the discrtized PBE, Equation 5.2, adapted from (Biggs & Lant, 2002). Following Equation 5.2, first term is formation of floc k due to collision of unequal particle sizes, second term is formation of floc k due to collision of equal particle sizes, third term is death of floc k due to collision with smaller particles, fourth term is death of floc k due to collision with equal or large particles, fifth term is death of floc k due to breakage, sixth term is formation of floc k due to breakage of large particles.

particles, interaction forces between particles, and hydrodynamic effects within the aggregate. In some cases, γ is considered as a constant value (Biggs & Lant, 2002; Golzarijalal et al., 2018), while in others, it is considered as an adjustable parameter (Wickramasinghe et al., 2005; Zhang & Li, 2003). In this chapter, the value of γ is assumed to be 0.5 for all simulations.

Collision Frequency ($\beta_{k,j}$)

Assessing the frequency of collisions is challenging due to the intricate interaction of various factors, including:

1. Perikinetic aggregation of flocs, i.e. Brownian motion, $\beta_{k,j}^{Br}$,
2. Orthokinetic aggregation of flocs, i.e. aggregation occurs because of a velocity gradient in a fluid, $\beta_{k,j}^{sh}$,
3. Gravity aggregation,i.e. differential settling, $\beta_{k,j}^{g}$.

For any given two particles, each of which belongs to a different phase k or$j$, collision frequency is calculated as follows:

$$\beta_{k,j} = \beta_{k,j}^{Br} + \beta_{k,j}^{sh} + \beta_{k,j}^{g}. \tag{5.3}$$

The flocs resulting from an aggregation process are irregular, permeable structures. Two parameters are introduced by (Veerapaneni & Wiesner, 1996) to correct for the fluid collision efficiency,

1. The efficiency of fluid accumulation inside a floc η,
2. The ratio of the drag force of a permeable aggregate to the drag force of an impermeable aggregate Ω.

The collision efficiency between permeable and irregular flocs is thus given by the following equations:

$$\beta_{k,j}^{Br} = \frac{2k_bT}{3\mu}\left(\frac{1}{\Omega_k r_k} + \frac{1}{\Omega_j r_j}\right)(r_k + r_j), \tag{5.4}$$

$$\beta_{k,j}^{sh} = 1.294G\left(\sqrt{\eta_k}r_k + \sqrt{\eta_j}r_j\right)^3, \tag{5.5}$$

$$\beta_{k,j}^{g} = \pi\left(\sqrt{\eta_k}r_k + \sqrt{\eta_j}r_j\right)^2 |(u_{kr} - u_{jr})|, \tag{5.6}$$

where r_k is the effective capture radius of an aggregate of phase k, k_b is Boltzman constant, T is the temperature, $G = (\epsilon/\nu)^{1/2}$ is the shear rate and μ is the dynamic viscosity. Considering the fractal dimension, the value of a floc's effective radius is determined by the following equation (Flesch et al., 1999):

$$r_k = r_2(\frac{\upsilon_k}{\upsilon_2})^{1/d_f}, \tag{5.7}$$

where $r_2 = d_2/2$ is the primary particle radius, d_f is the fractal dimension, which ranges from 1 to 3, with 1 being line of particles and 3 is a solid sphere. The irregular shape and the permeability of a floc are governed by the value of d_f , making it a critical factor for flocs structure. Ω in Equation 5.4 is the ratio between the force exerted by the fluid on a permeable aggregate and

the force exerted by the fluid on an impervious sphere of an equivalent size (Jeldres et al., 2015), it is given by:

$$\Omega = \frac{2\xi^2\left(1-\frac{tanh\xi}{\xi}\right)}{2\xi^2+3\left(1-\frac{tanh\xi}{\xi}\right)}, \tag{5.8}$$

where $\xi = r/\sqrt{K}$ is the dimensionless permeability, in which K is the permeability of an aggregate. We employ the Brinkman and Happel permeability equation to calculate the K (Li & Logan, 2001),

$$K = \frac{d_2^2}{72}\left(3+\frac{3}{1-\phi}-\sqrt[3]{\frac{8}{1-\phi}-3}\right), \tag{5.9}$$

where ϕ is the porosity of a floc, which is calculated using the fractal dimension approach:

$$\phi = 1 - C_b\left(\frac{d_k}{d_2}\right)^{d_f-3}, \tag{5.10}$$

where C_b is the packing coefficient, which is assumed to be 1 in this work. As demonstrated by Equation 5.10, there is an inverse relationship between fractal dimension and floc porosity. As the fractal dimension increases, the floc porosity decreases. This trend continues until the fractal dimension reaches its maximum value of $d_f = 3$, at which point the floc porosity reaches its minimum value of 0, indicating a solid case with no voids or pores, (Li & Logan, 2001).

Following Equations 5.5 and 5.6 and the Brinkman equations (Wickramasinghe et al., 2005), η is calculated using the following equation(Biggs & Lant, 2002):

$$\eta = 1 - \frac{d}{\xi} - \frac{c}{\xi^3}, \tag{5.11}$$

where

$$d = \frac{3}{J}\xi^3 \left(1 - \frac{tanh\xi}{\xi}\right), \tag{5.12}$$

$$c = -\frac{1}{J}\left(\xi^5 + 6\xi^3 - \frac{tanh\xi}{\xi}\left(3\xi^5 + 6\xi^3\right)\right), \tag{5.13}$$

$$J = 2\xi^2 + 3 - 3\frac{tanh\xi}{\xi}. \tag{5.14}$$

Breakage Rate (S_k)

In general, a floc breaks up when the imposed external force on the floc exceeds the floc's strength. The breakage rate S_k is determined as follows (J. C. Winterwerp, 1998):

$$S_i = E_b G \left(\frac{d_k - d_2}{d_2}\right)^{3-d_f} \left(\frac{\mu G}{F_y/d_k^2}\right)^{\frac{1}{2}}, \tag{5.15}$$

where F_y is floc strength. Very little is known about F_y, but Van Leussen, 1994 estimated it to be approximately $10^{-10}N$. E_b is the breakage coefficient.

Breakage distribution function

Determining the size distribution of daughter flocs produced from the breakup of a parent floc is challenging. Theoretical breakup distribution functions are used to find the best fit for the experimental data. In this chapter, we adopt a binary breakage function, which we believe will be adequate, as discussed in (W. Chen et al., 1990; Jeldres et al., 2015).

$$\zeta_{k,j} = \frac{v_j}{v_k},\ j = k+1\ and\ \zeta_{k,j} = 0\ for\ j \neq k+1. \tag{5.16}$$

5.2.2 Coupling Between Drift-Flux Model and PBE

We couple fluid dynamics and phase transition by using the relationship between the number density N_k and the volume concentration of particle phase, which remains constant over time.

$$N_k = \frac{\alpha_k}{\upsilon_k}. \tag{5.17}$$

From Equation 5.17 and Equation 4.7 we can deduce the following equation:

$$\begin{aligned}\frac{\partial \alpha_k}{\partial t} + \nabla.(\alpha_k(\mathbf{u_m} + \mathbf{u_{km}})) = \Bigg[& \upsilon_k \sum_{j=1}^{k-2} 2^{j-k+1} \gamma \beta_{k-1,j} N_{k-1} N_j \\ & + \frac{1}{2} \upsilon_k \gamma \beta_{k-1,k-1} N_{k-1}^2 - \upsilon_k N_k \sum_{j=1}^{k-1} 2^{j-k} \gamma \beta_{k,j} N_j - \\ & \upsilon_k N_k \sum_{j=i}^{imax} \gamma \beta_{k,j} N_j - S_k N_k \upsilon_k + \upsilon_k \sum_{j=i}^{imax} \zeta_{k,j} S_j N_j \Bigg] + \nabla.\Gamma_t \nabla \alpha_k.\end{aligned} \tag{5.18}$$

Thus, we replace Equation 4.7 by Equation 5.18, obtaining a particle of phase k that travels through time, space (advection and diffusion), and phase domains (i.e, volume as an internal coordinate). Subsequently, the proposed model is implemented using OpenFOAM, an open-source CFD code, as illustrated in Figure 5.2.

5.2.3 Settling Velocity

Investigating flocculation issues requires a close examination of the PSD, as it plays a crucial role in determining the effects of flocculation on mixture hydrodynamics. The PSD of CCZ is analyzed by Gillard et al. (2019), and the results provide a key starting point for further modeling efforts (as seen in Fig. 5.3).

The PSD used in this chapter is taken from the 8MUC location and divided into 27 fractions. The smallest fraction, known as the "primary phase," is $d_{k=2} = 2\mu m$ with density $\rho_{k=2} = 2650$. The largest fraction, which is based on the maximum floc size found by Gillard et al. (2019) in three experimental cases, is $d_{k=28} = 812.74\mu m$ (refer to Fig. 5.3). The intermediate fractions were calculated using the discretization rule in Equation 5.1. Note that a correction is made to the 27 fraction PSD curve to ensure that the area under the curve remains equal to one. This correction is necessary to account for

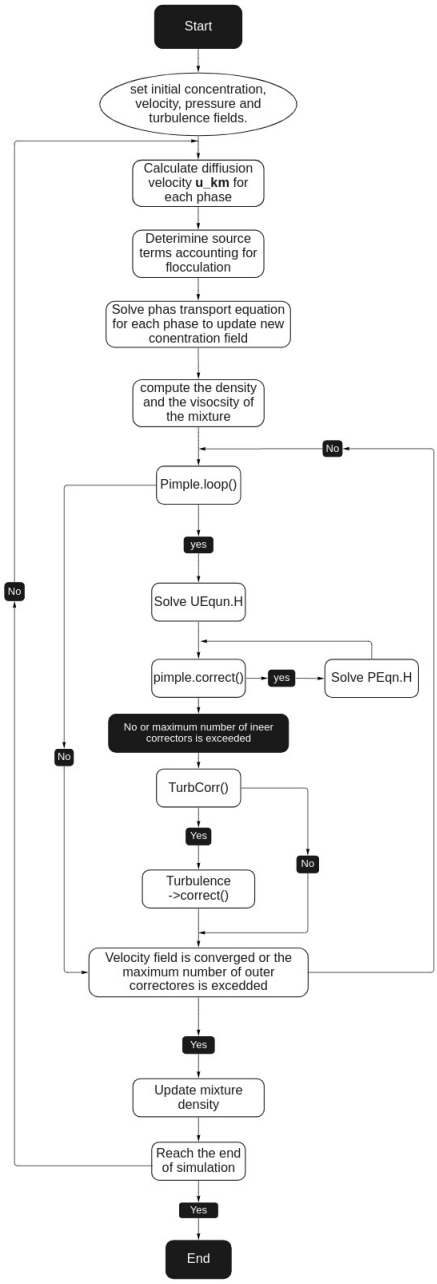

Figure 5.2: Flow chart of the solver algorithm in OpenFOAM.

the difference between the original PSD curve of Gillard et al. (2019) and the selected PSD used in this chapter.

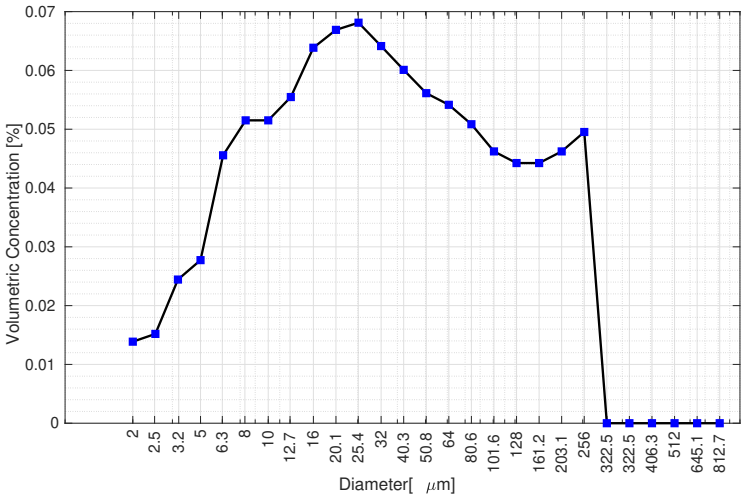

Figure 5.3: PSD of the 8 MUC location in the CCZ Gillard et al., 2019. The blue points represents the corrected 27 fractions used in this chapter.

In shear-induced flows, aggregation of particles results in an increase in floc size and a decrease in density as water becomes trapped within the flocs during the aggregation process. This has a direct impact on the settling velocity of the flocs, which then affects the accuracy of predictions for mixture hydrodynamics. To account for these changes, we use an improved definition of settling velocity that takes into account the floc density by incorporating the primary particle size ($d_{k=2}$) and the fractal dimension (d_f). This updated formula extends the one proposed by Ferguson and Church (2004) and is as follows:

$$u_{kr} = \frac{R_{s,k} g d_k^2}{b_1 \nu_c + (0.75 b_2 R g d_k^3)^{1/2}}, \tag{5.19}$$

where ν_c is the kinematic viscosity of the carrier fluid (water), and b_1 and b_2 are coefficients that account for particle shape and drag, respectively. $R_{s,k} = (\rho_k - \rho_1)/\rho_k$ represents the submerged specific gravity and highlights the correlation between floc density and settling velocity. $R_{s,k}$ is calculated differently as per Kranenburg (1994) and Strom and Keyvani (2011), as follows:

$$R_{f,k} = R_{s,k} \left(\frac{d_k}{d_2} \right)^{d_f - 3}, \tag{5.20}$$

By substituting Equation 5.20 with Equation 5.19, we arrive at a general explicit formulation for the settling velocity of a floc as follow:

$$u_{kr} = \frac{R g d_k^{d_f - 1}}{b_1 \nu_c d_2^{d_f - 3} + b_2 (0.75 R g d_k^{d_f} d_2^{d_f - 3})^{1/2}}. \tag{5.21}$$

5.3 Numerical Model

The mathematical description of the flow of water-sediment mixtures, such as DSM turbidity flows, is given by the variable-density, in-compressible Navier-Stokes equations. In the context of multi-phase flow, it is important to note that the particle size distribution is divided into bins, each of which is treated as a separate phase. The governing equations are solved sequentially using the Finite-Volume Method (FVM). Accordingly, the equations are integrated at each computational cell, yielding discretized equations for each quantity.

5.3.1 Experiments

Gillard et al. (2019) study DSM-generated turbidity flows, where the flocculation process is quantified experimentally. To our knowledge, the flocculation parameters that we believe to play the largest role in controlling aggregation and breakup processes, , i.e. d_f and E_b, have not been calibrated for CCZ-type sediment. The exact values and sensitivity of these parameters therefore remain unknown, which is why we use the experimental results of Gillard et al. (2019) to calibrate and in Equation 5.17 to predict as accurately as possible. It is worth noting that despite Gillard et al. (2019)'s extensive research on real CCZ sediment, an important limitation of their study is the absence of in-situ CCZ water. The use of natural water is crucial in understanding the aggregation process in CCZ environments. As a result, the experimental work in Gillard et al. (2019) did not fully consider the impact of key factors such as extracellular polymeric substances (EPS) and bacteria present in real CCZ water on the aggregation of particles. However, to the best of our knowledge,

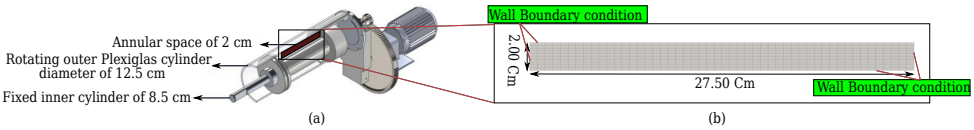

Figure 5.4: (a) Couette reactor setup. (b) The 2D mesh used in numerical runs.

this is still the only work in the literature that has detailed laboratory results for CCZ sediment.

Gillard et al. (2019) used a horizontal Couette reactor (Figure 5.4) to create a homogeneous shear rate. The reactor consists of a fixed inner cylinder and a rotating outer cylinder with a 2 cm wide annular space between the walls and a total working volume of 1.7 liters. The shear flow is generated by rotating the outer cylinder. The floc aggregation process is observed over time using a camera, as the outer chamber is made of transparent acrylic glass. The mixture is tracked during each experimental run.

5.3.2 Numerical Domain

A 2D mesh is created using OpenFOAM's block-Mesh utility to represent a horizontal slice of the Couette reactor's working volume (see fig. 5.4). The mesh is 25.7 cm long and 2 cm high. All sides are assigned a Wall Boundary Condition (B.C), with a no-slip B.C assigned to velocity, a zero gradient assigned to pressure, wall functions assigned to k and epsilon, and a zero gradient assigned to α_k.

In the model, turbulence inside the Couette reactor is kept constant due to the constant angular velocity created by the rotation of the outer wall, resulting in a constant shear rate G throughout an experimental run. Despite the constant turbulence in the experiments, the turbulence model (Equations 4.17 and 4.18) is not activated during the simulation, as constant values are assigned to k and ϵ, which are used to calculate Γ in Equation 5.18 and ν_m^t in Equation 4.4. The current study focuses solely on calibrating the most effective flocculation parameters in the RHS of Equation 5.17

The shear rate in an experimental run is used to calculate the value of ϵ for

each case by using the equation $G = (\epsilon/\nu_m)^{0.5}$. The turbulence length scale relation is then used to determine k as follows:

$$\epsilon = \frac{C_\mu^{0.75} k^{1.5}}{L}, \tag{5.22}$$

where L is taken as $0.02m$, the distance between the outer and inner walls of the reactor. The volumetric concentration α_k of each phase is then averaged over the entire domain, leading to the determination of d_{50}.

5.3.3 Settling Velocity Calibration

It is important to note that of the seven flocculation parameters E_b, d_2, C_b, d_f, b_1, b_2, only three d_f, b_1, and E_b are considered for calibration, as they have been found to have a high impact on the results, while the other four have been found to have only a slight impact.

As mentioned in the work of Ferguson and Church, 2004, the values of b_1 range from 18 to 24 and b_2 range from 1 to 1.2 for sand. However, when dealing with flocculation, the fractal dimension d_f plays a crucial role as it describes the space-filling ability of real flocs. According to Strom and Keyvani, 2011, the settling velocity changes with the variation of the fractal dimension. Therefore, we determine the particle shape parameter b_1 corresponding to the tested fractal dimension by calibrating the measured settling velocity of Gillard et al., 2019 to the results of equation 5.21, using the specific fractal dimension being tested. This allows us to determine the optimal value of b_1, taking into account that we found that the value of b_2 did not have a significant impact on the results and is thus kept constant at 1.5.

Gillard et al. (2019) conducted settling velocity measurements which are used to calibrate parameters b_1 and b_2 in Equation 5.21. The particle sizes varied from an initial $d_{50} = 20\mu m$ to the maximum floc size in each case. The results from Equation 5.21 are compared to the experimental results and the case-dependant empirical formulas from Gillard et al. (2019) are used.

Figure 5.5 shows the calibration of parameter b_1 using different values of d_f. In Section 5.3.4, the fractal dimension for each of the 3 test cases is determined. The settling velocity measurements in the figure are case-specific. The results from Equation 5.21 agree well with the experimental results.

However, there is some discrepancy between the measured and calculated settling velocities, particularly in the low-shear rate conditions and for small particle sizes. This divergence may be attributed to several factors including:

- The uncertainty about the primary particle size d2.
- Assuming a constant fractal dimension for the entire size range of particles.
- As a result, changes in fractal dimension can also affect the particle shape coefficient b_1, which can ultimately impact the calculations.

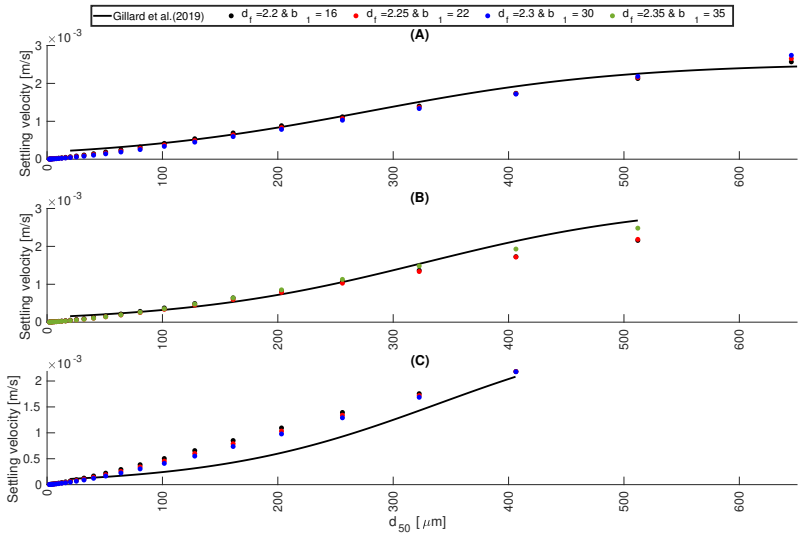

Figure 5.5: Calibration of the modeled settling velocity u_{kr} using the experimental results of (Gillard et al., 2019). (A): calibration process for 500 mg/l and 10.4 s^{-1}. (B): calibration process for 175 mg/l and 5.7 s^{-1} . (C): calibration process for 105 mg/l and 2.4 s^{-1}.

5.3.4 Calibration Results

The calibration set consists of three distinct cases, each characterized by a unique combination of mass concentration and shear rate. The concentrations tested are 500, 175, and 105 mg/l, paired with shear rates of 10.4, 5.7, and 2.4 s^{-1} respectively. These varied conditions allow for a comprehensive evaluation

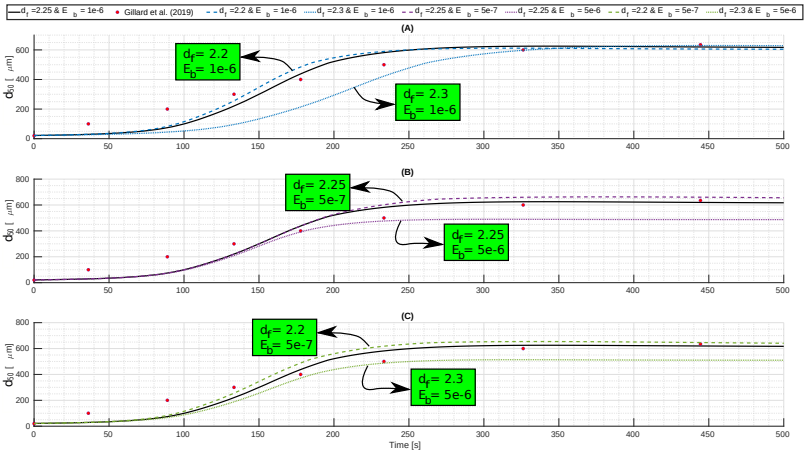

Figure 5.6: Calibration process in case of 500 mg/l mass concentration and 10.4 s^{-1} shear rate. All 3 figures show the development of d_{50} over time. (A) represents the sensitivity of the fractal dimension d_f on the numerical results, where the the breakage coefficient $E_b = 1 \times 10^{-6}$ is constant. (B) represents the sensitivity of the breakage coefficient, where for blue curves the $d_f = 2.3$ is constant. (C) represents the sensitivity of both parameters d_f and E_b on the development of d_{50}.

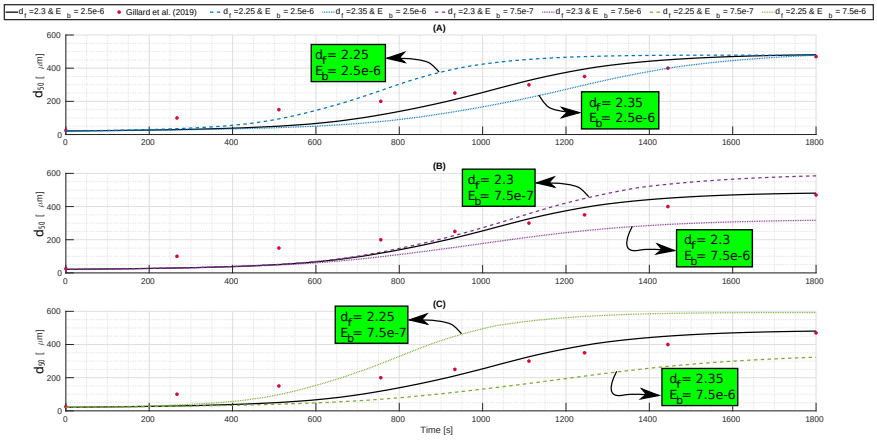

Figure 5.7: Calibration process for 175 mg/l mass concentration and 5.7 s^{-1} shear rate. All 3 figures show the development of d_{50} over time. (A) represents the sensitivity of the fractal dimension d_f on the numerical results, where the the breakage coefficient $E_b = 1 \times 10^{-6}$ is constant. (B) represents the sensitivity of the breakage coefficient, where for blue curves the $d_f = 2.3$ is constant. (C) represents the sensitivity of both parameters d_f and E_b on the development of d_{50}.

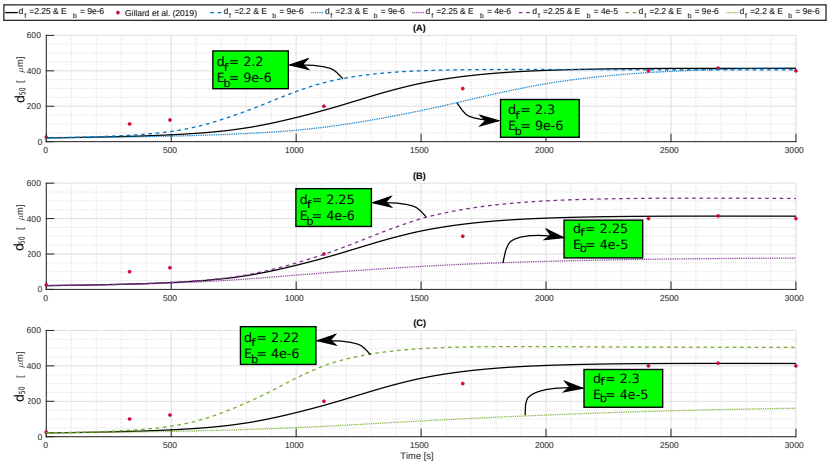

Figure 5.8: Calibration process in case of 105 mg/l mass concentration and 2.4 s^{-1} shear rate. All 3 figures show the development of d_{50} over time. (A) represents the sensitivity of the fractal dimension d_f on the numerical results, where the the breakage coefficient $E_b = 1 \times 10^{-6}$ is constant. (B) represents the sensitivity of the breakage coefficient, where for blue curves the $d_f = 2.3$ is constant. (C) represents the sensitivity of both parameters d_f and E_b on the development of d_{50}.

of flocculation behavior. Our observations indicate that the fractal dimension and breakage coefficient play a crucial role in determining the flocculation source terms, highlighting their significance in this process. In each case, the values that fit closest to the experimental results are used as reference values, with the side note that they are determined through trial and error. The best fit for each case is represented graphically as a solid black line in Figures 5.6, 5.7, and 5.8. To determine the sensitivity of the parameters, additional numerical runs are performed by varying the values of either d_f or E_b, or both. These additional experiments are depicted in (A) for d_f only, (B) for E_b only, and (C) for both d_f and E_b combined, in Figures 5.6, 5.7, and 5.8.

The results of the numerical simulations and experiments are compared and a good agreement is found for a range of fractal dimension and breakage coefficient values. The best fit for each case is shown as a solid black line in Figures 5.6, 5.7 and 5.8. The values of d_f and E_b are relatively similar from case to case, which is anticipated as they represent the same sediment. These results provide us with the necessary confidence to use these values in real-world applications (as discussed in Section 5.4). Given the complexity

and uncertainty associated with these parameters, it is deemed acceptable to use any value within the specified range to a certain extent.

In all cases, the solid black lines deviate from the experimental observations at the start of the simulation, but they begin to match more closely soon after. The deviation in the numerical prediction of d_{50} is higher when E_b is changed compared to when d_f is changed. The undervaluation of d_{50} increases as E_b decreases and vice versa. The deviation caused by changing d_f is more prominent at the start of the numerical simulation. It is clear that as the initial concentration and shear rate decrease, the sensitivity of E_b increases (as seen in B and C in Figure 5.8), leading to greater inaccuracies in the prediction of d_{50}. It could be that the overall deviation occurs due to:

1. The uncertainty in the initial particle size distribution (PSD) can have an impact on the calculation of the initial phase concentration (α_k), particularly during the early stages of a numerical run.

2. Only a small number of fractions are used;

3. The uncertainty of the constant values assigned to different parameters such as d_f, E_b and b_1;

4. The assumption of the primary particle size being $d_2 = 2\mu m$;

5. The shear rates explored in the study are relatively low, which could allow sediment particles to settle during the experiment, potentially impacting the accuracy of the measurements.

6. The possibility that the source terms of the PBE are only approximate.

It is critical to conduct a sensitivity analysis of parameters such as d_f and E_b before starting a numerical investigation, as improper estimation of these values may lead to significant over- or under-estimation of d_{50}, as demonstrated in (C) of Figures 5.6, 5.7 and 5.8. Fortunately, the ranges of the parameters for the three cases investigated in this chapter, namely $2.25 \leq d_f \leq 2.3$ and $2.5 \times 10^{-6} \leq E_b \leq 9 \times 10^{-5}$, are considered valid for use in CCZ sediment case studies. However, it is important to conduct a sensitivity analysis for each individual sediment type prior to applying the numerical model.

5.4 Case Studies

The multi-phase-drift-flux model has been previously validated through experimental studies conducted by Elerian et al. (2022) and mentioned in Chapter 4. The results of our analysis have demonstrated that the flocculation source terms of the model are effective in predicting the median grain size d_{50} of a water-sediment mixture. With this validation and calibration, we can now move forward to explore the impact of flocculation on turbidity current dispersion in the near-field region, which will be the focus of the next section.

5.4.1 Numerical Domain

As a PNMT travels along the seabed, it creates a highly turbulent region in its wake. The sediment particles generated by the PNMT are then subjected to high levels of mixing and increased chances of particle collisions, which can lead to either the aggregation of particles or the breakup of newly formed flocs. With the aim of investigating the effects of flocculation in the near-field region, we will be using the newly-developed model to conduct two main simulations as follow:

1. With flocculation;
2. Without flocculation, i.e. the 6 flocculation terms in equation 5.17 = 0.

Additionally, we have established in Subsection 5.3.4 that the flocculation behavior is highly dependent on d_f and E_b. To further understand the impact of these parameters on the near-field region, we conduct four additional simulations, each varying the values of d_f and E_b by ± 0.5 and $\pm 5 \times 10^{-7}$, respectively, from the values used in Run 1. The complete details of all numerical simulations performed can be found in Table 5.1. Runs 1 and 2 are the main simulations, with one examining the effects of flocculation and the other without, while Runs 3-6 are designed to assess the sensitivity of the flocculation parameters as outlined in Subsection 5.4.5.

It is further to be noted that for the no-flocculation case (Run2), a non-cohesive sediment (e.g. sand) should be used, so the simulation should start with the PSD of the 8 MUC location (same initial spectrum of the flocculation

Table 5.1: The values of d_f and E_b used in the numerical runs.

Runs	1	2	3	4	5	6
d_f	2.25	2.25	2.2	2.3	2.25	2.25
E_b	5e-6	0	5e-6	5e-6	1e-7	1e-6

case, see Figure 5.3), considering it as sand. The settling velocity for the no-flocculation case is calculated using the Ferguson formula (Equation 5.19) for the sand fractions throughout the simulation. However, using this approach for comparison with the flocculation case is invalid as the latter uses Equation 5.21. Therefore, while comparing the results, not only the phase transition will be the changing parameter but also the settling velocity, which can affect the conclusions regarding the observed difference in the numerical results. Consequently, this can affect the conclusions regarding whether the observed difference in the numerical results is due to using different settling velocity formulas or because of the phase transitions. Therefore, we unify the settling velocity calculations using only Equation 5.21 for both cases with a $d_f = 2.25$, allowing the phase transition to be the only changed parameter. In other words, when we use the term "no-flocculation" case, we are referring to a scenario where there is no phase transition occurring (i.e. the particle size distribution is only affected by transport mechanisms and not the phase transition). In this case, we assume that the settling velocity of the particles is calculated in the same way as in the flocculation case. By making this assumption, we can isolate the effect of the phase transition on the settling behavior of the particles and better understand flocculation impact.

The computational domain, with dimensions of 20 m in height, 35 m in width, and 120 m in length, is depicted in Figure 5.9. The length of the domain, 120 m, is selected to accommodate the flocculation process, as it requires substantial time and length scales to occur effectively. Preliminary simulations, not depicted, indicated that a sufficient distance should be maintained between the INLET, SIDE, TOP, and PNMT boundaries to prevent pressure disturbance between the boundaries. As depicted in Figure 5.9, the positioning of the PNMT back is set at 18 m from the INLET boundary, the side of the PNMT is placed at 34 m from the SIDE boundary, and the PNMT top is positioned at 16.5 m from the TOP boundary to ensure the aforementioned distance requirements are met, as established by the preliminary simulations. As shown in Figure 5.9, the PNMT geometry is kept simple, as the main objective of

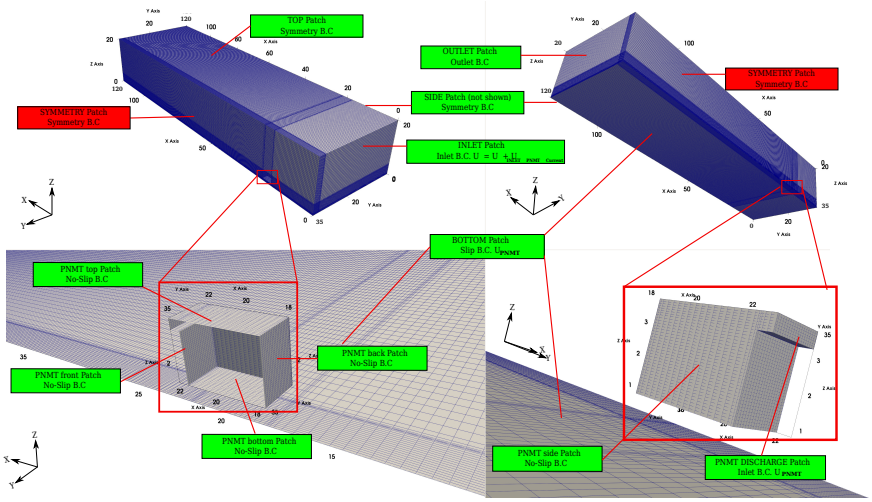

Figure 5.9: Geometry used in all numerical simulations with the name of the relevant B.C. The top figures depict half of the domain, utilizing symmetry B.C as indicated by the red tag, while the bottom figures show the geometry for the PNMT. The unrepresented half of the domain is mirrored along the ZX plane for post-processing analysis. The flow direction is in the positive X direction with a positive discharge.

the simulation is not to optimize PNMT geometry, but rather to study the flocculation process. Additionally, it is important to note that our study does not take into account the effects of any aggregation or breakage that may occur within the PNMT, keeping in mind that the collection process is highly turbulent due to the high velocity jets involved, which may impact the behavior of particles Alhaddad and Helmons, 2023. The background oceanic current is assumed to be 0.1 m/s, as reported in (GSR, 2018). As this is a moving source problem, the PNMT is considered the reference frame, with a forward speed of 0.5 m/s, which is equal and opposite in direction to the mixture discharge velocity, as reported in (Gillard & Thomsen, 2019; GSR, 2018). It is worth mentioning that the PNMT moves in the negative X direction. Our hypothesis is that discharging the mixture at a velocity equal to the forward speed of the PNMT would result in an immediate transition to the negative buoyancy phase, minimizing dispersion due to the expected lower velocity of the generated turbidity current. It is important to note that the focus of this chapter is not to examine the impact of varying discharge velocities or PNMT speeds, but to investigate the effects of flocculation in the near-field region. Given that the PNMT serves as the reference frame, the bottom wall

Table 5.2: Boundary condition set up at different positions for all variables.

Boundaries	U $[m/s]$	$P_{\rho gh}$ $[pa]$	α_t [%]	k $\times 10^{-4}$ $[m^2/s^2]$	ϵ $[\times 10^{-6}]$ $[m^2/s^3]$
INLET	0.5	zero gradient	0	1.5	1.5
OUTLET	-	0	zero gradient	zero gradient	zero gradient
TOP	zero gradient	zero gradient	zero gradient	zero gradient	zero gradient
BOTTOM	0.5	zero gradient	zero gradient	0	0
SIDE	zero gradient	zero gradient	zero gradient	zero gradient	zero gradient
SYMMETRY	symmetry	symmetry	symmetry	symmetry	symmetry
All PNMT	0	zero gradient	zero gradient	Wall Function	Wall Function
PNMT DISCHARGE	0.6	zero gradient	1	1.5	1.5

of the PNMT has a speed equal to the forward speed of the PNMT, creating a boundary condition conflict between the bottom of the PNMT (no-slip boundary, U = 0 m/s) and the BOTTOM boundary (slip boundary, U = 0.5 m/s). However, it is assumed that the sediment disturbance caused by the PNMT tracks would be negligible compared to the discharge source from the PNMT. To account for this, a 0.8 m empty space is maintained between the boundaries, as seen in the right-bottom figure in Figure 5.9.

Leveraging the symmetry of the problem, only half of the domain is solved and the result is mirrored across the XZ plane during post-processing, effectively reducing the computing power required by half. Table 5.2 and Figure 5.9 show the boundary conditions for various variables. The simulation is run for 250s to ensure a steady-state case for the turbid flow, even though a simulation time of 200s is sufficient for the PNMT to traverse the 100m domain length. A single run takes about 5 days on 64 cores of the Delft-Blue supercomputer ((DHPC), 2022).

5.4.2 Mesh Structure and Sensitivity

The computational mesh consists of approximately 3.5 million cells. To capture the density difference in front of the PNMT, grid clustering with increased resolution is applied in the positive x, y, and z directions. The cells in the first 4m have a height of 3cm, length of 20cm, and width of 10cm, while those in other regions are 50cm in all directions. The cell size around the PMNT gradually increases with a growth rate of 1.003 in the normal direction of each

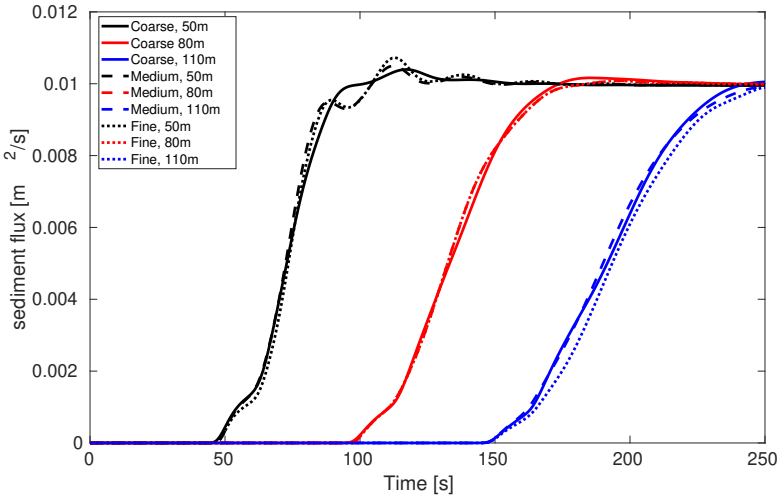

Figure 5.10: Comparison of sediment flux in coarse, medium and fine mesh. In each case, three x-normal slices are considered at 50 m, 80 m and 110 m.

PNMT boundary.

In addition to the coarse mesh described above, two other meshes, the medium and fine, are considered to evaluate the solution's dependence on the number of cells. The medium mesh has approximately 6.5 million cells and represents a 1.25-fold increase, while the fine mesh has approximately 11.5 million cells and represents a 1.5-fold increase in cells compared to the coarse mesh. The sediment flux, represented by $\alpha_t \times U_{m,x} \times A$, is chosen as the key metric in this chapter. Our analysis of the sediment flux over time in three cross-sections of 50m, 80m and 110m, as shown in Figure 5.10, revealed minimal variations among the meshes. For this reason the coarsest mesh is used for this chapter.

5.4.3 Flocculation Nature

To understand the behavior of turbid flows in the near-field region, we compare cases with and without flocculation. This comparison will highlight the significance of flocculation and provide insight into whether it can play a role in reducing the turbidity flows caused by DSM. To do so, we monitor

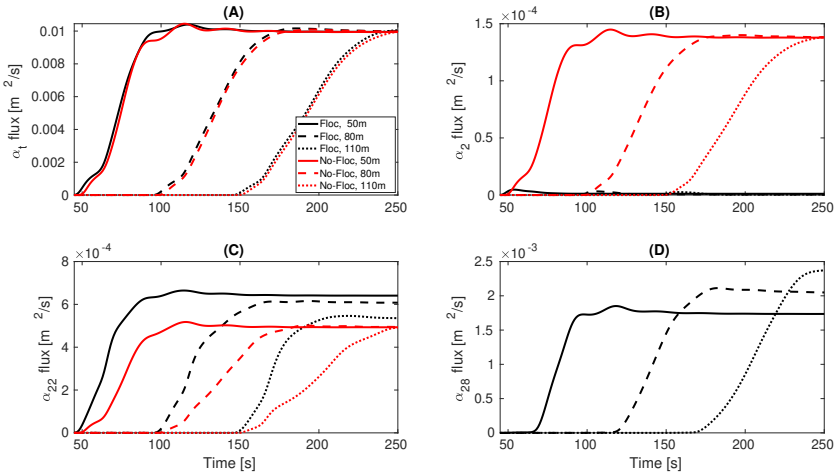

Figure 5.11: Fraction fluxes across the the three x-normal slices, slice1 at 50m, slice2 at 80m and slice3 at 110m. (A) α_t flux, (B) α_2 flux , (C) α_{22} flux , (D) α_{28} flux .

the sediment flux α_t and the fractional fluxes α_2, α_{22} and α_{28} through three cross-sections (yz plane) at 50m, 80m, and 110m, as shown in Figure 5.11. The data is collected from run 1 and 2. The three fractions, α_2, α_{22} and α_{28}, represent particle sizes of $d_2 = 2\mu m$, $d_{22} = 256\mu m$ and $d_{28} = 812.7\mu m$. These fractions are carefully chosen as they represent the smallest and largest particles (d_2, d_{22}) in the initial particle size distribution (PSD), as well as the largest possible aggregate (d_{28}), as illustrated in Figure 5.3.

While there is little variation in the total sediment flux between the two runs, as shown in Figure 5.11 (A), a notable difference can be observed in the fraction fluxes in (B), (C), and (D). In the case of flocculation, the fraction flux (Figure 5.11, B) is significantly lower compared to the no-floc case, primarily due to aggregation processes that cause particles to transition from $k = 2$ to higher-level phases. In contrast, without flocculation, the flux remains constant and unchanging across the cross-sections as there are no aggregation mechanisms in play.

The aggregation process is further confirmed in Figure 5.11 (C), where the steady-state flux decreases in the flocculation scenario from one cross-section to the next, a trend that is not present in the no-flocculation scenario. In the flocculation scenario, as seen in Figure 5.11 (C), the steady-state flux is

23%, 19% and 8% lower in sections 1, 2, and 3, respectively, compared to the no-flocculation scenario, indicating that the particles have transitioned to higher phases in the regions between these sections. The steady-state flux of α_{28} shows an increase from one cross-section to the next, suggesting that lower fractions such as α_{22} have undergone aggregation and progressed to the phase α_{28}. The region behind the PNMT experiences a high shear rate due to its presence, leading to a higher rate of flocculation in cross-section 1 compared to the others. As the PNMT moves away, the particle aggregation rate gradually decreases.

In the case of α_{28}, as shown in Figure 5.11 (D), there is no no-flocculation scenario present throughout the simulation. Nevertheless, the development of the α_{28} flux can be presented to demonstrate that finer phases undergo aggregation, resulting in an increase in the steady-state flux.

5.4.4 Flocculation Effect Visualisation

As the speed of the PNMT is equal to the discharge velocity, the discharged mixture immediately enters the negative buoyancy phase and then impacts the seabed, creating a turbidity current. Since the observed differences between the flocculation and no-flocculation scenarios are related to the sideways turbidity currents, we plot 4 z-normal sections -(xy) plane- for the volumetric concentration of the two runs at BOTTOM boundary and 1m from the bottom boundary and 250s (see Figure 5.12). Moreover, the relative concentration difference is calculated, resulting in the top 2 figures in Figure 5.13. Such that the relative concentration difference is calculated as follows:

$$\alpha_{t,diff} = \frac{\alpha_{t,no-floc} - \alpha_{t,floc}}{\alpha_{t,no-floc}}. \tag{5.23}$$

This would result in a clearer visualization of the differences between the two cases, providing a more comprehensive understanding of the extent to which flocculation affects the behavior of turbidity currents. Furthermore, we plot 2 X-normal figures (bottom figures in Figure 5.13) to clearly visualize the sediment distributions in the sideways turbidity current in both cases.

To explain the results, we must first introduce the structure of a turbidity current resulting from an instantaneous discharge. We consider a current that

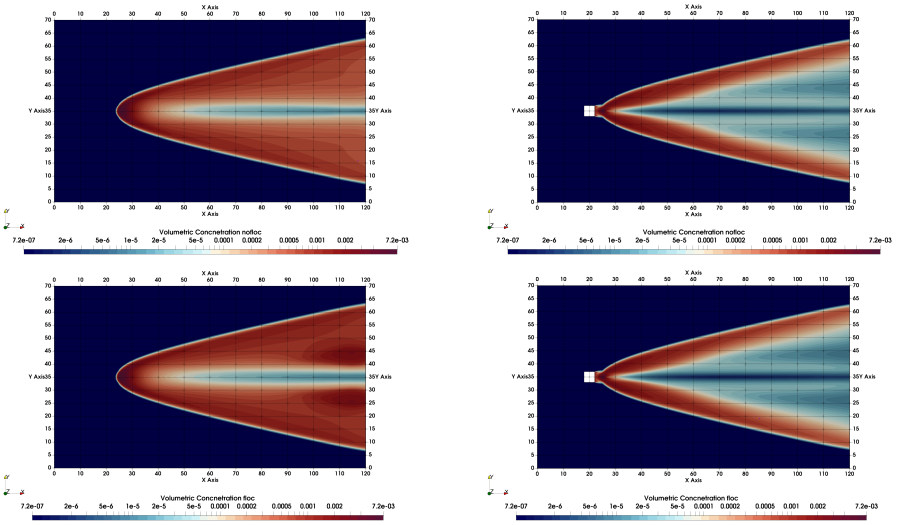

Figure 5.12: Z-normal sections for the flocculation and no flocculation cases are taken at the BOTTOM boundary **(left)** and 1m from the bottom **(right)**. The top row shows the no-flocculation case, while the lower row shows the flocculation case.

propagates to the right and left (along the y-axis) from the PNMT. At the beginning, a head forms and as it propagates, a body begins to appear. Over time, a tail starts to form. These are the three main structural regions of the side-way current, noting that not all sideways current shown herein have this structure.

In the flocculation and no-flocculation scenarios, the dispersion trend remains unchanged and the overall turbidity current forms a wedge shape in both cases. However, from the perspective of sediment distribution, there are significant differences between both cases, indicating that flocculation does have an effect in the near-field region. The regions most affected by flocculation are the head and body of a sideways turbidity current, particularly in cases where the current propagates for longer periods of time and the tail becomes visible. It is important to keep in mind that a sideways turbidity current that has only propagated for a shorter period of time is less likely to exhibit the tail region, which typically forms relatively close to the PNMT.

In the head region, the flocculation case has a higher volumetric concentration than the no-flocculation scenario. In the tail region, especially at section

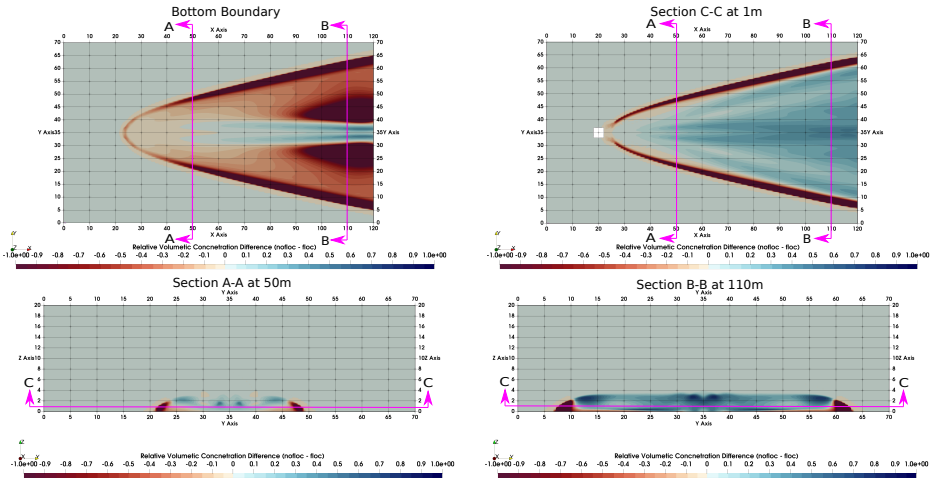

Figure 5.13: Z and X normal sections show the relative differences between the flocculation and no-flocculation cases. The Z-normal sections are taken at the BOTTOM boundary **(left)** and 1m from the bottom **(right)** which is section C-C, while the X-normal sections are taken at 50m and 110m from the INLET boundary.

B-B in Figure 5.13, the flocculation case has the highest sediment distribution in the lower region. There is also a slight flocculation effect in the body region, where in the no-flocculation scenario, the sediment remains in suspension, while the large flocs in the flocculation case have already settled.

These observed differences occur due to the migration of the fine fractions to the coarser fractions, forming new large fractions and enlarging existing ones. The large-formed flocs have relatively high settling velocities. For example, the $u_{kr} = 0.00305$ for a floc size of $d_{28} = 812.7\mu m$ and density of $\rho_{28} = 1018.23kg/m^3$. This has two direct implications on the total sediment distribution: first, the elimination of fine particles with low settling velocities, and second, an increase in the total average settling velocity of the sediment as a whole. In contrast, this does not happen in the no-flocculation scenario, as it is clearly evident in Figure 5.13 that at the top body region, the no-flocculation case has a higher concentration than the flocculation scenario. This is because fine fractions with lower settling velocities are still in suspension. Despite the relatively large settling velocities of the large flocs, they remain in suspension in the head region due to the high mixing in this region.

To conclude,

1. In the near-field region, aggregation between particles is the dominant mechanism, leading to the formation of large particles and the enlargement of existing ones. This results in the elimination of fine particles in the near-field region and generally an increase in the settling velocity of sediment particles.

2. As large particles settle out from the turbidity current, this reduces the concentration of the turbidity current, which subsequently creates an evident tail region of the side-ways current and reduce the amount of the transported sediment to the far-field.

5.4.5 Layer Averaged Parameters

To further understand the impact of flocculation on turbidity currents, we conducted additional analysis focusing on the lateral flow in the region where differences are noted in the previous section (sec. 5.4.4). Thus, we selected a point at 118 m on the X-axis, 100 m away from the front of the PNMT, located in the region where significant differences are observed. Four vertical concentration and velocity profiles, each 5 m in height, are taken along the run-out distance (Y-axis) at 15 m, 20 m, 25 m, and 30 m. The 35 m point is the SYMMETRY boundary and 0 is the SIDE boundary (Figure 5.9). The layer-averaged parameters are calculated using the following equations:

$$Uh = \int_0^{z_\infty} u_y \, dz, \tag{5.24}$$

$$U^2h = \int_0^{z_\infty} u_y^2 \, dz, \tag{5.25}$$

$$UhC = \int_0^{z_\infty} \alpha_t u_y \, dz, \tag{5.26}$$

where $z[m]$ is the upward normal coordinate, h $[m]$ is the height of the current, $U[m/s]$ is the layer-averaged velocity, $C[-]$ is the layer-averaged concentration and $u[m/s]$ is the local velocity and z is the vertical coordinate. Figure 5.14 shows the layer averaged parameters for both the flocculation and no-flocculation scenarios. We also examined the other 4 scenarios, runs 3-6 (Table 5.1), in order to assess the sensitivity of the flocculation parameters.

In general, adjusting flocculation parameters d_f and E_b has a slight effect on the determination of the flocculation process, see the leftmost figures in

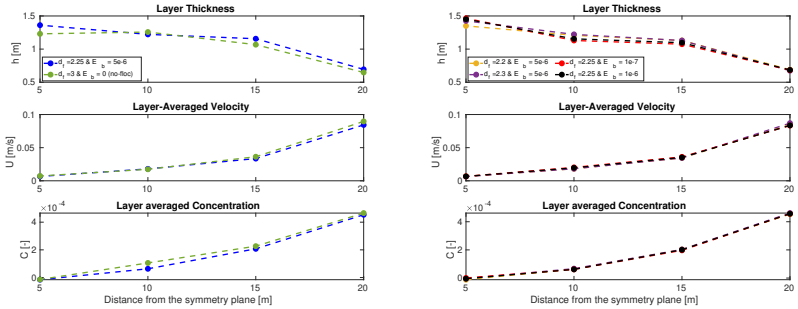

Figure 5.14: Layer-averaged parameters of the sideways turbidity current. The flocculation scenarios are compared on the left, where the fractal dimension d_f and the breakage coefficient E_b are changing. The graphs on the right compare the flocculation scenario and no-flocculation scenario.

Figure 5.14. This, however, does not affect the main comparison between the no-flocculation scenario (Run2) and the flocculation scenario (Run 1), since hardly any differences are observed with respect to layer-averaged velocity and concentration in Runs 3-6, unlike the difference observed between the two cases (Runs 1,2), which can be spotted immediately(right figures in Figure 5.14), implying that only the flocculation process is responsible for the observed differences between Runs 1,2. In other words, changing flocculation parameters at this level of scale, i.e. the near-field region, does not have a major impact on flocculation. We can now proceed with our main investigation: determining the effect of flocculation by comparing Runs 1,2.

In the no-flocculation scenario, the layer-averaged velocity in regions far apart from the middle region is almost 6% higher than in the flocculation scenario. Moreover, while flocculation does occur, the turbidity current has a lower layer-averaged concentration, resulting in a higher layer-averaged thickness in the flocculation scenario than in the no-flocculation scenario. As the current propagates along the run-out distance, particles aggregate and particle size increases, with the freshly formed flocs exhibiting an increased settling velocity. Therefore, in the no-flocculation scenario, sediment particles are still in suspension, providing the current with extra buoyancy force that is not present in the flocculation scenario. It is worth mentioning here that buoyancy force is one of the main driving forces of a turbidity current, which is why differences are observed between the layer-averaged parameters.

5.4.6 Discussion

While flocculation is active and the sideways turbidity current propagates, the current is expected to lose its momentum quickly due to the settling of particles in the body and the tail parts, implying that lower amount of sediment will be available for the passive transport phase, which comes directly after the turbidity current phase. In the passive transport phase, the sediment is transported based on the background current, ambient turbulence and topography (Ouillon et al., 2021). This is more likely to happen in the far-field region. Thus the current work proves that there should be enough attention to optimize the PNMT including the discharge conditions to promote flocculation in the near-field region. Despite the slight effect of the flocculation in the near-field region, we believe according to the insights that are gained from the previous sections that flocculation will definitely plays a major role in the far-field region.

Although the aforementioned results present an understanding of the effects of flocculation in the near-field region, flocculation might be under/overestimated due to the PNMT design considered here, which is simple and does not represent a real PNMT design. We know that the wake region is highly dependent on PNMT geometry and different estimated shear rates will have a different effect on flocculation dynamics. Studying the effect of PNMT geometry on flocculation dynamics can provide unique insights into the most favorable conditions for flocculation in the near-field region. This, in turn, will improve the settling potential of flocs in the near-field regions, which will have a positive effect on the far-field region.

If flocculation results in a low degree of polydispersivity among the sediment within the mixture, it could lead to the current dissipating more quickly, as demonstrated by Harris et al. (2002), who showed that higher levels of polydispersivity can lead to a shorter run-out length compared to a monodisperse current with an equivalent settling velocity. In addition, they found that faster settling particles, or "flocs," contribute to shorter run-out distances. Therefore, considering both the effects of a low degree of polydispersivity and faster settling flocs, a current with flocculation would likely dissipate more quickly than one with no or lower levels of flocculation.

The results of the systematic comparison between flocculation and no-flocculation presented in this chapter suggest that flocculation is likely to

occur in the near-field region immediately following discharge. The aggregation of sediment particles has a limited impact on the behavior of turbidity currents in the near-field, with the flocs within the current showing a high propensity for settling. Our results indicate that flocculation does not significantly affect the behavior of turbidity currents generated by DSM in the near-field region. However, it is expected to have a notable and distinguishable impact in the far-field region.

5.5 Conclusions

This chapter sought to investigate the effect of flocculation in the turbidity flows generated by polymetallic nodule mining. The numerical evaluation demonstrates that sediment readily flocculates to form large particles that will settle as soon as the turbidity current subsides enough to allow this to happen, this process is likely occurring in the far-field region. The flocs are rapidly forming due to the turbulence caused by the PNMT, particularly in the region close to the PNMT. Furthermore, it is evident from the numerical work that the aggregation mechanism is more dominant than the break-up mechanism. The effects of flocculation can be observed in the near-field region, but they are limited to have a significant impact on the turbidity current in the vicinity of the PNMT.

Drift-Flux modelling coupled with the Population Balance Equation serves as an acceptable tool for modeling the hydrodynamics of water-sediment mixtures, which are present in DSM activities. Therefore, different discharge scenarios need to be investigated in order to gain more insight into the effect of flocculation in the near-field region. However, it is crucial to arrive at a proper estimation of the fractal dimension and breakup coefficient first. Moreover, the design of PNMTs may be adapted to foster conditions that are more favorable for flocculation. It is worth noting that turbulence modelling is crucial in flocculation modeling, since the shear rate is directly related to the flocculation source terms. Therefore, better representation of the turbulence in the wake region is recommended, since the buoyant $k - \epsilon$ model still lacks 2 important kinetic energy damping mechanisms: the turbulence flux of momentum in the vertical direction and the extra vertical mixing between the flow layers due to the particles, i.e., the turbulent wake resulting from particle deposition in the vertical direction. It is also important to assess the sensitivity of these

two damping mechanisms on the shear rate, which, in turn, is responsible for the collision/breakage dynamics of the flocs. Using spatial averaging rather than time averaging to estimate turbulence characteristics might help improve the representation of turbulence and therefore flocculation, but the amount of computing power required to do so must be taken into consideration.

With the intention of simplifying our current analysis, we omit the consideration of the front collection process. However, this aspect could play a crucial role in affecting the particle's fate through its effect on the flocculation process, from the moment of collection to the moment of discharge. To enhance the accuracy of our findings, it would be wise to conduct a separate study to estimate the particle size distribution and the primary particle size at the moment of discharge. This would provide a more dependable representation of the results.

Another limitation of our calibration process is the limited availability of detailed experimental data on CCZ sediment. So far, only one study in the literature, (Gillard et al., 2019), has investigated this topic in depth. Therefore, the calibration is based on a single data set and may not be applicable to other studies. In addition, these experimental results did not use in-situ seawater, which is a crucial factor in any flocculation research. To improve the robustness of our method, further calibration should be conducted using additional data sets using in-situ water samples to establish appropriate values for the flocculation parameters.

Chapter 6

The Influence of System Design on the Dispersion and Flocculation of Turbidity Currents

Abstract

The mathematical and numerical models from Chapter 5 are utilized to examine the impact of discharge parameters on dispersion and flocculation. A test matrix is implemented to vary four parameters associated with PNMT operation, namely PNMT forward velocity, ambient velocity velocity, discharge velocity, and initial concentration at discharge. The results demonstrate that increasing PNMT velocity, initial concentration, and ambient current velocity can increase sediment disturbance and enhance flocculation. Conversely, higher discharge velocity can lead to slower flocculation pace and higher turbidity levels in the near-filed region. Maintaining a lower densimetric Froude number ($Fr \lesssim 1$) at discharge and a slower PNMT velocity, with a PNMT velocity / discharge velocity ratio of 1, allows the turbidity current to flow under and even ahead of the PNMT.

During the hydraulic collection process of polymetallic nodules, turbidity flows can occur due to the inevitable mixing of collected sediment particles with water, which are then discharged into the surrounding environment (GSR, 2018; Haalboom et al., 2023). The behavior of the formed turbidity current in the near-field region depends on the discharge conditions, such that this behavior in a given discharge condition can be studied and modeled using numerical methods (see Chapter 5). In the context of polymetallic nodules mining operation, a discharge scenario refers to the specific release conditions of a water-sediment mixture from a PNMT system, such as the rate of discharge, the velocity and direction of the mixture, and the size and composition of the sediment particles being released.

The aim of this chapter is to investigate the influence of different system parameters, such as PNMT velocity, ambient velocity, discharge velocity, and initial concentration at discharge, on the dispersion of turbidity currents and the flocculation process that occurs downstream of the PNMT. By gaining a comprehensive understanding of these effects, it is possible to develop an improved system design for the PNMT. This can be achieved through optimizing the discharge conditions, such as the velocity and concentration, as well as determining the optimum velocity of the PNMT.

Sediment flux is a commonly used criterion for defining a discharge scenario or release condition. It is a measure of the amount of sediment being discharged by the PNMT and can be expressed in units of mass per unit time per unit area. However, it is not the only factor that can affect the behavior of the turbidity current, other parameters, such as the elevation of the discharge device and the velocity of the PNMT, can also significantly impact the dispersion of the sediment particles and the overall behavior of the turbidity current. By considering these factors, discharge condition that minimize potential environmental impacts can be designed for.

As explored in Chapter 5, flocculation can have a significant impact on turbidity currents in the near-field region, but this effect may vary under different discharge conditions. Increasing the concentration of particles in a suspension may enhance the probability of aggregation, while decreasing the concentration of particles may lower the probability of collision and aggregation, resulting in a reduced likelihood of flocculation. Additionally, changes in other parameters such as discharge velocity, PNMT velocity, and ambient current velocity can increase the shear rate and alter the fate of

particles. This chapter will delve into these effects in greater detail.

To the best of our knowledge, only two studies have specifically addressed the importance of discharge conditions design in DSM operations. These studies have highlighted the need for careful design of the discharge, as follows:

1. One study was specifically focused on studying the effect of discharge scenarios on the dispersion of turbidity flows (Decrop & Wachter, 2019);

2. The other study was more broadly focused on providing a fundamental understanding of the anatomy of the turbidity current formed behind the PNMT (Ouillon et al., 2021).

Before conducting our own investigation into the impact of discharge condition on the behavior of turbidity currents, it is important to briefly summarize the findings of the previous studies on this topic. Decrop and Wachter (2019) used detailed two-phase mixture model to study the behavior of turbidity flows in the near-field region, where different discharge scenarios were tested. As part of their investigation, they used real-case discharge scenarios as input to their model in order to study the behavior of the resulting turbidity currents. Seven different discharge scenarios, in which the concentration, PNMT velocity, and ambient current velocity were varied in order to produce various sediment fluxes for each case. The results show that high PNMT velocitys and high sediment fluxes can lead to the formation of thick and dense turbidity currents. The results also indicate that low discharge velocities can result in lower mixing of the discharged turbidity current with the surrounding environment. Their findings emphasize the importance of studying the effect of discharge scenarios on the dispersion the turbidity current.

The second study that has addressed the importance of discharge design in polymetallic nodules mining was reported by Ouillon et al. (2021). This study used DNS (direct numerical simulation) to investigate the behavior of a turbidity current discharged from a moving source. The DNS approach allowed for a detailed and accurate prediction of the mixture, providing fundamental understanding into the anatomy of the generated turbidity current. They considered several discharge scenarios, including one in which the PNMT was stationary and discharged mixture at the same time. One of the key investigations in this study is the behavior of sideways propagating turbidity

currents, which were found to have similar properties to those observed in lock-exchange tanks (Chapter4).

Although those studies provide meaningful insights into the behavior of turbid flows in the near-field region, they have not considered the effect of particle size and the settling velocity. Both studies only use one particle size fraction, meaning that the propagation of sediment particles inside the turbidity current in the near-field region is only described by one settling velocity. As a result, the dynamics of aggregation and break-up are not modelled. The results gained from the previous chapters give us confidence in the importance of describing such sediment particle dynamics in numerical models. In this chapter, we first introduce the numerical model used in this study in Section 6.1. Subsequently, in Section 6.2, we present our investigation of the steady-state situation. We then proceed to compare the results from different runs in Section 6.3. In Section 6.4, we discuss the insights gained from the results. Finally, we draw conclusions and provide recommendations in Section 6.5.

6.1 Numerical Model

The numerical model and the computational mesh (Figure 5.9) that were reported in Chapter 5 (Drift flux and PBE) are used again to investigate the proposed discharge scenarios in Table 6.1. The same PSD (Figure 5.3), boundary conditions (Table 5.2) and flocculation characteristics (Table 5.1) of Run 1 in Chapter 5 are used herein. The initial concentration, discharge velocity, PNMT velocity and ambient current velocity are changed according to each numerical run.

In Table 6.1, we explore various system design options using an in-situ CCZ PSD as input. These scenarios include the study of flocculation hydrodynamics and aim to evaluate the impact of different parameters, such as PNMT velocity, discharge velocity, initial concentration, and ambient current velocity on the behavior of the resulting turbidity current. It is important to note the following factors:

1. The discharge velocity and PNMT velocity have opposite directions. The ambient current velocity is in the same direction as the discharge;

Table 6.1: Test matrix showing various discharge scenarios from a PNMT.

Runs	Volumetric Concentration[%]	Mixture Density[kg/m^3]	PNMT Velotiy[m/s]	Discharge Velocity [m/s]	Ambient Current Velocity [m/s]	Densimetric Froude Number (Fr_d)[-]	Velocity Ratio r[-]	Volumetric Sediment Flux[m^2/s]
1	1	1016.5	0.5	0.5	0.1	1.75	1	0.01
2	1	1016.5	0.5	0.75	0.1	2.63	0.66	0.015
3	1	1016.5	0.25	0.5	0.1	1.75	0.5	0.01
4	1	1016.5	0.25	0.25	0.1	0.87	1	0.005
5	1	1016.5	0.25	0.75	0.1	2.63	0.33	0.015
6	1	1016.5	0.5	0.5	0.05	1.75	1	0.01
7	0.5	1008.25	0.5	0.5	0.1	2.48	1	0.005
8	0.5	1008.25	0.25	0.25	0.1	1.24	1	0.0025
9	0.5	1008.25	0.25	0.75	0.1	3.72	0.33	0.0075
10	1.5	1024.75	0.5	0.5	0.1	1.44	1	0.015
11	1.5	1024.75	0.25	0.25	0.1	0.72	1	0.0075

2. The densimetric Froude number can be calculated as follows:

$$Fr = \frac{u}{\sqrt{g' \times h}}. \tag{6.1}$$

   Here, u represents the discharge velocity, and g' is the relative density difference between the mixture and ambient fluid, which can be calculated as $g \times \frac{\rho_m - \rho_l}{\rho_m}$, where ρ_m and ρ_l denotes to the mixture and the water densities, respectively. The characteristic length scale, denoted by h, is set to 0.5 m, which is the length of the vertical side of the discharge device;

3. The velocity ratio r is defined as the ratio of the PNMT velocity to the discharge velocity, expressed as $r =$ PNMT velocity/discharge velocity;

4. The volumetric sediment flux is the quantity of sediment released from the discharge device per unit area and unit time, calculated using the following equation: $S_f = \alpha_t \times u \times A$, where α_t is the sediment concentration, and $A = 1m^2$ is the cross-sectional area of the discharge device.

The numerical simulations were performed on the Delft Blue supercomputer ((DHPC), 2022) to generate a duration of 250 seconds. The average runtime for a single simulation using 64 nodes was approximately six days. However, some simulations, such as runs 4 and 11, required nearly three weeks of computation time on 64 nodes. It is noteworthy that increasing the number of nodes did not significantly reduce the computation time for each run.

6.2 Steady State in the PNMT Reference Frame

When it comes to comparing the results of the numerical runs, it is critical to conduct the analysis during a steady-state condition of the compared runs. This is to guarantee a fair comparison between the outcomes and the different dispersion shapes produced by the tested parameters.

During the initial analysis of the results, it was found that two particular locations, located at 35m and 70m in the x direction and away from the INLET boundary (as shown in Figure 5.9), were crucial in determining the steady-state condition. These locations were identified through a trial-and-error

process, whereby the first location where the steady-state could be achieved was selected. To ensure a steady-state condition, sediment flux was used as the evaluation criterion. The analysis focused on two x-normal sections, one for each group of runs. The first group included Runs 1, 2, 3, 5, 6, 7, 9, and 10, while the second group comprised Runs 4, 8, and 11. Upon analyzing the results further, it is concluded that special attention is required for Runs 4 and 11, as they did not reach a steady state close to the PNMT (will be discussed in Subsection 6.3.4), unlike the other group which achieved a relatively more distant steady-state location (see Figure 6.1). Nevertheless, Runs 3 and 5 are also close to achieving the steady-state condition, albeit with a slight delay. Given the computational expenses involved, we have deemed this delay acceptable and consider these runs to be nearly in steady-state.

At the specified locations (35m and 70m in the x direction and away from the INLET boundary), an xz section is taken, and the volumetric sediment flux is calculated for those sections. The calculation of sediment flux is simple, involving the multiplication of sediment velocity in the x-direction (Ux), section area (A), and the total sediment concentration (α_t). The formula for sediment flux is $S_f = \alpha_t \times U_x * A$. A steady state is considered to have been achieved when the sediment flux remains constant within the selected section, indicating no change in the sediment flux over time. Therefore, two figures, A and B, are presented in Figure 6.1 to depict the first group at 70 meters and the second group at 35 meters, respectively. Since the time scale of the flocculation process is crucial, meaning that the particles take some time until they aggregate/breakup together, it is essential to have a consistent time reference for all the runs which is 250 seconds to ensure fair comparisons. It's worth mentioning that if a Run has achieved the steady state condition at the 70m location, it automatically implies that it has also achieved the steady state at the 35m.

6.3 Comparison of the Results

We take into account the variation of different controlling parameters while designing the test matrix in Table 6.1. Thus in the following subsections we study the effect of the following parameters:

1. PNMT forward velocity;

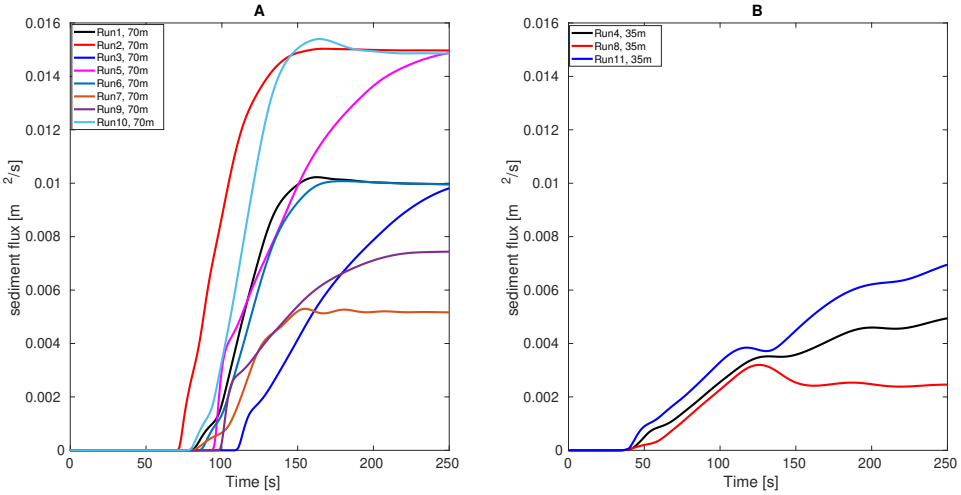

Figure 6.1: Steady state analysis of two distinct groups of runs at different locations: 35m **A** and 70m **B**.

2. Ambient current velocity;

3. Discharge velocity;

4. Initial concentration.

For all runs, we plot the bottom boundary or 1 cm above the bottom at 250s in order to compare the dispersion of the turbidity current in the near-field region.

6.3.1 PNMT Forward velocity

For the same sediment flux, the PNMT forward velocity has a significant impact on the shape of the turbidity current and the shear rate in the near-field region.

Visualization

The top two figures, A and B in Figures 6.2 illustrate the dispersion shape of the turbidity current in the near-field region for Runs 1 and 3. The bottom two figures, C and D, show the shear rate field associated Runs 1 and 3. The dispersion shape is defined here as the shape that the turbidity current forms in the near-field region. In Run 1 and 3, the PNMT drives with a forward velocity of 0.5 m/s. Figure 6.3 has similar structure except for Runs 3 and 5, in which the PNMT drives with a forward velocity of 0.25 m/s. Note that Run 1 and 3 are equal in terms of discharged sediment flux, as are Run 2 and 5.

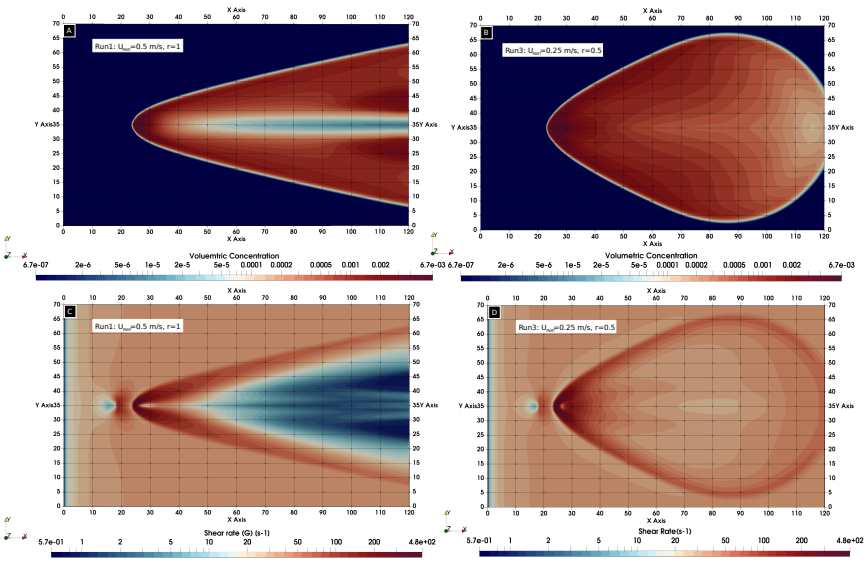

Figure 6.2: The impact of PNMT Forward velocity on volumetric concentration and shear rate for Runs 1 and 3. The figures present Z-normal sections at a distance of 1 cm from the bottom.

In order to explain the results, we must first introduce the following turbidity current structure. Let us consider a sideways propagating current resulting from an instantaneous discharge. The current propagates to the right and left (along the y-axis) after the impingement region, where the head forms at the beginning and the body begins to appear as it propagates. Over time, the tail starts to form. These are the three main structural regions of the sideways

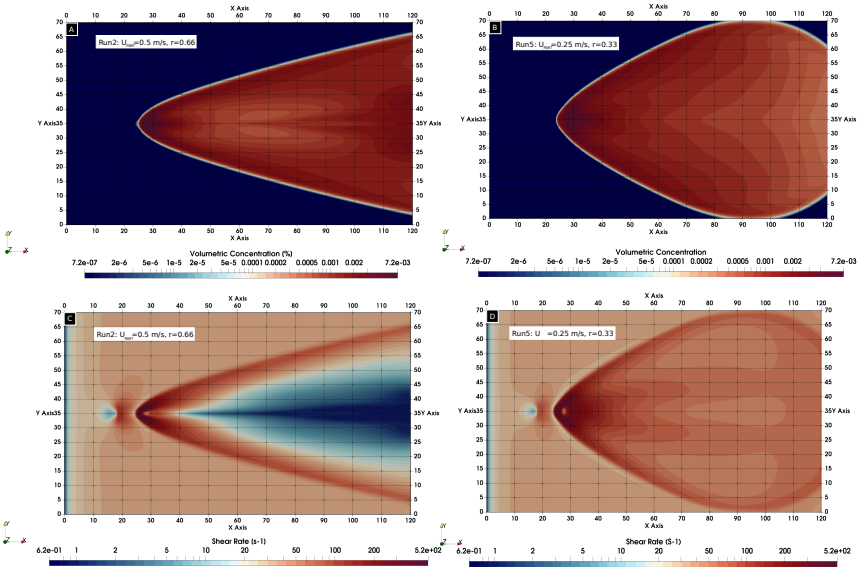

Figure 6.3: The impact of PNMT Forward velocity on volumetric concentration and shear rate for Runs 2 and 5. The figures present Z-normal sections at a distance of 1 cm from the bottom.

propagating current. We will use these definitions in the following context. Figure 6.4, A, shows the structure of the sideways turbidity current

When the PNMT forward velocity is high, the turbidity current disperses in a smaller angle compared to the larger angle generated by PNMT with lower forward velocity, as shown in Figures A and B in 6.2 and 6.3. The difference in dispersion angle is due to the difference in distance achieved in both cases (slow and fast) because of the fixed time of 250 seconds. Specifically, the slower run covered a distance of 62.5 meters while the faster run covered 125 meters, resulting in the observed differences.

There is a significant difference between the sideways propagating currents of both cases. In the case of high PNMT velocity, the sideways propagating current begins to have a concentration gradient along its structure, with high concentration at the head region and lower concentration at the tail region (Figure 6.4). This is because the supply of sediment for each sideways propagating current from the PNMT decreases quickly over time as the PNMT is moving through the area at a high velocity (Figure 6.4, panels A and C).

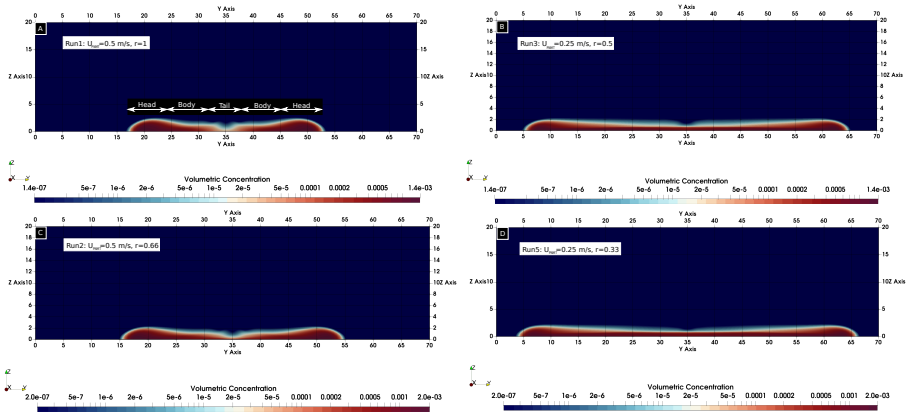

Figure 6.4: Examining the influence of PNMT forward velocity on sideways-propagating turbidity currents in Runs 1, 2, 3, and 5. An YZ plane section captured at the Steady State Location of 70m from the INLET Boundaries. Example of the Sideways-Propagating Turbidity Current Shown in Panel A

In contrast to the PNMT that is driven slowly, the sideways propagating current has a sediment supply for double the time, which explains why the concentration along its structure decreases slightly from the head to the tail. Due to the lower forward velocitys, the tail region is not yet apparent in the current cases. The sideways propagating currents are currently limited to head and body regions, as depicted in Figure 6.4 panels B and D.

The velocity of the PNMT has a significant impact on the resulting shear rate. At high PNMT velocity, the shear rate in the central region is lower than that of the low PNMT velocity, indicating that the central region is still in a high-mixing condition even at lower PNMT velocitys. Conversely, the head region at high PNMT velocity exhibits a higher shear rate, as expected due to the increased turbulence resulting from high PNMT velocity. Moreover, the sediment distribution in the central region is higher at low PNMT velocity compared to high PNMT velocity, resulting in a well-formed tail with a lower concentration distribution. Consequently, buoyancy forces in the central region are lower at high PNMT velocity, leading to reduced mixing and lower shear rate. Conversely, when there is a high concentration of suspended sediment in the central region, buoyancy forces are higher, leading to increased mixing

and relatively high shear rate, especially at low PNMT velocity. Furthermore, it is noteworthy that the overall shear rate increases slightly as the PNMT velocity increases, with a 20-40 s^{-1} increase in the entire domain from lower to higher PNMT velocities.

Analysis of the Sideways Propagating Turbidity Current

To gain a better understanding of the mixture dynamics in the near-field, we examine the results of two groups of runs - (1,3) and (2,5). Runs 1 and 2 have a PNMT velocity of 0.5 m/s, while Runs 3 and 5 have a PNMT velocity of 0.25 m/s. Our previous analysis of the steady state case (see fig. 6.1) revealed that the four runs attain a steady state with the PNMT reference frame located at 70m in the X direction. Thus, we compare the normalized volumetric sediment flux and the normalised largest fraction α_{28} at the 4m profile, situated where the X direction intersects with 70m and Y direction intersects with 25m, see fig 6.5. Normalization involves dividing the volumetric sediment flux $[m^2/s]$ and α_{28} $[m^2/s]$ by the volumetric sediment flux at discharge $[m^3/s]$, resulting in a normalised voluemtric sediment flux $[m^{-1}]$ and a normalized α_{28} flux $[m^{-1}]$.

A comparison of the two groups of runs reveals a clear trend: a PNMT with higher forward velocity generally produces more volumetric sediment flux than a PNMT with lower forward velocity. This is also observed by the higher flux of the largest fraction in the case of high PNMT forward velocity, indicating a faster pace of flocculation. This is shown in Figure 6.6. The results demonstrate that the sideways propagating turbidity current is relatively faster and the amount of sediment is slightly higher for a PNMT with higher forward velocity. Moreover, it's worth noting that a higher PNMT velocity leads to an increase in the quantity of the largest sediment fractions, indicating a faster formation of larger flocs. However, it's important to consider the time required for both slow and fast PNMT velocitys to reach steady state. Although the turbidity current has reached a steady state at this location, it doesn't necessarily imply that the flocculation process has also reached a steady state and the aggregation process may still be ongoing. Thus, the amount of sediment transported to the far field could be higher with high PNMT velocity. As the shear rate is relatively higher at the head of a PNMT with higher velocity, the rate of flocculation also increases, enabling

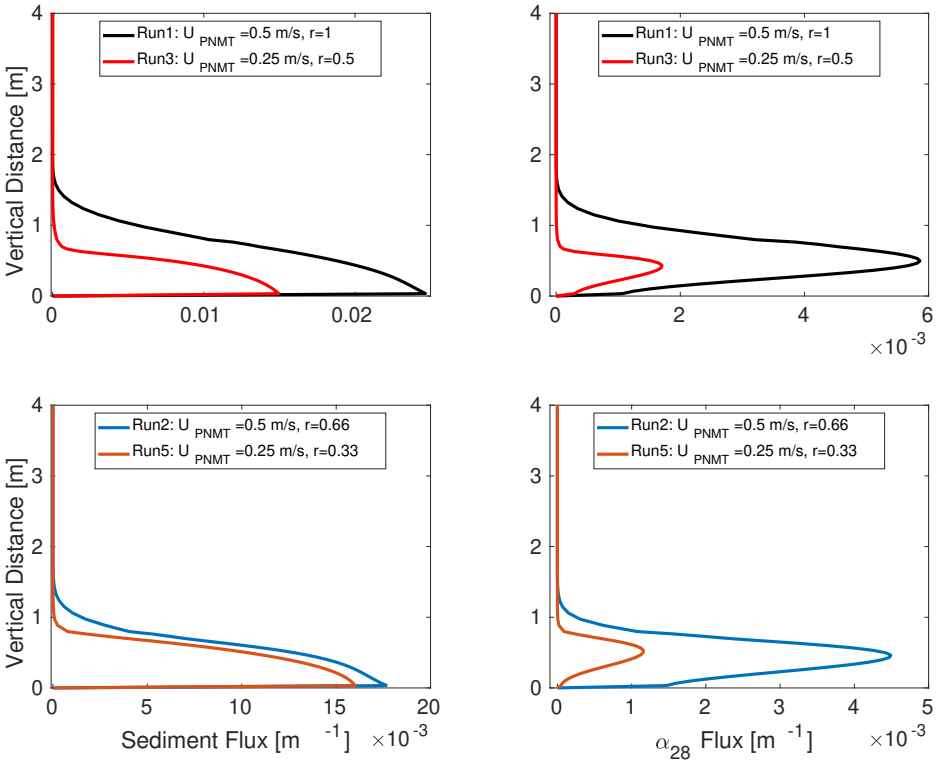

Figure 6.5: Normalised total sediment flux (**left**) and normalised largest fraction flux, α_{28} (**right**). A 4m profile at 70m in X and 25m in Y direction is taken to examine the side way turbidity current.

the largest fraction to form more quickly. Additionally, the higher PNMT velocity leads to increased sideways propagating turbidity current velocity and greater thickness, particularly at the head.

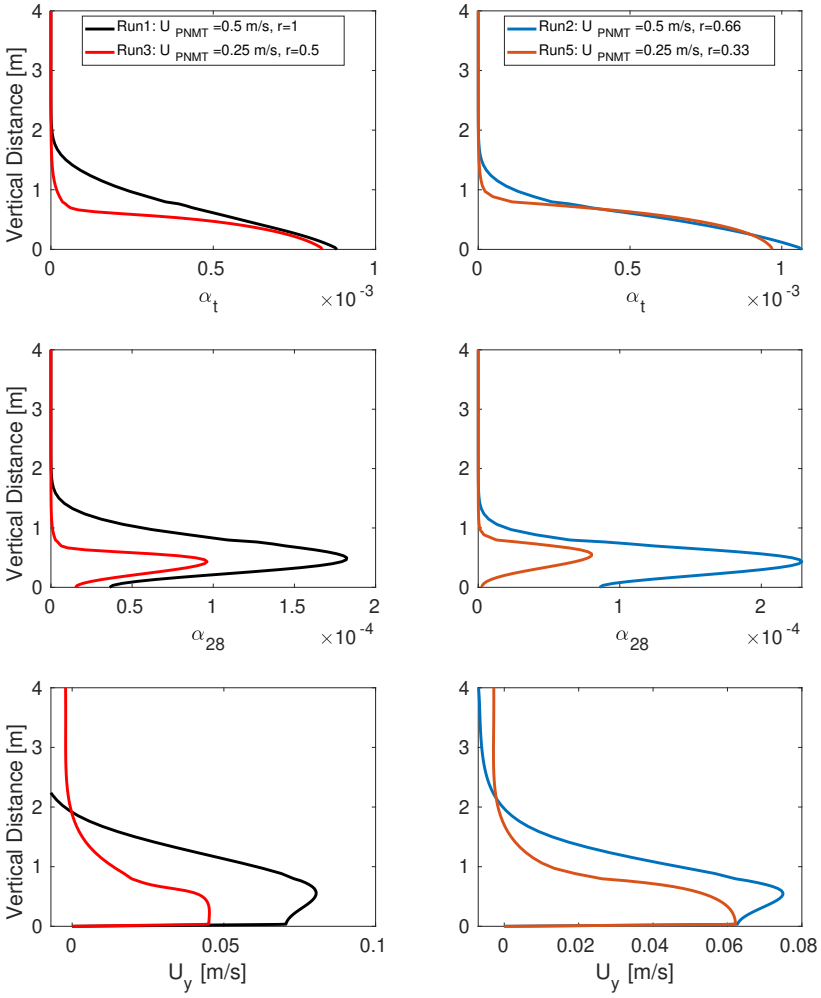

Figure 6.6: Comparing total Sediment, largest Fraction (α_{28}), and side-way Velocity (y direction) in Runs 1 3 (**left**) and Runs 2 5 (**right**). A 4m profile at 70m in X and 25m in Y direction is taken to examine the side way turbidity current.

6.3.2 Ambient Current

The background ambient current plays a significant role in the amount of sediment transported to the far-field region, making it an essential parameter to investigate. We compare two runs, 1 and 6, in which the only varying factor is the velocity value of the current, to examine its impact.

Visualization

To examine the ambient velocity impact, we subtract the results of two runs from each other, since there is no change in the dispersion shape of the current as follows:

$$\alpha_{t,diff} = \alpha_{t,Run1} - \alpha_{t,Run6}. \tag{6.2}$$

In Figure 6.7, we show 2 z-normal sections that represent the $\alpha_{t,diff}$ field at 1 cm and 100 cm above the bed at left and right, respectively.

Although both cases exhibit a wedge-shaped dispersion, there are three regions where significant differences in the total sediment distribution, largest fractions distribution, and shear rate are observed between them, in the following regions:

1. The head of the sideways propagating current (the edges of the wedge),
2. The body of the sideways propagating current especially in the region that lies between 40m-120m longitudinal lines,
3. The tail of the sideways propagating current especially in the region that lies between 100m-120m longitudinal lines).

It is clear that the background current affects the propagation of the current. In Figure 6.7, there is a negative difference at the head of the sideways propagating turbidity current, while the difference is positive at the body and the tail. To investigate this difference, we compare the fractions field between the two runs. The total concentration of Run 1 is lower than that of Run6 at the top-layer head region. In contrast, in the body and tail region, the total concentration of Run 1 is higher than that of Run6. Furthermore, we also plot the shear rate difference in the bottom figures at 1 cm and 100 cm from the

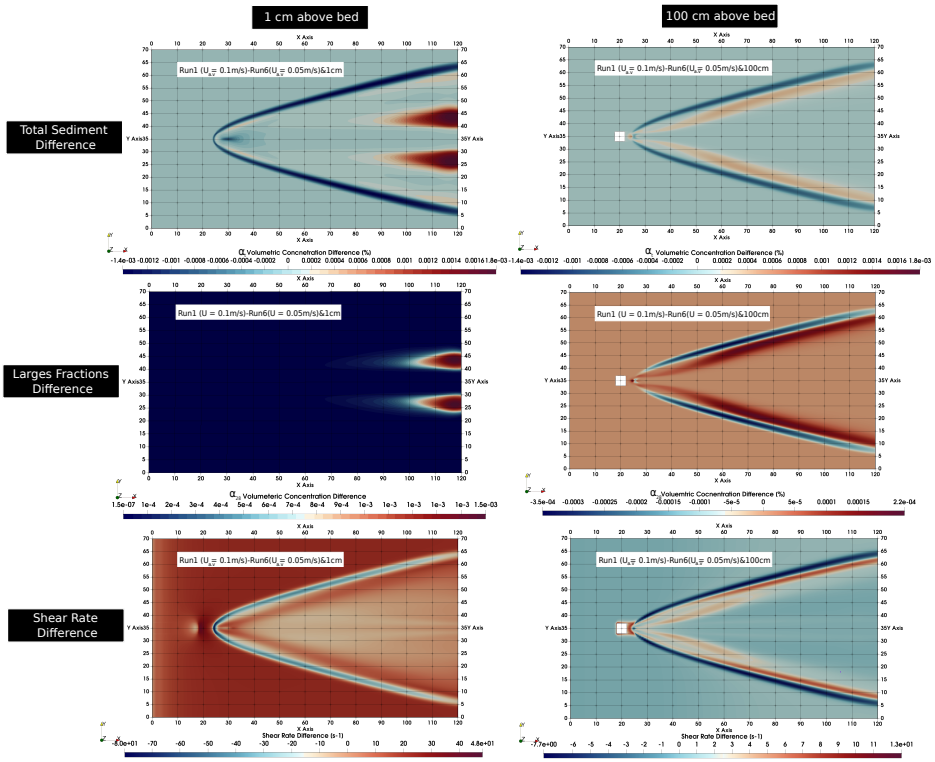

Figure 6.7: The volumetric concentration and shear rate are shown at two depths, 1 cm and 100 cm from the bottom, in the left and right columns, respectively. The top two figures show the difference in the total volumetric concentration ($\alpha_{t,diff}$), the middle two figures show the difference in the volumetric concentration of the largest flocs $\alpha_{28,diff}$, and the bottom two figures show the difference in the shear rate of the largest flocs. The $U_{a.v}$ is the ambient velocity.

bottom. The shear rate follows a similar trend, where in the head region, it is higher for lower ambient current velocitys than for higher ambient current velocitys.

The numerical results show that the ambient background current affects the nature of flocculation in the near-field region. As the velocity of the ambient current increases, the shear rate of the flow in the wake region also increases, resulting in an evident increase in the pace of flocculation in the case of a high ambient background current velocity. This results in an increase in settling potential, where the flocs that form at the body region eventually settle in the tail region.

In general, in the wake region, the shear rate is higher by nearly 20-30 s^{-1} for high velocity ambient currents. However, in the head region, the shear rate is lower in this case compared to lower velocity ambient currents. The difference in shear rate between the two regions is higher in the bottom region (20-40 s^{-1}) than in the top region (5-7 s^{-1}). It could be because of the effect of flocculation. In the case of higher ambient current velocity, the large flocs that form tend to settle, affecting the mixing at the head region due to the decreased buoyancy forces. This, in turn, affects the shear rate at the head region.

Analysis of Sideways Propagating Turbidity Current

In Figure 6.8, we plot the normalized sediment flux, total sediment distribution, largest fraction distribution (α_{28}), and lateral velocity at the the steady state location specified earlier in Figure 6.1. The results clearly demonstrate that high ambient velocity leads to increased sediment flux, higher total sediment distribution, and a larger α_{28} distribution. This suggests that flocculation occurs at a faster rate under conditions of high ambient velocity.

These findings are consistent with those presented in Figure 6.7, where the left-middle panel shows a greater abundance of larger flocs under high ambient velocity conditions. The figure also indicates that the shear rate is slightly elevated in the body regions of the current at high ambient velocity, which may contribute to the rapid formation of flocs. Nevertheless, despite the faster pace of flocculation under conditions of high ambient velocity, a higher sediment flux, in general, is still transported by the sideways propagating

turbidity current.

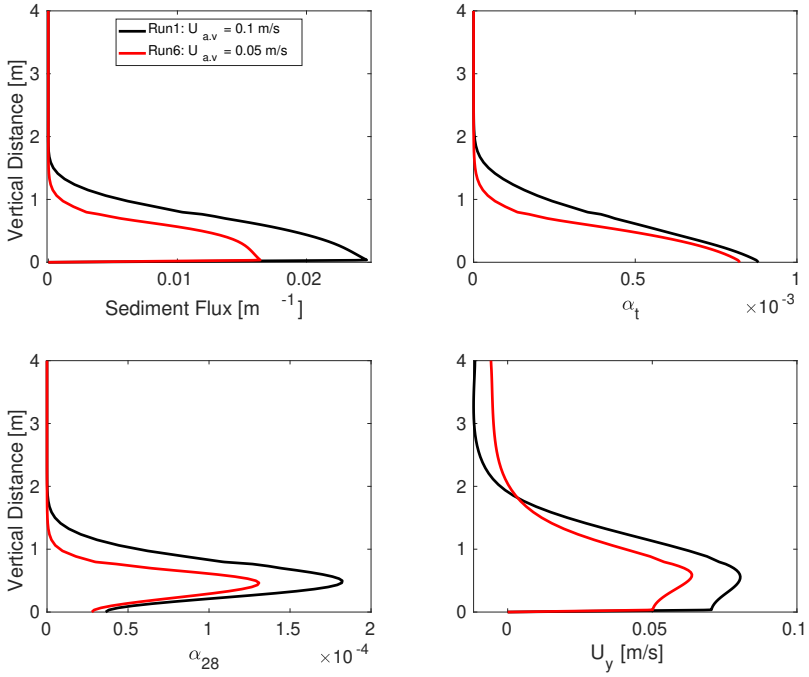

Figure 6.8: Comparing normalised total Sediment flux, total sediment distribution, largest Fraction (α_{28}), and side-way Velocity (y direction) in Runs 1 and 6. A 4m profile at 70m in X and 25m in Y direction is taken to examine the side way turbidity current. The $U_{a.v}$ is the ambient velocity.

Table 6.2: Summary of group comparisons: runs and associated discharge velocity

Runs	1	2	3	5	8	9
Velocity $[m/s]$	0.5	0.75	0.5	0.75	0.25	0.75

6.3.3 Discharge Velocity

Discharge velocity is one of the most important parameters in any PNMT design, as it can be controlled by the manufacturer, unlike other parameters that have a lot of uncertainties (e.g. the ambient background current). In this regard, we present three case studies, where we compare Runs 1 and 2, Runs 3 and 5, and Runs 8 and 9. In each case study, the two runs have the same initial conditions, except for a different discharge velocity. Runs 1 and 2 have discharge velocities of 0.5 m/s and 0.75 m/s, respectively, which is the same for Runs 3 and 5. Runs 8 and 9 have discharge velocities of 0.25 m/s and 0.75 m/s, respectively (Table 6.2).

Visualization

When all other initial parameters are constant, the dispersion shape of the turbidity current in the near-field region hardly changes as the discharge velocity increases or decreases. In Figure 6.9, we plot the total volumetric concentration difference ($\alpha_{t,diff}$) between the two runs of each case study, together with the shear-rate difference.

It is immediately apparent that in the case of a high discharge velocity, the concentration in the near-field region is higher compared to a lower discharge velocity, especially in the head region. Our analysis revealed that, in case of high discharge velocity, the sideways propagating turbidity current is ahead of that at lower discharge velocities, causing the observed positive difference in the head of the turbidity current. As the discharge velocity increases, the transported sediment flux increases. In case of a high discharge velocity, it is more likely that the mixture will be in the jet phase, resulting in a longer jet length. In contrast, in the case of a lower discharge velocity, it is more likely that the mixture will quickly transition to the plume phase. The difference in the impingement region position between the high and low discharge velocity cases results in a negative difference observed near the PNMT. This change in impingement region position could explain why the turbidity current in the

high discharge velocity cases is ahead of that in the low discharge velocity cases.

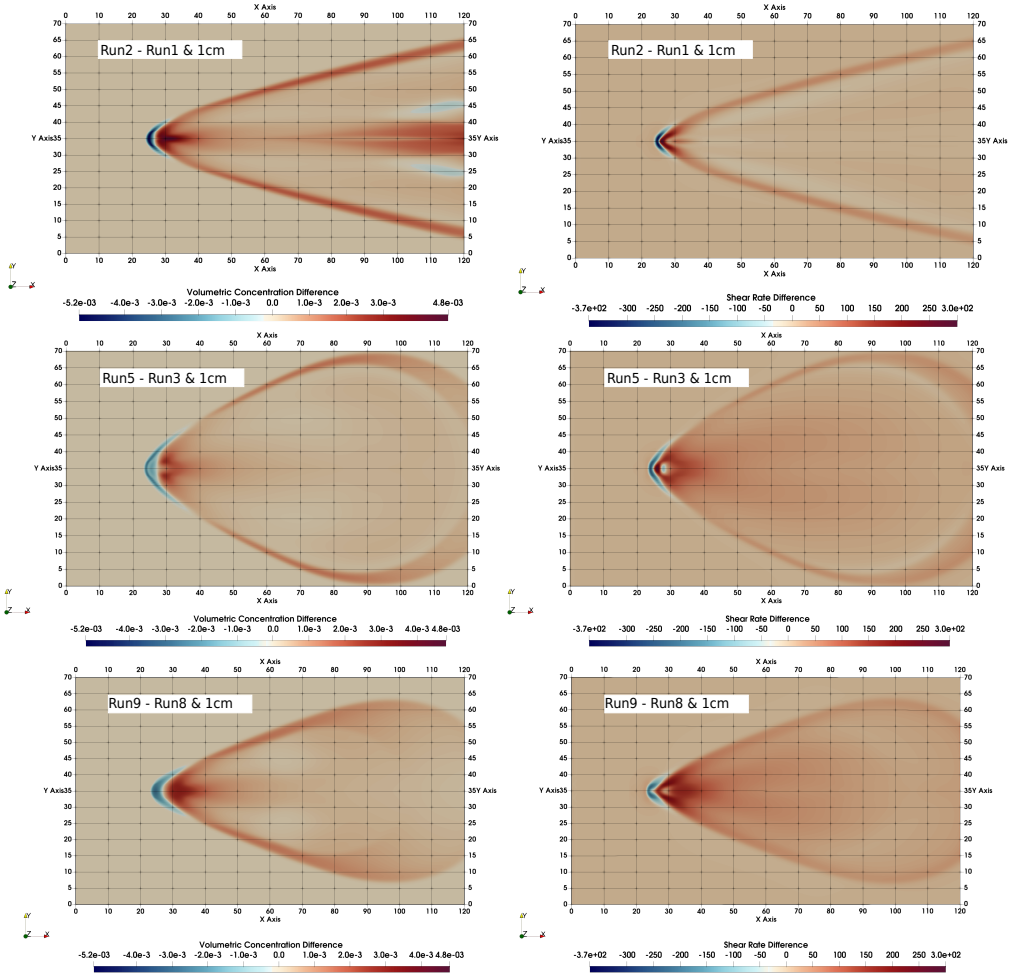

Figure 6.9: The effects of discharge velocity on volumetric concentration and shear rate differences are compared at a distance of 1cm. Runs 1 and 2, and Runs 3 and 5, have the same discharge velocities of 0.5 m/s and 0.75 m/s, respectively. In contrast, Runs 8 and 9 have lower and higher discharge velocities of 0.25 m/s and 0.75 m/s, respectively.

The discharge velocity affects the shear rate because the amount of sediment flux increases with higher discharge velocities. However, the observed shear rate difference varies between the three case studies, with Runs 2 and 1

showing the low difference, followed by Runs 9 and 8 with a slightly higher difference, and the highest difference observed in Runs 3 and 5. One possible explanation for this difference is PNMT velocity / discharge velocity ratio, with a lower difference in this ratio potentially leading to a higher difference in the observed shear-rate.

Analysis of the Sideways Propagating Turbidity Current

To evaluate the impact of changing turbidity current on the sideways propagating turbidity current, we have generated Figures 6.10 and 6.11. These figures demonstrate the sediment flux, largest floc fluxes, total sediment distribution, and side-way velocity. Note that all profiles are captured at a distance of 70m in the X direction and 25m in the Y direction, except for Runs 8 and 9, where a 4m profile is taken at 35m in the X direction and 30m in the Y direction. The profile location for Runs 8 and 9 is chosen specifically to ensure that the measurements are in the body region, after the current had passed.

In general, a higher discharge velocity results in a larger sediment flux and total sediment distribution, with the exception of Runs 1 and 2. Run 1 has a slightly higher sediment flux than Run 2. It is evident from Figure 6.6 that Run 1 has a higher sideways propagating turbidity current velocity. Furthermore, the α_{28} flux is higher at lower discharge velocities, indicating faster flocculation. Generally, the sideways propagating turbidity current is slightly higher at higher discharge velocities, except in the cases of Runs 1 and 2.

It is possible that the deviation of Runs 1 and 2 from the observed trend is due to the forward velocity of the PNMT, which may have affected the behavior of the turbidity current in these cases. Notably, these runs have a forward velocity of 0.5 m/s, whereas the other two groups have a PNMT velocity of 0.25 m/s. It is possible that as the forward velocity of the PNMT increases and the ratio velocity decreases, the sideways propagating turbidity current also increases. However, to validate this hypothesis, additional numerical runs are necessary. By exploring this further, we can gain a more comprehensive understanding of the relationship between the discharge velocity and sediment flux, and the role that the forward velocity of the PNMT may play in this relationship.

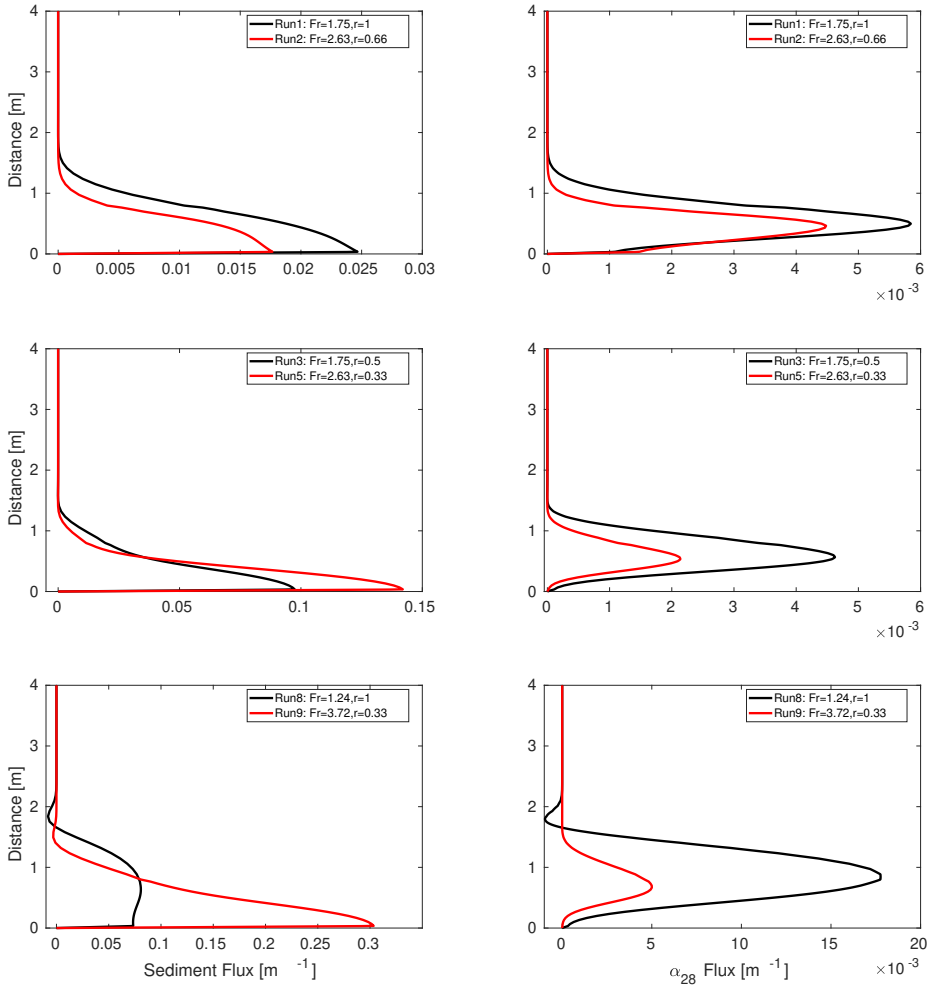

Figure 6.10: The normalised sediment flux **(left)** and the normalised largest fraction flux **(right)** for groups of runs of (1,2), (3,5), (8,9).. For Runs 8 and 9, the 4m profile is captured at the intersection of 35 in the X direction and 30 in the Y direction

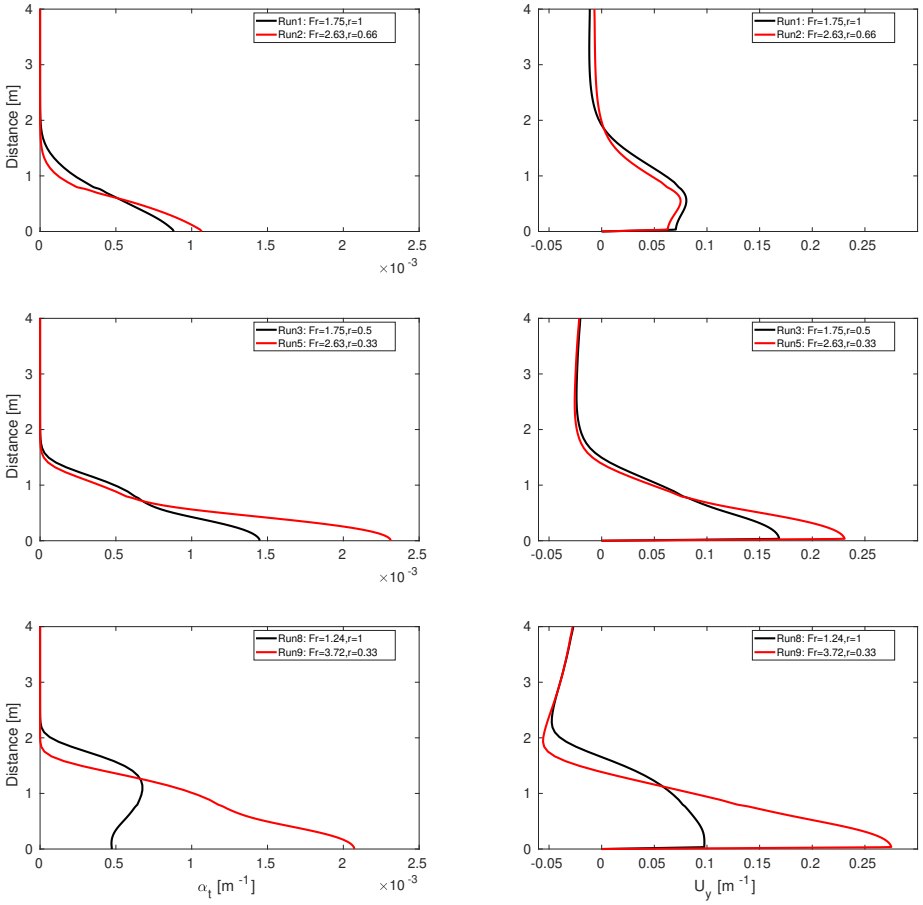

Figure 6.11: The total volumetric concentration **(left)** and velocity profiles **(right)** for group of runs of (1,2), (3,5), (8,9). For Runs 8 and 9, the 4m profile is captured at the intersection of 35 in the X direction and 30 in the Y direction.

6.3.4 Initial Concentration

The initial concentration is defined as the concentration of solid particles at the moment of release from the PNMT. The initial concentration is also one of the parameters that can be influenced and designed by manufacturers. Therefore, we investigated two case studies representing three initial concentrations of 0.5%, 1%, and 1.5% for Runs 7, 1, and 10, and Runs 4, 8, 11, respectively. Keep in mind that the discharge device size remains constant, while the amount of sediment is increased.

Visualisation

Figures 6.12 and 6.13 show the effect of increasing the initial concentration on the development of the turbidity current. In the case of a high initial concentration, the sideways propagating current has a high amount of suspended sediment and a high forward velocity. In contrast, in the case of a lower initial concentration, the run-out distance of a sideways propagating current is low. In the tail region (the region between 100m-120m longitudinal lines), there is an increase in the total volumetric concentration as the initial concentration increases. When the initial concentration is high, there are more sediment particles available for collision, which leads to faster flocculation and a higher settling potential for the resulting flocs. However, in the near-field region, a lower initial concentration is more favorable. This can be achieved by increasing the water entrainment in the mixture prior to discharge.

An increase in initial concentration also leads to an increase in the shear rate. This is due to the higher sediment flux and the corresponding increase in buoyancy forces, which cause more mixing, especially in the head region, resulting in higher shear rates. Furthermore, changes in the PNMT forward velocity, initial concentration, and discharge velocity can also affect the dispersion shape.

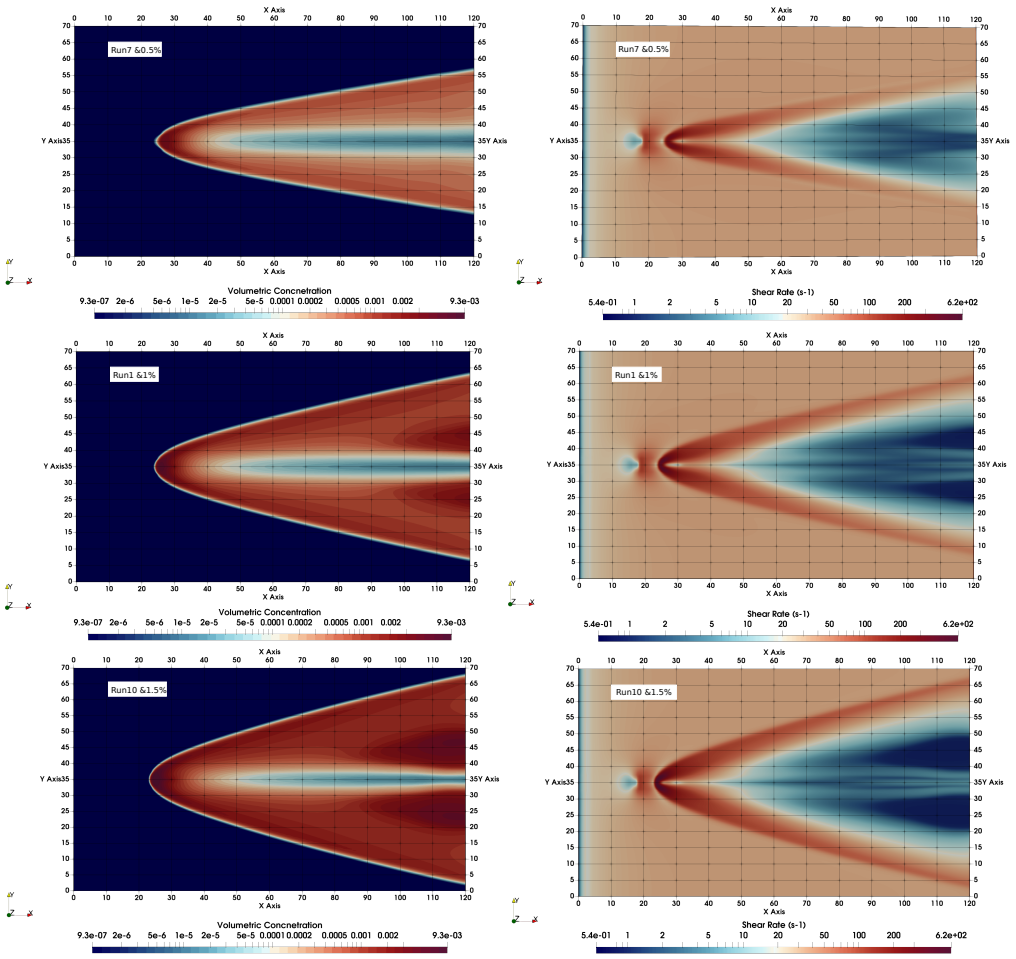

Figure 6.12: The volumetric concentration field and shear rates for Runs 7, 1, and 10 on the left and right are shown here. In these runs, the PNMT forward velocity is 0.5 m/s.

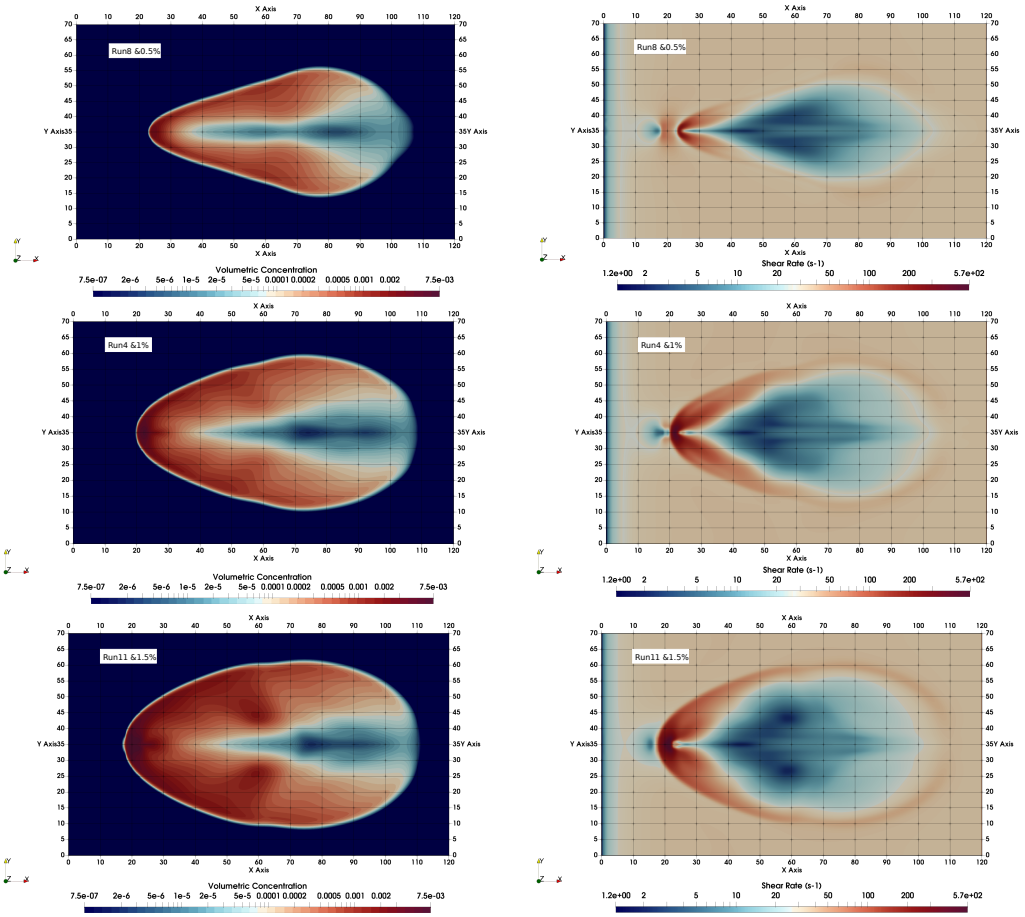

Figure 6.13: The volumetric concentration field and shear rates for Runs 8, 4, and 11 on the left and right are shown here. In these runs, the PNMT forward velocity is 0.25 m/s.

Special attention has to be given to to Runs 4 and 11 due to the sub-critical flow at discharge (densimetric Froude number $\lesssim 1$), which may cause non-uniform sediment distribution during discharge. However, to simplify the discharge number, it is assumed to be homogeneous. Figure 6.14 depicts two sections per run, demonstrating how the current flows beneath and next to the PNMT. This occurs primarily due to three mechanisms combined:

1. sub-critical regime at the discharge (densimetric Froude number $\lesssim 1$),
2. low PNMT velocity,
3. velocity ratio $r \leq 1$.

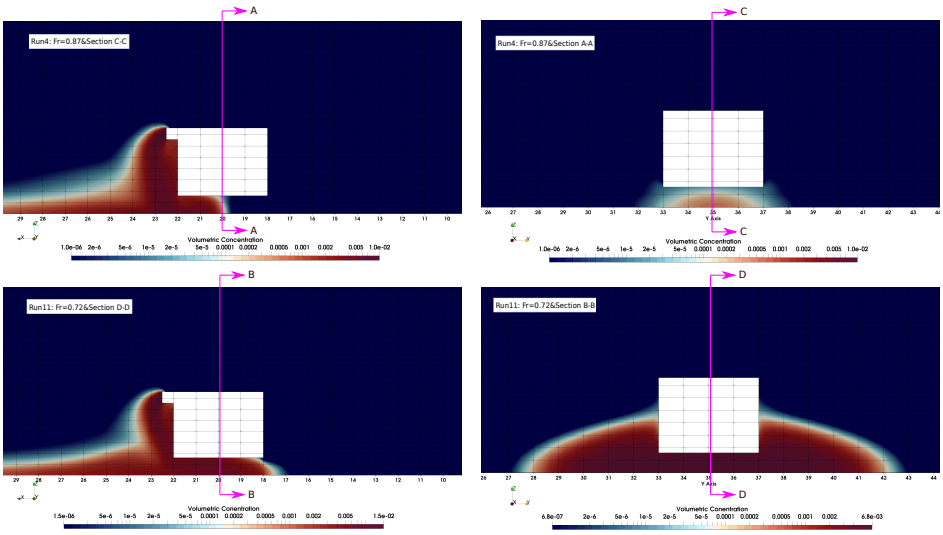

Figure 6.14: Sections of the PNMT region in Runs 4 and 11 demonstrate the potential for turbidity currents to flow beneath the PNMT and advance the collector over time.

To better understand the dynamics of the turbidity currents beneath the PNMT, there are several factors that need to be investigated further. First, it is unclear whether the critical transition value for the current to start flowing underneath the PNMT occurs at $Fr_d = 1$ at the discharge or if it is at a different value. Additionally, the height of the discharge above the bed is another crucial factor that may affect the advancement of the current. This is because the potential energy of the mixture will differ, resulting in

variations in the flow development of the mixture in the jet/plume phase. Such variations can have an impact on the concentration at the impingement region. Currently, it remains unknown whether changing the height of the discharge affects the current's ability to advance beneath the PNMT, even with subcritical flow at the discharge. Furthermore, while Runs 4 and 11 only differ in their initial sediment concentration, it is important to consider the effects of varying the mixture volume flux while keeping the same sediment flux. This will help to better understand the dynamics of the current and its potential to advance beyond the PNMT.

Sideways Propagating Turbidity Current Analysis

In this study, we are specifically interested in investigating the parameters of the sideways propagating turbidity current for the group of runs - Runs 1, 7, and 10 (Figure 6.15). We have excluded the comparing runs - Runs 4, 8 and 11- from our analysis as Runs 4 and 11 do not achieve the steady-state condition at the location of 30 m, as shown in Figure 6.1. Specifically, Runs 4 and 11 exhibit a unique trend where they advance the PNMT, which makes them unsuitable for comparison. Therefore, we will focus solely on comparing the Runs 1 ,7 and 10 for our investigation of the sideways propagating turbidity current parameters.

Figure 6.15 displays four variables: the sediment flux, α_{28} flux, the velocity of the sideways propagating current, and the total sediment distribution. The figure clearly indicates that low initial concentration at the discharge leads to higher sediment flux and velocity, including α_{28}. The trend continues with increasing initial concentration, suggesting that a higher initial concentration at the discharge may be beneficial. However, it is important to note that the vertical profile is taken at the same location for all the runs, but not at the same time/phase domain of the turbidity current for each run.

Increasing the initial concentration at the discharge leads to a larger angle of the wedge, which means that the sideways propagating turbidity current in the case of higher initial concentration develops faster in the lateral direction with a higher run-out distance. Consequently, the position of the profile taken may be at the head of the current for one run, like Run 7, while it might be in the body for another run, such as Run 10. This explains the higher parameters observed in Figure 6.15 for certain runs.

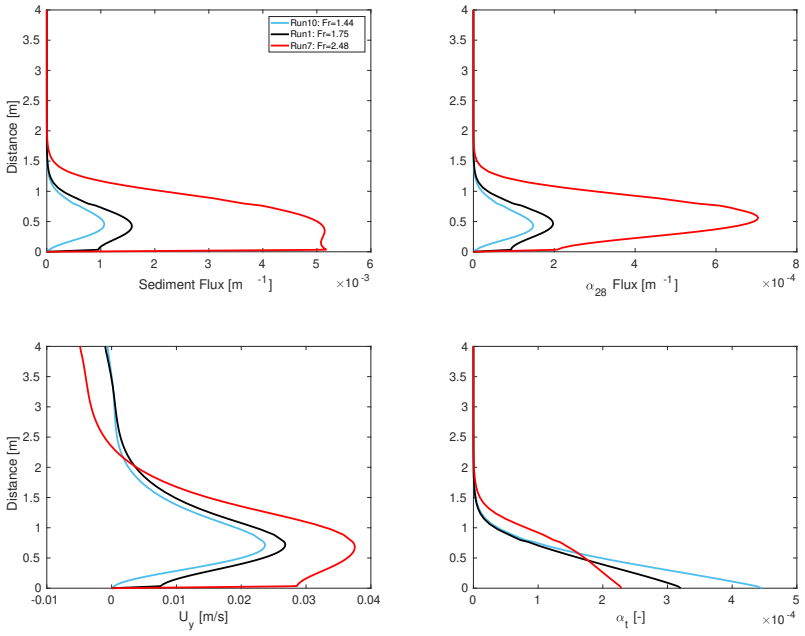

Figure 6.15: This plot shows four variables at the intersection of 70 in the X direction and 30 in the Y direction: the total sediment flux **(top-left)**, the largest fraction flux **(top-right)**, the sideways propagating current velocity **(bottom-left)**, and the total volumetric concentration **(bottom-right)**.

6.4 Discussion

The results of the different runs have yielded valuable insights into the effects of various parameters on the near field from the PNMT. In this section, we present a comprehensive discussion of all four parameters that are tested. The aim of this discussion is to develop a framework that will facilitate a deeper understanding of the PNMT discharge mixture and its associated dynamics. .

To analyze the effect of the four variables of interest on the sediment flux and α_{28}, we integrated the profiles at 4 meters depth and obtained a single value for each run. By plotting the integrated values on the Y-axis against each of the four variables on the X-axis, we can observe the trends associated with each variable (see fig. 6.16). This analysis allowed us to gain insights

into the impact of each variable on the sediment flux and α_{28}, as well as to identify any correlations or patterns that may exist between the variables and the integrated values.

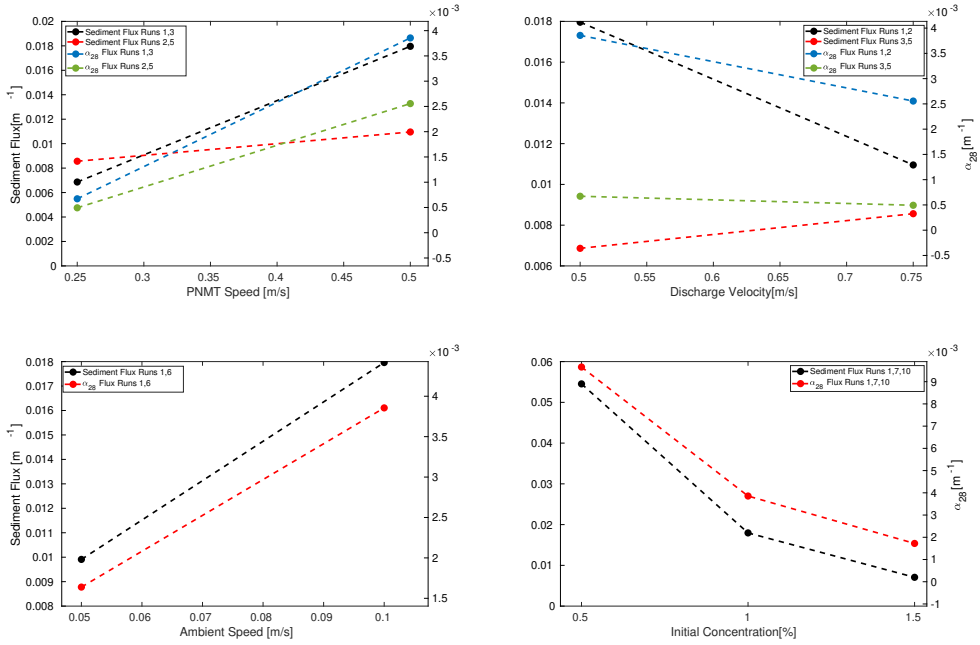

Figure 6.16: This plot shows the integration of the sediment flux **(left y axis)** and α_{28} flux **(right y axis)**, for the 4 variables of interest, namely PNMT velocity **(top-left)**, discharge velocity **(top-right)**, ambient velocity **(bottom-left)**, and the initial concentration **(bottom-right)**.

Generally, increasing the velocities of both the PNMT and the ambient current can enhance flocculation due to the shear generated by their hydrodynamics effect. However, this increase in velocity can also result in a greater sediment flux being transported to the far-field. Furthermore, increasing the discharge velocity usually leads to a higher sediment flux and a slower flocculation pace, except in Runs 1 and 2, which exhibit slightly different behavior. This may be due to the higher PNMT velocity, as these two runs involve a PNMT moving at a velocity of 0.5 m/s

To further investigate the effect of the velocity ratio r on the turbidity

current's dispersion in the near-field, we selected four runs (5, 3, 2, 1) that have varying discharge velocity and velocity ratio while keeping the initial concentration and ambient current velocity constant. Figure 6.17 shows the sediment flux and α_{28} flux for each run, allowing us to observe the trends associated with each variable. As we can see, increasing the velocity ratio r generally increases the amount of transported sediment flux while also increasing flocculation, which may have a more beneficial long-term effect.

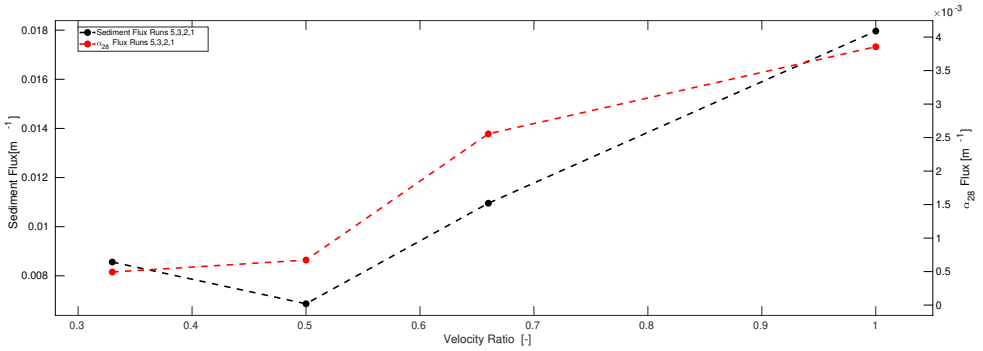

Figure 6.17: This plot shows the integration of the sediment flux **(left y axis)** and α_{28} flux **(right y axis)**, for a changing velocity ratio.

Another crucial parameter to consider is the initial concentration. While it may appear from Figure 6.16 that increasing the initial concentration leads to lower sediment flux and flocculation, this is not necessarily the case. As mentioned earlier, increasing the initial concentration leads to a wide angle wedge shape, making it challenging to compare sediment and α_{28} fluxes across different runs.

The results obtained suggest a correlation between the initial concentration, PNMT velocity, and discharge velocity, with increasing initial concentration and keeping velocity ratio $r$to be 1 (i.e., decreasing the Froude number at the discharge) resulting in the turbidity current flowing beneath or even ahead of the PNMT. The aforementioned phenomenon was also noted in the direct numerical simulations conducted by Ouillon et al. (2021). Our observation indicates that when $Fr \lesssim 1$ and PNMT is slow ($U_{PNMT} = 0.25$ m/s) and keeping the velocity ratio r equals 1, the current exhibits this behavior, but it is unknown whether $Fr_d = 1$ marks a turning point for this phenomenon. Additionally, it is unclear whether increasing the volume flux of the water-

sediment mixture while keeping the sediment flux constant (i.e., increasing the size of the discharge device) and lowering the densimetric froude number of the discharge will result in the same behavior. Thus, further investigations are necessary. In conclusion, based on the observed correlation between the mixture and the PNMT, we hypothesize that this interaction could be utilized as an engineering solution to generate additional mixing, potentially leading to enhanced flocculation and settling.

6.5 Conclusions and recommendations

To investigate the movement of a PNMT, 3D CFD simulations are run for various discharge scenarios. The scenarios varied in terms of the initial concentration, ambient current velocity of the mixture, discharge velocity, and PNMT forward velocity.

In conclusion, it can be observed that increasing certain parameters such as PNMT velocity, initial concentration, and ambient current velocity can result in an increase in transported sediment flux to the far-field, as well as an enhanced potential for flocculation occurrence in the near-field. On the other hand, increasing discharge velocity can lead to higher sediment flux leaving the near-field with a slower flocculation pace. Moreover, maintaining a lower Froude number ($Fr \lesssim 1$) at the discharge and slower PNMT velocity, with a velocity ratio r of 1 allow the turbidity current to flow under the PNMT and even ahead of it.

There are several other factors that might impact the dispersion of the sideways propagating turbidity currents. These factors include the height, position and orientation of the discharge geometry and the volume fraction, which can be increased while maintaining a constant amount of sediment. Furthermore, during the investigation of the impact of discharge velocities, it was observed that there is a deviation from the anticipated trend for runs with high PNMT velocity. Further investigation is required to determine the root cause of this deviation. Additionally, some of the runs did not achieve steady-state conditions within 250 seconds of simulation time, indicating that these runs must continue until steady-state conditions are reached. However, this prolonged duration may also impact the flocculation nature of the particles, causing them to either aggregate or break-up. To ensure a fair comparison,

all numerical runs should be extended to the same reference time.

The turbulence structure is still an important consideration, as our turbulence model is time-averaged and does not provide an accurate description of the turbulence structure. Large-eddy simulation (LES) could be a better option for investigating the flow structure, although it come with higher computational demands.

Chapter 7

Conclusions and Prospects

Abstract

This chapter presents a recapitulation of the dissertation outcomes in the form of answers to the research question presented in chapter 1. The findings of this study opens up new prospects for the existing form of polymetallic nodules mining, and thus suggestions and recommendations are provided.

7.1 Conclusions

The growing focus on limiting the dispersion of DSM-generated turbidity flows is driving the need for greater understanding of turbid flows. For example, classifying flow types in the near-field region has allowed us to study the nature of these flows in a detailed manner, providing a clearer understanding of the effect of sediment particle size and settling velocity on the development of turbidity currents. This motivated further numerical studies aimed at promoting particle aggregation to increase their size, subsequently enhancing their settling potential, which would decrease the driving buoyancy forces of turbidity currents. Furthermore, the knowledge gained from this study can offer valuable insights to include during the design process of PNMT systems. Therefore, this dissertation aims at improving the current understanding of generated turbidity flows nature in the near-field region by answering the following three research questions.

1. How do sediment particle size and concentration at the impingement region influence the development of the turbidity current?
2. How does flocculation influence the generated turbidity current?
3. How do discharge conditions affect the dispersion of the generated turbidity current?

To pursue answers to these questions, a literature review is carried out, followed by 1D numerical modeling of real discharge scenarios. Furthermore, a series of lock-exchange experiments was conducted with different sediment types to obtain results that could be used for validating a newly-implemented multi-fractions mixture model. Finally, the model is further extended to consider flocculation dynamics, enabling a detailed numerical study of turbid flows in the near-field region.

Influence of sediment particle size and concentration on turbidity current development.

During the lock-exchange experiments, the local concentration of the generated turbidity current is measured using pixel-concentration calibration method.

In addition, the forward velocity of the turbidity current was measured during the experiments. The time-distance curves are used to identify and distinguish the different phases of a turbidity current. Flow measurements have shown that:

1. The particle size and initial sediment concentration of a lock-exchange turbidity current can affect its propagation behavior.
2. The lowest forward velocity and concentration distribution were observed under conditions of lower initial sediment concentration and higher sediment particle settling velocities, indicating that these conditions are favorable in the impingement region.
3. The current generated exhibits a shorter transition time from the self-similar phase to the viscous phase under conditions of lower initial sediment concentration and higher sediment particle settling velocity. This results in a faster dissipation of the current.
4. When the initial concentration of sediment particles exceeds a threshold of 1.5%, the density difference becomes dominant, resulting in an unaffected propagation speed of the current by particle size. However, it is important to emphasize that this conclusion is limited to the type of sediment used and the tank length scales examined in Chapter 4.

Finally, the numerical results of the newly implemented solver in OpenFOAM are compared to the experimental results by utilizing the flow measurements obtained from the experiments. The key findings of this study include:

1. The recently implemented drift-flux model with multiple fractions can accurately predict the evolution of turbidity currents.
2. The accuracy of the predictions depends on the number of fractions used, with a greater degree of accuracy achieved when a higher number of fractions are utilized.

Role of Flocculation in DSM-generated Turbidity Flows

Given the cohesive properties of deep sea sediment and the presence of organic material, flocculation could be a key factor in increasing particle size and,

therefore, the settling velocity. The newly validated multi-fraction drift-flux model, when coupled with the population balance equation, provides a unique tool for modeling the hydrodynamics of the water-in-situ CCZ sediment mixture. The numerical results of this study highlight the role of flocculation in the dispersion of turbid flows in the near-field and far-field regions as follows:

1. The wake generated in the vicinity of the PNMT increases the possibility of particle aggregation, resulting in the formation of larger flocs that settle faster as the turbidity current subsides.

2. Sediment readily flocculates to form larger particles that will settle as soon as the turbidity current subsides enough to allow this to happen, which is likely occurring in the far-field region.

3. Although the influence of flocculation is present in the near-field region, it does not significantly affect the turbidity current in that region.

4. The aggregation mechanism is more dominant than the break-up mechanism.

Effect of Operational Parameters on the Propagation Behavior and Flocculation of Turbidity Currents in the Near-Field Region

The model developed in Chapter 5 was used to investigate the effect of various discharge scenarios on the propagation behavior of turbidity currents in the near-field region. Four main variables were studied in our test matrix, including PNMT forward velocity, ambient current velocity, discharge velocity, and initial concentration. The numerical simulations revealed the following key findings:

1. Increasing PNMT forward velocity, initial concentration, and ambient current velocity can lead to a larger transported sediment flux to the far-field and a higher potential for flocculation in the near-field.

2. Increasing discharge velocity can result in a higher sediment flux leaving the near-field, but with a slower flocculation pace.

3. In the case of a lower densimetric Froude number ($Fr_d < 1$) at the discharge and a slower PNMT speed, with a PNMT speed/discharge velocity ratio of 1, the turbidity current can flow under the PNMT and even ahead of it.

7.1.1 Recommendations

Based on the outcomes of the current study, future research can be pointed out. The recommendations are presented as follows:

Experimental Study

On Lab Scale

In Chapter 4, non-cohesive sediment types were utilized, thus the impact of flocculation was not observed. To gain a more comprehensive understanding of turbidity flows in the near field, it is necessary to conduct experiments that capture the effects of flocculation using in-situ CCZ sediment at shear rates experienced in the wake region behind the PNMT. Additionally, quantifying turbulence in the wake region is a critical area of future study, which can be accomplished through proper scaling of the PNMT. Together, these flocculation and wake experiments can provide valuable insights into the structure of turbidity flows in the near field.

Although conducting flocculation experiments requires in-situ CCZ sediment, which is not always present, it may be feasible to replicate similar characteristics of CCZ sediment in a laboratory setting. By doing so, we can mimic the flocculation behavior, as well as settling velocity distribution, enabling further studies in a controlled lab environment.

Only experimental work has been conducted on flocculation using in-situ CCZ sediment, as described in the study by Gillard et al. (2019). However, this work did not employ in-situ CCZ seawater, but rather artificial seawater, and thus they did not consider the impact of key factors such as extracellular polymeric substances (EPS) and bacteria present in real CCZ water on the aggregation of particles. Therefore, additional laboratory experiments are needed to design CCZ seawater in the lab, in order to study flocculation in the context of CCZ.

On Field Scale

Although there have been some direct measurements of the discharge at the PNMT, the current literature lacks comprehensive data on various design realizations. To enhance our understanding of the discharge, it is essential

to quantify the discharge source at the PNMT, including parameters such as PSD, discharge velocity, and initial concentration. By collecting and analyzing these datasets for different design realizations, we can improve the input for numerical models, leading to more accurate predictions.

Numerical Modelling

The 1D layer-averaged turbidity currents model proposed by Parker et al. (1986) was used to model the turbidity current over a 100 m distance downstream of a fixed discharge from a PNMT. However, we recognize that this model may not accurately represent the actual propagation of turbidity currents in the near field. In reality, turbidity currents can propagate both longitudinally and laterally, and our current understanding suggests that the large turbidity flows behind the PNMT consist mainly of lateral turbidity currents that propagate almost perpendicular to the PNMT direction. Therefore, we suggest that further development of the turbidity current model proposed by Parker et al. (1986) is necessary to properly study the sideways propagation of turbidity currents, while also taking into account the motion of the PNMT.

While the turbidity current is propagating along the seabed, and due to the shear velocity of the current with the seabed, the current might pick up sediment particles from the seabed; this process is known as erosion. The current drift-flux-PBE model still lacks some important closures, such as erosion closure. Moreover, because of the potential energy that the mixture possesses at the moment of discharge, the mixture might switch between two main mechanisms at the impingement region: deposition and erosion. Therefore, modeling sediment pick-up due to flow shear-rate would create more accurate predictions

Another key important factor in studying flocculation mechanisms is the representation of turbulence. Flocculation source terms are typically calculated based on the shear rate, which is determined from turbulence modeling. To improve our understanding of these mechanisms, it is recommended that turbidity flows be modeled using Large Eddy Simulation (LES). By employing this, a better estimation for the shear rate will be calculated, in turn, we can gain a more solid understanding of the flocculation process, resulting in a better prediction of the fate of sediment particles.

To improve the accuracy of estimating the transition from the turbidity current phase to the passive-transport phase, it would be beneficial to couple the near and far field models together. The different resolutions of these models can be addressed by inputting the output of the near-field model into the far field model. Based on our modeling of different discharge scenarios, we have observed that the flow behind the PNMT reaches a steady-state condition at a specific location. However, over time, the entire domain reaches the steady-state case. We can use the concentration, velocity, and PSD data from this steady-state case as input into the lower resolution grids of the far-field model. By applying this data as a boundary condition, we can create a more accurate and consistent representation of the transition from the turbidity current phase to the passive-transport phase.

It is important to consider the limitations of the simulations conducted in Chapters 5 and 6. Specifically, the discharge scenarios and numerical model were idealized and did not fully capture the complexities of real-world scenarios. For example, the simulations assumed a flat sea bed, which may not be the case in actual situations where there may be slopes or bumps. Additionally, the ambient current direction was assumed to be parallel to the discharge direction, while in reality, there may be an angle of attack that could affect the behavior of turbidity currents behind the PNMT. Therefore, future research should aim to extend the current numerical model to consider more realistic scenarios and variables in the simulations to better understand the behavior of turbidity currents and the effectiveness of the PNMT. This could involve utilizing more advanced numerical models that can account for variations in the sea bed topography and ambient current direction.

Bibliography

Adduce, C., Sciortino, G., & Proietti, S. (2012). Gravity currents produced by lock exchanges: Experiments and simulations with a two-layer shallow-water model with entrainment. *Journal of Hydraulic Engineering*, *138*(2), 111–121.

Alhaddad, S., de Wit, L., Labeur, R. J., & Uijttewaal, W. (2020). Modeling of breaching-generated turbidity currents using large eddy simulation. *Journal of Marine Science and Engineering*, *8*(9), 728.

Alhaddad, S., & Helmons, R. (2023). Sediment erosion generated by a coandă-effect-based polymetallic-nodule collector. *Journal of Marine Science and Engineering*, *11*(2), 349.

Ali, W., Enthoven, D., Kirichek, A., Chassagne, C., & Helmons, R. (2022). Effect of flocculation on turbidity currents. *Frontiers in earth science*, *10*, 1014170.

Allen, J. (1971). Mixing at turbidity current heads, and its geological implications. *Journal of Sedimentary Research*, *41*(1), 97–113.

Altinakar, S., Graf, W. H., & Hopfinger, E. (1990). Weakly depositing turbidity current on a small slope. *Journal of Hydraulic Research*, *28*(1), 55–80.

BGR. (2019). *Environmental impact assessment* (tech. rep.). Bundesanstalt für Geowissenschaften und Rohstoffe.

Bhole, M., Joshi, J., & Ramkrishna, D. (2008). Cfd simulation of bubble columns incorporating population balance modeling. *Chemical Engineering Science*, *63*(8), 2267–2282.

Biggs, C., & Lant, P. (2002). Modelling activated sludge flocculation using population balances. *Powder Technology*, *124*(3), 201–211.

Bischoff, J. L., Heath, G. R., & Leinen, M. (1979). Geochemistry of deep-sea sediments from the pacific manganese nodule province: Domes sites a, b, and c. In *Marine geology and oceanography of the pacific manganese nodule province* (pp. 397–436). Springer.

Bleninger, T., Lipari, G., & Jirka, G. H. (2002). Design and optimization program for internal diffuser hydraulics. *Proceedings of the 2nd International Conference Marine Waste Water Discharges, Istanbul, Turkey*, *9*.

Bobba, S., Claudiu, P., Huygens, D., Alves Dias, P., Gawlik, B., Tzimas, E., Wittmer, D., Nuss, P., Grohol, M., Saveyn, H., et al. (2018). Report on critical raw materials and the circular economy. *Luxembourg: EU*.

Burt, D. (2010). *Improved design of settling tanks using an extended drift flux model* (Doctoral dissertation). University of Bristol Bristol, UK. https://doi.org/10.13140/RG.2.1.5109.2082

Cahill, J., Cummins, P., Staples, E., & Thompson, L. (1987). Size distribution of aggregates in flocculating dispersions. *Journal of colloid and interface science*, *117*(2), 406–414.

Cantero, M., Garcia, M., Buscaglia, G., Bombardelli, F., & Dari, E. (2003). Multidimensional cfd simulation of a discontinuous density current. *Proceedings of the XXX IAHR International Congress*, 24–29.

Carazzo, G., Kaminski, E., & Tait, S. (2006a). The route to self-similarity in turbulent jets and plumes. *Journal of Fluid Mechanics*, *547*, 137–148.

Carazzo, G., Kaminski, E., & Tait, S. (2006b). The route to self-similarity in turbulent jets and plumes. *Journal of Fluid Mechanics*, *547*, 137–148. https://doi.org/10.1017/S002211200500683X

Carlotti, P., & Hunt, G. R. (2005). Analytical solutions for turbulent non-boussinesq plumes. *Journal of Fluid Mechanics*, *538*, 343–359.

Chen, F., Simon, C., & Lai, A. C. (2006). Modeling particle distribution and deposition in indoor environments with a new drift–flux model. *Atmospheric Environment*, *40*(2), 357–367.

Chen, H. (1991). Turbulent boyant jets and plumes in flowing ambient environments.

Chen, W., Fischer, R. R., & Berg, J. C. (1990). Simulation of particle size distribution in an aggregation-breakup process. *Chemical Engineering Science*, *45*(9), 3003–3006. https://doi.org/https://doi.org/10.1016/0009-2509(90)80201-O

Chowdhury, M., & Testik, F. (2011). Laboratory testing of mathematical models for high-concentration fluid mud turbidity currents. *Ocean engineering*, *38*(1), 256–270.

Clift, R., Grace, J. R., & Weber, M. E. (1979). *Bubbles, Drops and Particles* (Vol. 94). https://doi.org/10.1017/s0022112079221290

Corliss, B. H. (1985). foraminifera within deep-sea sediments F-1. *314*(April), 4–7.

Craske, J., Debugne, A. L., & van Reeuwijk, M. (2015). Shear-flow dispersion in turbulent jets. *Journal of Fluid Mechanics*, *781*, 28–51.

Cuthbertson, A. J., Apsley, D. D., Davies, P. A., Lipari, G., & Stansby, P. K. (2008). Deposition from particle-laden, plane, turbulent, buoyant jets. *Journal of Hydraulic Engineering*, *134*(8), 1110–1122.

Cuyvers, L., Berry, W., Gjerde, K., Thiele, T., & Wilhem, C. (2018). *Deep seabed mining, a rising environmental challenge*. IUCN Gland, Switzerland.

Davidson, G. (1986). Gaussian versus top-hat profile assumptions in integral plume models. *Atmospheric Environment (1967)*, *20*(3), 471–478.

Decrop, B., De Mulder, T., Troch, P., Toorman, E., & Sas, M. (2013). Experimental investigation of negatively buoyant sediment plumes resulting from dredging operations. *CoastLab 2012*, 573–582.

Decrop, B., & Wachter, T. D. (2019). Detailed CFD Simulations For near Field Dispersion Of Deep Sea Mining Plumes, 116–127.

Delichatsios, M. (1979). Time similarity analysis of unsteady buoyant plumes in neutral surroundings. *Journal of Fluid Mechanics*, *93*(2), 241–250.

Department of Commerce. (1977). *Deep Ocean Mining Enviromental Study –Information And Issues* (tech. rep.).

de Wit, L., Talmon, A., & Van Rhee, C. (2014). 3d cfd simulations of trailing suction hopper dredger plume mixing: Comparison with field measurements. *Marine pollution bulletin*, *88*(1-2), 34–46.

de Wit, L., van Rhee, C., & Keetels, G. (2014). Turbulent interaction of a buoyant jet with cross-flow. *Journal of Hydraulic Engineering*, *140*(12), 04014060.

(DHPC), D. H. P. C. C. (2022). DelftBlue Supercomputer (Phase 1).

Drew, D. A. (1983). Mathematical modeling of two-phase flow. *Annual review of fluid mechanics*, *15*(1), 261–291.

Elerian, M., Alhaddad, S., Helmons, R., & van Rhee, C. (2021). Near-field analysis of turbidity flows generated by polymetallic nodule mining tools. *Mining*, *1*(3), 251–278.

Elerian, M., Van Rhee, C., & Helmons, R. (2022). Experimental and numerical modelling of deep-sea-mining-generated turbidity currents. *Minerals*, *12*(5). https://doi.org/10.3390/min12050558

Ferguson, R., & Church, M. (2004). A simple universal equation for grain settling velocity. *Journal of sedimentary Research*, *74*(6), 933–937.

Fernández-Barbero, A., Schmitt, A., Cabrerizo-Vılchez, M., & Martınez-Garcıa, R. (1996). Cluster-size distribution in colloidal aggregation monitored by single-cluster light scattering. *Physica A: Statistical Mechanics and its Applications*, *230*(1-2), 53–74.

Fernando, H. J. (2012). Handbook of environmental fluid dynamics, volume one: Overview and fundamentals.

Fischer, H. B., List, J. E., Koh, C. R., Imberger, J., & Brooks, N. H. (1979). *Mixing in inland and coastal waters*. Academic press.

Flesch, J. C., Spicer, P. T., & Pratsinis, S. E. (1999). Laminar and turbulent shear-induced flocculation of fractal aggregates. *AIChE journal*, *45*(5), 1114–1124.

Fox, D. G. (1970). Forced plume in a stratified fluid. *Journal of Geophysical Research*, *75*(33), 6818–6835.

Garcia, M. H. (1994). Depositional turbidity currents laden with poorly sorted sediment. *Journal of hydraulic engineering*, *120*(11), 1240–1263.

Georgoulas, A. N., Angelidis, P. B., Panagiotidis, T. G., & Kotsovinos, N. E. (2010). 3d numerical modelling of turbidity currents. *Environmental fluid mechanics*, *10*(6), 603–635.

Gillard, B., Purkiani, K., Chatzievangelou, D., Vink, A., Iversen, M. H., & Thomsen, L. (2019). Physical and hydrodynamic properties of deep sea mining-generated, abyssal sediment plumes in the clarion clipperton fracture zone (eastern-central pacific). *Elementa: Science of the Anthropocene*, *7*.

Gillard, B., & Thomsen, L. (2019). *Characterization of sediment plumes behind mining vehicles in the NORI area (laboratory analyses)* (tech. rep.). iSeaMC.

Gladstone, C., Phillips, J., & Sparks, R. (1998). Experiments on bidisperse, constant-volume gravity currents: Propagation and sediment deposition. *Sedimentology*, *45*(5), 833–843.

Global Sea Mineral Resources NV. (2018). *Environmental impact statement* (tech. rep. No. 1). https://doi.org/10.1007/978-3-642-79940-2_11

Goeree, J. (2018). *Drift-flux modeling of hyper-concentrated solid-liquid flows in dredging applications* (Doctoral dissertation).

Goeree, J. C., Keetels, G. H., Munts, E. A., Bugdayci, H. H., & van Rhee, C. (2016). Concentration and velocity profiles of sediment-water mixtures using the drift flux model. *The Canadian Journal of Chemical Engineering*, *94*(6), 1048–1058.

Golzarijalal, M., Zokaee Ashtiani, F., & Dabir, B. (2018). Modeling of microalgal shear-induced flocculation and sedimentation using a coupled cfd-population balance approach. *Biotechnology Progress*, *34*(1), 160–174.

Grunsven, F., Keetels, G., & Rhee, C. (2018). The initial spreading of turbidity plumes – dedicated laboratory experiments for model validation.

Grunsven, F., Keetels, G., & van Rhee, C. (2016). Modeling offshore mining turbidity sources. *WODCON XXI: Innovations in dredging*.

GSR. (2018). *Blue nodules deliverable report d3.4, report describing the process flow overview* (tech. rep.). Global Sea Mineral Resources NV.

GSR, G. S. M. R. (2018). *Environmental impact statement: Small-scale testing of nodule collector components on the seafloor of the clarion-clipperton fracture zone and its environmental impact* (tech. rep.). Global Sea Mineral Resources NV.

Guillaume, R. (2023). Securing europe's supply of critical raw materials: The material nature of the eu's strategic goals.

Haalboom, S., de Stigter, H. C., Mohn, C., Vandorpe, T., Smit, M., de Jonge, L., & Reichart, G.-J. (2023). Monitoring of a sediment plume produced by a deep-sea mining test in shallow water, málaga bight, alboran sea (southwestern mediterranean sea). *Marine Geology*, *456*, 106971.

Haeckel, M. (2018). Mining Impact; Environmental Impacts and Risks of Deep-Sea Mining, 1–64.

Hage, S., Cartigny, M. J., Sumner, E. J., Clare, M. A., Hughes Clarke, J. E., Talling, P. J., Lintern, D. G., Simmons, S. M., Silva Jacinto, R., Vellinga, A. J., et al. (2019). Direct monitoring reveals initiation of turbidity currents from extremely dilute river plumes. *Geophysical Research Letters*, *46*(20), 11310–11320.

Hanna, S. R. (2012). Atmospheric turbulence and diffusion laboratory national oceanic and atmospheric administration. *Air Pollution Modeling and Its Application I*, *1*, 337.

Harris, T. C., Hogg, A. J., & Huppert, H. E. (2002). Polydisperse particle-driven gravity currents. *Journal of Fluid Mechanics*, *472*, 333–371.

Härtel, C., Meiburg, E., & Necker, F. (2000). Analysis and direct numerical simulation of the flow at a gravity-current head. part 1. flow topology

and front speed for slip and no-slip boundaries. *Journal of Fluid Mechanics*, *418*, 189–212.

Hein, J. R., Koschinsky, A., & Kuhn, T. (2020). Deep-ocean polymetallic nodules as a resource for critical materials. *Nature Reviews Earth & Environment*, *1*(3), 158–169.

Helmons, R., de Wit, L., de Stigter, H., & Spearman, J. (2022). Dispersion of benthic plumes in deep-sea mining: What lessons can be learned from dredging? *Frontiers in Earth Science*, 796.

Henniger, R., & Kleiser, L. (2011). Large-eddy simulation of particle-driven gravity currents using the relaxation-term model. *Journal of Physics: Conference Series*, *318*(5), 052008.

Henniger, R., Meiburg, E., & Kleiser, L. (2008). Large-eddy simulation of particle-driven gravity-currents. *APS Division of Fluid Dynamics Meeting Abstracts*, *61*, GQ–009.

Hounslow, M., Ryall, R., & Marshall, V. (1988). A discretized population balance for nucleation, growth, and aggregation. *AIChE journal*, *34*(11), 1821–1832.

Hunt, G., & Van den Bremer, T. (2011). Classical plume theory: 1937–2010 and beyond. *IMA journal of applied mathematics*, *76*(3), 424–448.

Huppert, H. E., & Simpson, J. E. (1980). The slumping of gravity currents. *Journal of Fluid Mechanics*, *99*(4), 785–799.

Ishii, M. (1975). Thermo-fluid dynamic theory of two-phase flow. *NASA Sti/recon Technical Report A*, *75*, 29657.

Jankowski, J., Malcherek, A., & Zielke, W. (1994). Numerical modeling of sediment transport processes caused by deep sea mining discharges. *Proceedings of OCEANS'94*, *3*, III–269.

Jeldres, R. I., Concha, F., & Toledo, P. G. (2015). Population balance modelling of particle flocculation with attention to aggregate restructuring and permeability. *Advances in colloid and interface science*, *224*, 62–71.

Johnson, M. A. (1962). Turbidity currents.

Keulegan, G. H. (1958). *Twelfth progress report on model laws for density currents: The motion of saline fronts in still water* (Vol. 5831). US Department of Commerce, National Bureau of Standards.

Kirwan, A., Doyle, L., Bowles, W., & Brooks, G. (1986). Time-dependent hydrodynamic models of turbidity currents analyzed with data from the grand banks and orleansville events. *Journal of Sedimentary Research*, *56*(3), 379–386.

Kneller, B., & Buckee, C. (2000). The structure and fluid mechanics of turbidity currents: A review of some recent studies and their geological implications. *Sedimentology*, *47*, 62–94.

Kranenburg, C. (1994). The fractal structure of cohesive sediment aggregates. *Estuarine, Coastal and Shelf Science*, *39*(5), 451–460.

Kulkarni, C. S., Haley, P. J., Lermusiaux, P. F., Dutt, A., Gupta, A., Mirabito, C., Subramani, D. N., Jana, S., Ali, W. H., Peacock, T., et al. (2018). Real-time sediment plume modeling in the southern california bight. *OCEANS 2018 MTS/IEEE Charleston*, 1–10.

Lane-Serff, G. F., & Moran, T. J. (2005). Sedimentation from buoyant jets. *Journal of hydraulic engineering*, *131*(3), 166–174.

Lee, J. H., Chu, V., & Chu, V. H. (2003). *Turbulent jets and plumes: A lagrangian approach* (Vol. 1). Springer Science & Business Media.

Lee, J. H., & Cheung, V. (1990). Generalized lagrangian model for buoyant jets in current. *Journal of Environmental Engineering*, *116*(6), 1085–1106.

Lee, Li, A. C., & Lee, J. H. (2013). Structure of a horizontal sediment-laden momentum jet. *Journal of Hydraulic Engineering*, *139*(2), 124–140.

Lee, W., Li, A. C., & Lee, J. H. (2013). Structure of a horizontal sediment-laden momentum jet. *Journal of Hydraulic Engineering*, *139*(2), 124–140.

Lescinski, J., Jeuken, C., Cronin, K., Vroom, J., & Elias, E. (2014 b). *Modelling investigations on mine tailing plume dispersion on the Chatham Rise1209110* (tech. rep.). Deltares.

Li, X.-Y., & Logan, B. E. (2001). Permeability of fractal aggregates. *Water research*, *35*(14), 3373–3380.

Lombardi, V., Adduce, C., & La Rocca, M. (2018). Unconfined lock-exchange gravity currents with variable lock width: Laboratory experiments and shallow-water simulations. *Journal of Hydraulic Research*, *56*(3), 399–411.

Maciąg, Ł., & Harff, J. (2020). Application of multivariate geostatistics for local-scale lithological mapping–case study of pelagic surface sediments from the clarion-clipperton fracture zone, north-eastern equatorial pacific (interoceanmetal claim area). *Computers & Geosciences*, *139*, 104474.

Maggi, F. (2009). Biological flocculation of suspended particles in nutrient-rich aqueous ecosystems. *Journal of Hydrology*, *376*(1-2), 116–125.

Manninen, M., Taivassalo, V., & Kallio, S. (1996). *On the mixture model for multiphase flow* [Project code: 21HIPO Project code: N5SU00204]. VTT Technical Research Centre of Finland.

Marjanovic, G., Taub, G., & Balachandar, S. (2019). On the effects of buoyancy on higher order moments in lazy plumes. *Journal of Turbulence*, *20*(2), 121–146.

McKernan, J. L., Ellenbecker, M. J., Holcroft, C. A., & Petersen, M. R. (2007). Evaluation of a proposed area equation for improved exothermic process control. *Annals of occupational hygiene*, *51*(8), 725–738.

Middleton, G. V. (1966). Experiments on density and turbidity currents: I. motion of the head. *Canadian Journal of Earth Sciences*, *3*(4), 523–546.

Middleton, G. V. (1993). Sediment deposition from turbidity currents. *Annual review of earth and planetary sciences*, *21*, 89–114.

Mietta, F., Chassagne, C., Verney, R., & Winterwerp, J. C. (2011). On the behavior of mud floc size distribution: Model calibration and model behavior. *Ocean Dynamics*, *61*, 257–271.

Miller, K., Brigden, K., Santillo, D., Currie, D., Johnston, P., & Thompson, K. (2021). Challenging the need for deep seabed mining from the perspective of metal demand, biodiversity, ecosystems services, and benefit sharing. *Frontiers in Marine Science*, 1040.

MIT Mechanical Engineering. (2019). Visualizing deep-sea mining. %5Curl%7Bhttps://www.youtube.com/watchv=Lwq1j3nOODA&ab_channel=MITMechanicalEngineering%7D

Morton, B., & Middleton, J. (1973). Scale diagrams for forced plumes. *Journal of Fluid Mechanics*, *58*(1), 165–176.

Morton, B., Taylor, G. I., & Turner, J. S. (1956). Turbulent gravitational convection from maintained and instantaneous sources. *Proceedings of the Royal Society of London. Series A. Mathematical and Physical Sciences*, *234*(1196), 1–23.

Morton, B. (1959). Forced plumes. *Journal of Fluid mechanics*, *5*(1), 151–163.

Muñoz-Royo, C., Ouillon, R., El Mousadik, S., Alford, M. H., & Peacock, T. (2022). An in situ study of abyssal turbidity-current sediment plumes generated by a deep seabed polymetallic nodule mining preprototype collector vehicle. *Science advances*, *8*(38), eabn1219.

Muñoz-Royo, C., Peacock, T., Alford, M. H., Smith, J. A., Le Boyer, A., Kulkarni, C. S., Lermusiaux, P. F., Haley, P. J., Mirabito, C., Wang, D., et al. (2021). Extent of impact of deep-sea nodule mining midwater plumes is influenced by sediment loading, turbulence and thresholds. *Communications Earth & Environment*, *2*(1), 1–16.

Murakami, S., Kato, S., Chikamoto, T., Laurence, D., & Blay, D. (1996). New low-reynolds-number k-ε model including damping effect due to buoyancy in a stratified flow field. *International journal of heat and mass transfer*, *39*(16), 3483–3496.

Necker, F., Härtel, C., Kleiser, L., & Meiburg, E. (2002). High-resolution simulations of particle-driven gravity currents. *International Journal of Multiphase Flow*, *28*(2), 279–300.

Neves, M., Neves, A., & Bleninger, T. (2002). Prediction on particle deposition in effluent disposal system. *Proceedings of the 2nd Intenational Conference Marine Waste Water Discharges, International Association for Hydro-Environment Engineering and Research (IAHR) and International Water Association (IWA), Istanbul, Turkey*, 16–20.

Nogueira, H. I., Adduce, C., Alves, E., & Franca, M. J. (2013a). Analysis of lock-exchange gravity currents over smooth and rough beds. *Journal of Hydraulic research*, *51*(4), 417–431.

Nogueira, H. I., Adduce, C., Alves, E., & Franca, M. J. (2013b). Image analysis technique applied to lock-exchange gravity currents. *Measurement Science and Technology*, *24*(4), 047001.

Normandeau, A., Lajeunesse, P., St-Onge, G., Bourgault, D., Drouin, S. S.-O., Senneville, S., & Bélanger, S. (2014). Morphodynamics in sediment-starved inner-shelf submarine canyons (lower st. lawrence estuary, eastern canada). *Marine Geology*, *357*, 243–255.

Oebius, H. U., Becker, H. J., Rolinski, S., & Jankowski, J. A. (2001). Parametrization and evaluation of marine environmental impacts produced by deep-sea manganese nodule mining. *Deep Sea Research Part II: Topical Studies in Oceanography*, *48*(17-18), 3453–3467.

Ooi, S. K., Constantinescu, G., & Weber, L. J. (2007). 2d large-eddy simulation of lock-exchange gravity current flows at high grashof numbers. *Journal of Hydraulic Engineering*, *133*(9), 1037–1047.

Ouillon, R., Kakoutas, C., Meiburg, E., & Peacock, T. (2021). Gravity currents from moving sources. *Journal of Fluid Mechanics*, *924*.

Parker, G., Fukushima, Y., & Pantin, H. M. (1986). Self-accelerating turbidity currents. *Journal of Fluid Mechanics*, *171*, 145–181.

Parker, G., Garcia, M., Fukushima, Y., & Yu, W. (1987). Experiments on turbidity currents over an erodible bed. *Journal of Hydraulic Research*, *25*(1), 123–147.

Parsons, J. D., Bush, J. W., & Syvitski, J. P. (2001). Hyperpycnal plume formation from riverine outflows with small sediment concentrations. *Sedimentology*, *48*(2), 465–478.

Petersen, S., Krätschell, A., Augustin, N., Jamieson, J., Hein, J. R., & Hannington, M. D. (2016). News from the seabed–geological characteristics and resource potential of deep-sea mineral resources. *Marine Policy*, *70*, 175–187.

Priestley, C., & Ball, F. (1955). Continuous convection from an isolated source of heat. *Quarterly Journal of the Royal Meteorological Society*, *81*(348), 144–157.

Prosperetti, A., & Tryggvason, G. (2009). *Computational methods for multiphase flow*. Cambridge university press.

Purkiani, K., Gillard, B., Paul, A., Haeckel, M., Haalboom, S., Greinert, J., Stigter, H. D., Hollstein, M., Baeye, M., Vink, A., et al. (2021). Numerical simulation of deep-sea sediment transport induced by a dredge experiment in the northeastern pacific ocean. *Frontiers in Marine Science*, 1175.

Quezada, G. R., Ayala, L., Leiva, W. H., Toro, N., Toledo, P. G., Robles, P., & I Jeldres, R. (2020). Describing mining tailing flocculation in seawater by population balance models: Effect of mixing intensity. *Metals*, *10*(2), 240.

Reichart, G.-J., Duineveld, G., van Rhee, C., & Lindeboom, H. J. (2013). *Towards Responsible ExtrAction of submarine mineral REsources (TREASURE)* (tech. rep.).

Richardson, J., & Zaki, W. (1954). The sedimentation of a suspension of uniform spheres under conditions of viscous flow. *Chemical Engineering Science*, *3*(2), 65–73.

Rooney, G., & Linden, P. (1996). Similarity considerations for non-boussinesq plumes in an unstratified environment. *Journal of fluid mechanics*, *318*, 237–250.

Rottman, J. W., & Simpson, J. E. (1983). Gravity currents produced by instantaneous releases of a heavy fluid in a rectangular channel. *Journal of Fluid Mechanics*, *135*, 95–110.

Rowe, P. (1987). A convenient empirical equation for estimation of the richardson-zaki exponent. *Chem. Eng. Sci.*, *42*, 2795–2796.

Ruan, Z., Wu, A., Bürger, R., Betancourt, F., Ordoñez, R., Wang, J., Wang, S., & Wang, Y. (2021). A population balance model for shear-induced polymer-bridging flocculation of total tailings. *Minerals*, *12*(1), 40.

Russel, W. B., Russel, W., Saville, D. A., & Schowalter, W. R. (1991). *Colloidal dispersions*. Cambridge university press.

Rzeznik, A. J., Flierl, G. R., & Peacock, T. (2019). Model investigations of discharge plumes generated by deep-sea nodule mining operations. *Ocean Engineering*, *172*, 684–696.

Schouten, T., van Rhee, C., & Keetels, G. (2021). Two-phase modelling for sediment water mixtures above the limit deposit velocity in horizontal pipelines. *J. Hydrol. Hydromech*, *69*(3), 263–274.

Schriever, G., & Thiel, H. (2013). *Tailings and their disposal in deep-sea mining* (Doctoral dissertation).

Sharma, R. (2015). Environmental issues of deep-sea mining. *Procedia Earth and Planetary Science*, *11*, 204–211.

Sharma, R., Nath, B. N., Parthiban, G., & Sankar, S. J. (2001). Sediment redistribution during simulated benthic disturbance and its implications on deep seabed mining. *Deep Sea Research Part II: Topical Studies in Oceanography*, *48*(16), 3363–3380.

Shen, X., Lee, B. J., Fettweis, M., & Toorman, E. A. (2018). A tri-modal flocculation model coupled with telemac for estuarine muds both in the laboratory and in the field. *Water research*, *145*, 473–486.

Shi, Z., Zhang, G., Zhang, Y., He, T., & Pei, G. (2019). Modeling of flocculation and sedimentation using population balance equation. *Journal of Chemistry*, *2019*.

Silva, L. F. L., Damian, R., & Lage, P. L. (2008). Implementation and analysis of numerical solution of the population balance equation in cfd packages. *Computers & Chemical Engineering*, *32*(12), 2933–2945.

Simpson, J., & Britter, R. (1980). Experiments on the dynamics of the front of a gravity current. *J. Fluid Mech*, *88*, 223–240.

Smith, S. J., & Friedrichs, C. T. (2011). Size and settling velocities of cohesive flocs and suspended sediment aggregates in a trailing suction hopper dredge plume. *Continental Shelf Research*, *31*(10), S50–S63.

Spearman, J., Taylor, J., Crossouard, N., Cooper, A., Turnbull, M., Manning, A., Lee, M., & Murton, B. (2020). Measurement and modelling of deep sea sediment plumes and implications for deep sea mining. *Scientific reports*, *10*(1), 1–14.

Strom, K., & Keyvani, A. (2011). An explicit full-range settling velocity equation for mud flocs. *Journal of Sedimentary Research*, *81*(12), 921–934.

Telford, J. (1966). The convective mechanism in clear air. *Journal of Atmospheric Sciences*, *23*(6), 652–666.

Terfous, A., Chiban, S., Ghenaim, A., Terfous, A., Chiban, S., & Ghenaim, A. (2019). Modeling sediment deposition from marine outfall jets To cite this version : HAL Id : hal-02126174.

Terfous, A., Chiban, S., & Ghenaim, A. (2016). Modeling sediment deposition from marine outfall jets. *Environmental technology*, *37*(15), 1865–1874.

Thiel, H. (2003). Anthropogenic impacts on the deep sea. *Ecosystems of the World*, 427–472.

Thiel, H., Schriever, G., Borowski, C., Bussau, C., Hansen, D., Melles, J., Post, J., Steinkamp, K., & Watson, K. (1989). Cruise-Report DISCOL 1, SONNE - Cruise 61. *3*, 91.

Thomas, D. G. (1965). Transport characteristics of suspension: Viii. a note on the viscosity of newtonian suspensions of uniform spherical particles. *Journal of colloid science*, *20*(3), 267–277.

Toorman, E., Bruens, A., Kranenburg, C., & Winterwerp, J. (2002). Interaction of suspended cohesive sediment and turbulence. In *Proceedings in marine science* (pp. 7–23). Elsevier.

Turner, J. (1962). The 'starting plume'in neutral surroundings. *Journal of Fluid Mechanics*, *13*(3), 356–368.

Turner, J. (1986). Turbulent entrainment: The development of the entrainment assumption, and its application to geophysical flows. *Journal of Fluid Mechanics*, *173*, 431–471.

United Nations. (2015). Paris agreement. *Report of the Conference of the Parties to the United Nations Framework Convention on Climate Change (21st Session, 2015: Paris). Retrived December*, *4*, 2017.

Van den Bremer, T., & Hunt, G. R. (2010). Universal solutions for boussinesq and non-boussinesq plumes. *Journal of fluid mechanics*, *644*, 165–192.

Van Leussen, W. (1994). Estuarine macroflocs and their role in fine-grained sediment transport. ministry of transport. *Public Works and Water Management, National Institute for Coastal and Marine Management (RIKZ)*.

Van Rhee, C. (2002). *On the sedimentation process in a trailing suction hopper dredger* (Doctoral dissertation). Delft University of Technology.

van Grunsven, F., Keetels, G., & van Rhee, C. (2018). The initial spreading of turbidity plumes–dedicated laboratory experiments for model validation. *48th Underwater Mining Conference (UMC)*.

van Reeuwijk, M., Salizzoni, P., Hunt, G. R., & Craske, J. (2016). Turbulent transport and entrainment in jets and plumes: A dns study. *Physical Review Fluids*, *1*(7), 074301.

Veerapaneni, S., & Wiesner, M. R. (1996). Hydrodynamics of fractal aggregates with radially varying permeability. *Journal of Colloid and Interface Science*, *177*(1), 45–57.

Verichev, S. N., Rhee, C. V., Jak, R. G., & Vries, P. D. (2014). Towards Zero Impact of Deep Sea Offshore Projects Towards Zero Impact of Deep Sea Offshore Projects An assessment framework for future environmental studies of deep-sea. (April).

Wickramasinghe, S., Han, B., Akeprathumchai, S., Jaganjac, A., & Qian, X. (2005). Modeling flocculation of biological cells. *Powder technology*, *156*(2-3), 146–153.

Winterwerp, J., Van Kesteren, W., Van Prooijen, B., & Jacobs, W. (2012). A conceptual framework for shear flow–induced erosion of soft cohesive sediment beds. *Journal of Geophysical Research: Oceans*, *117*(C10).

Winterwerp, J. C. (1998). A simple model for turbulence induced flocculation of cohesive sediment. *Journal of hydraulic research*, *36*(3), 309–326.

Winterwerp, J. C., & Van Kesteren, W. G. (2004). *Introduction to the physics of cohesive sediment dynamics in the marine environment*. Elsevier.

Wong, L. J., Kalyan, B., Chitre, M., & Vishnu, H. (2020). Acoustic assessment of polymetallic nodule abundance using sidescan sonar and altimeter. *IEEE Journal of Oceanic Engineering*, *46*(1), 132–142.

Yu, H.-Z. (1990). Transient plume influence in measurement of convective heat release rates of fast-growing fires using a large-scale fire products collector.

Zawadzki, D., Maciąg, Ł., Abramowski, T., & McCartney, K. (2020). Fractionation trends and variability of rare earth elements and selected critical metals in pelagic sediment from abyssal basin of ne pacific (clarion-clipperton fracture zone). *Minerals*, *10*(4), 320.

Zedler, E. A., & Street, R. L. (2001). Large-eddy simulation of sediment transport: Currents over ripples. *Journal of Hydraulic Engineering*, *127*(6), 444–452.

Zhang, J.-j., & Li, X.-y. (2003). Modeling particle-size distribution dynamics in a flocculation system. *AIChE Journal*, *49*(7), 1870–1882.

Zielke, W., Jankowski, J., Sündermann, J., & Segschneider, J. (1995). Numerical modeling of sediment transport caused by deep-sea mining. *First ISOPE Ocean Mining Symposium*.

Zuber, N., & Findlay, J. A. (1965). Average Volumetric Concentration in Two-Phase Flow Systems. *Journal of Heat Transfer*, *87*(4), 453–468. https://doi.org/10.1115/1.3689137

List of Publications

Journal Publications

Elerian M, Alhaddad S, Helmons R, van Rhee C. Near-field analysis of turbidity flows generated by polymetallic nodule mining tools. Mining. 2021 Dec;1(3):251-78.

Elerian M, Van Rhee C, Helmons R. Experimental and numerical modelling of deep-sea-Mining-Generated turbidity currents. Minerals. 2022 Apr 29;12(5):558.

Elerian M, Huang Z, van Rhee C, Helmons R. Flocculation effect on turbidity flows generated by deep-sea mining: A numerical study. Ocean Engineering. 2023 Jun 1;277:114250.

Conference Publications

Elerian M, Bedon Vasquez A, Enthoven D, Helmons R, van Rhee C The effect of particle size, salinity, flocculating agents on the propagation of mining-generated turbidity currents. Proceedings of the 23rd World Dredging Conference, WODCON XXlll, Copenhagen, Denmark, 2022.

Curriculum Vitae

Mohamed Elerian

14-02-1990	Born in Hail, Saudi Arabia

Education

2006-2011	Bachelor of Science (BSc.), Mechanical Engineering Tanta University, Egypt
2015-2018	Master of Science (MSc.), Water Resources Engineering and Management University of Stuttgart, Germany
2019-2023	Doctor of Philosophy(PhD) Delft University of Technology, The Netherlands Thesis: Numerical Investigation of Turbidity Flows Generated by Polymetallic Nodules Mining Promotor: Prof. dr. C. van Rhee Copromotor: Dr. ir. R.L.J. Helmons

Work Experience

2011-2015	Project Engineer, Focus Engineering Services, Cairo, Egypt
2017-2018	Intern, Daimler AG, Stuttgart, Germany
2018-2019	Project Engineer, Nohl Brandschutz GmbH, Stuttgart, Germany
2019-2023	PhD researcher, Delft University of Technology, Delft, The Netherlands
2023-Now	Environmental Engineer, Van Oord, Rotterdam, The Netherlands

Acknowledgements

With a heart full of gratitude, I thank the Lord Almighty, Allah, for giving me the chance, determination, and ability to do this research. His blessings and guidance have been essential on my journey. I'm also incredibly thankful to the amazing people who supported and showed kindness throughout this endeavor.

In my treasured memories of my academic journey, one person stands out - my esteemed professor, Cees van Rhee - who sadly passed away before I could express my deepest gratitude. I would like to take this opportunity to thank him enough for his continuous support throughout the past four years. His constant accessibility, motivation, and invaluable guidance were instrumental in shaping my academic journey. I will forever cherish the moments when he was there for me when I needed him the most. Though he is no longer with us, his impact on my life and academic pursuits will be a lasting testament to his dedication as a mentor and educator. Thank you, Cees, for everything you have done for me.

To Rudy Helmons, my mentor and my daily supervisor, words cannot adequately express my gratitude towards you. Right from the moment you offered me this opportunity and accepted me for this challenging endeavor, I knew that you had faith in my abilities. I always recognized that your ultimate goal was to bring out the best in me. Your solid commitment to keeping me motivated and your continuous support have played a vital role in shaping my journey. I am truly indebted to you for your exceptional supervision and the immense guidance you have provided throughout. Your belief in my potential has pushed me to exceed my own expectations. I want to sincerely thank you for your dedication, encouragement, and mentorship. It has been an honor to work under your guidance, and I am immensely grateful for the invaluable contributions you have made to my personal and professional growth.

I express my sincere gratitude to Prof. Gabe Weymouth for accepting to be the promoter for my PhD defense on short notice. Thank you, Gabe, I am truly honored.

I would also like to express my deep gratitude to Said Alhaddad for his invaluable instructions during the writing of my first paper. Working with Said has been an enlightening journey of learning and growth. His expertise

has played a crucial role in shaping my understanding of the research process. Thank you, Said, for being an exceptional colleague and friend, and for generously sharing your knowledge and expertise with me. Your contributions have had a profound impact on my academic journey, and I am sincerely thankful for the support you have provided me.

A heartfelt shout-out goes to my incredible roommates, Stefano and Thijs. Our countless conversations about every thing in life, in particular, Computational Fluid Dynamics (CFD) and the different models involved have been an absolute game-changer for my understanding and improvement in simulations. Stefano, I can't thank you enough for our lively discussions on how we see the world. Your view and perspectives have broadened my horizons in more ways than I can express. The time we spent diving deep into those topics will always be cherished. Thijs, I owe you a big thank you for laying down the foundational knowledge of OpenFOAM. Your instructions have been invaluable in helping me navigate through this intricate world. The expertise you shared has been a crucial building block in my learning and growth. To both of you, I am immensely grateful for the contribution you've made to my journey.

The IHC guys, Bas Nieuwboer and Edwin de Hoog, deserve a special mention for their exceptional support throughout my research journey. Bas, your insightful discussions and expertise in OpenFOAM have been absolutely invaluable. Your contributions have not only expanded my understanding but have also propelled the progress of my work. I am truly fortunate to have had the opportunity to learn from you and benefit from your expertise. And Edwin, I want to express my sincere appreciation for your valuable input in this research area. Our countless discussions about the drift-flux model and its various aspects have provided me with the necessary insights to pursue my research. Your support has been instrumental in shaping the direction of my work. I am truly grateful for your unwavering support and exceptional contributions to my research endeavors.

I want to give a big shout-out to my awesome TUDelft colleagues Antonio, Arno, Geert, Dhruv, Jian, Xiuhan, Shaheen, Waqas, and Mosaab. You guys have made my time here unforgettable with all the amazing memories we've created together. And let's not forget about our endless coffee corner discussions! Thank you all for the good times and great conversations. Cheers to our wonderful camaraderie!

To my incredible Arabic gang all over the world, Hamed, Khopayp, Mostafa Emam, Hazem, Abdelqader, Hany, Omar Eladel, Mohamed Mostafa, Tareq Elzaqoot and Ezz Eldein – I want to give a huge shoutout and express my deepest gratitude! You guys have been my rock, always there to support me and lift me up. Your friendship and encouragement have been invaluable to me, and I cherish the memories we've created together. Hamed, our moments of sipping cappuccino while sharing your wisdom on navigating research work will forever be treasured. Your insights have been instrumental in shaping my journey. Thank you all for being the incredible friends that you are, always there to brighten my days and inspire me to reach new heights.

To my incredible parents, I want to express my deepest gratitude for the unwavering support you have provided me throughout my life. Dad, you have been my role model as an engineer and have taught me the importance of hard work and perseverance in achieving my goals. Your guidance and wisdom have shaped me into the person I am today. Mom, your unwavering dedication to raising me and molding me into the person I have become is truly remarkable. Your love and sacrifices have been invaluable. Thank you both for being the amazing parents that you are. I am forever grateful for your love, support, and teachings.

To my amazing siblings, Ahmed, Wafaa, Mahmoud, and Moataz, I want to express my heartfelt thanks for your unwavering support throughout my journey here in the Netherlands. Your encouragement and belief in me have been invaluable. Whether it was through your words of wisdom or simply being there to listen, you have shown me unconditional support. I am truly grateful for the bond we share and the strength you bring to my life. Thank you for always being there for me and for being an essential part of my journey.

To Malek, my son, you are my greatest joy and the source of endless happiness in my life. From the moment you entered this world, my heart has been filled with an indescribable love for you. For the past three years, coming home to your smiling face after a long day at work has been the highlight of my day. Your laughter, your innocence, and your unconditional love have been a constant source of motivation and inspiration for me. You remind me of what truly matters in life and encourage me to be the best version of myself.

And finally, the most important person in my life, my beloved wife Ayat. You have been the rock that has kept me grounded throughout this entire journey. Your unwavering love, support, and understanding have been my

greatest source of strength. You have stood by my side through the ups and downs, believing in me even when I doubted myself. Your patience, encouragement, and sacrifices have allowed me to pursue my dreams with confidence.